

POLITECNICO DI TORINO

Master Degree in Biomedical Engineering
Master Thesis

Molecular and coarse grained modelling to characterize and optimize dendrimer-based nanocarriers for siRNA delivery



Thesis Advisor:
Prof. M. A. Deriu

Candidate:
Filip Stojceski

ACADEMIC YEAR 2018-2019

*“Science is not only a disciple of reason but,
also, one of romance and passion.”*

-Stephen Hawking-

Table of Contents

1. Introduction	8
2. Scientific background	10
2.1. Introduction to Rheumatoid arthritis	10
2.2. Symptoms and risk factors	11
2.3. Pathophysiology	12
2.4. Diagnosis	14
2.5. Medical treatment.....	14
2.5.1. Dendrimer-siRNA based medical treatment.....	17
3. Materials and methods	19
3.1. Introduction to molecular dynamics	19
3.2. Molecular mechanics.....	20
3.2.1. The potential energy function.....	20
3.2.2. Bonded interactions	20
3.2.3. Non-bonded interaction	22
3.2.4. Periodic boundary condition.....	23
3.2.5. Cut-off radius restrictions	24
3.3. Molecular dynamics	25
3.3.1. Statistical ensemble	25
3.3.2. Ergodic hypothesis	27
3.3.3. Energy minimization	28
3.3.4. Leapfrog integrator	29
3.3.5. Constraint algorithm	30
3.3.6. Temperature coupling.....	31
3.3.7. Pressure coupling.....	32
3.4. Simulated annealing	33
3.5. Coarse Grained modelling.....	34
3.5.1. Martini force-field	35
3.5.2. Modified Boltzmann inversion	40

4. Coarse Grained dendrimers models	42
4.1. Introduction	42
4.2. Materials and methods.....	43
4.2.1. Atomistic Simulation.....	43
4.2.2. CG System set up	45
4.2.3. Molecular dynamics	51
4.3. Results and discussion	52
4.4. Dendrimers self-assembly proprieties	58
4.4.1. Introduction	58
4.4.2. Materials and methods.....	58
4.4.3. Results and discussion.....	59
4.5. Conclusions	63
5. Elucidating interaction mechanism between dendrimers and siRNA	64
5.1. Stoichiometry of dendrimer-siRNAs binding capability.....	64
5.1.1. Introduction	64
5.2.2. Materials and methods.....	64
5.2.3. Results and discussion.....	66
5.2. Conclusions	74
6. Conclusions and future development	76
Acknowledgment	77
Bibliography	78
Supporting Information	89

Estratto

L'artrite reumatoide (RA) è una malattia infiammatoria cronica autoimmune, che colpisce principalmente le articolazioni portandole alla progressiva distruzione. L'AR colpisce lo 0,5-1% delle persone nel mondo sviluppato secondo le statistiche elaborate nel 2015. L'insorgenza dei sintomi spesso richiede diverse settimane, portando alla comparsa di calore, arrossamento, gonfiore e dolore nella giuntura affetta. Oggigiorno, la terapia per trattare l'AR consiste principalmente nell'alleviare i sintomi e nel rallentare l'evoluzione della malattia usando farmaci antidolorifici, antinfiammatori e modificanti la malattia reumatici (DMARD). Tuttavia, non esiste ancora una terapia che blocchi completamente la progressione della malattia. Un nuovo trattamento attualmente in fase di test in vivo, raggiunge l'obiettivo di arrestare lo sviluppo di RA, bloccando la distruzione delle articolazioni. Si tratta della terapia di silenziamento genico mediata da micro RNA interferente (siRNA), che ostacola la produzione normale di citochine nei leucociti. Il concetto alla base è quello di ostacolare la produzione di citochine infiammatorie, in modo da sopprimere la risposta autoimmune. Una volta che l'infiammazione viene arrestata, anche il riassorbimento della cartilagine viene interrotto. Uno dei problemi principali è portare gli siRNA all'interno delle cellule mantenendo intatta la loro struttura, evitandone il degrado nell'ambiente extra-cellulare. Pertanto, è necessario sviluppare un sistema di trasporto dei farmaci che sia biocompatibile, affidabile ed efficiente. I dendrimeri sono nano-carrier polimerici ramificati, che hanno dimostrato la capacità di trasportare numerosi tipi di carichi farmacologici all'interno delle cellule, anche gli stessi siRNA. In numerosi esperimenti in vitro e in vivo, è stato dimostrato che i dendrimeri possono legare gli siRNA e rilasciarli nelle aree bersaglio. Lo scopo di questo lavoro di tesi è esplorare le caratteristiche sopramolecolari della complessazione tra dendrimeri e siRNA. Attraverso l'uso di un particolare tipo di dinamica molecolare (MD), chiamata "Coarse Grained" (CG) MD abbiamo chiarito alcuni aspetti riguardanti l'aggregazione tra dendrimeri e siRNA, non del tutto compresi fino ad ora. Sono stati considerati due tipi di dendrimeri ingegnerizzati: i dendrimeri Pyrrolidinium (DP) e i dendrimeri Morpholinium (DM). In primo luogo, è stato studiato il comportamento di auto-assemblaggio dei dendrimeri DM e DP, dove è stato riscontrato che il DP ha una maggiore capacità di auto-aggregarsi, formando oltretutto del precipitato in soluzione. Successivamente, sono stati valutati i valori di stechiometria DM e DP nel legare il siRNA per far luce del perché i DP hanno una maggiore efficienza nel legare 2 siRNA, mentre i DM riescono a legare tendenzialmente solo 1 siRNA. Infine, è stato valutato il comportamento di competizione dei dendrimeri-siRNA, verificando se i valori stechiometrici sono in qualche modo influenzati da questo meccanismo. L'analisi delle proprietà di aggregazione

sopramolecolare utilizzando la MD, rende possibile stabilire le linee guida per lo sviluppo o la modifica della struttura chimica dei dendrimeri reali, con l'obiettivo di realizzare dendrimeri nanomerici ancora più efficienti ed affidabili. Inoltre, le simulazioni MD possono tentare di determinare i fenomeni di aggregazione molecolare tra dendrimeri e siRNA che potrebbero altrimenti rimanere inspiegati.

Abstract

Rheumatoid arthritis (RA) is a chronic autoimmune inflammation disorder, which mainly affects the articulations leading them to progressive destruction. RA bear upon 0.5-1% of people in the developed world according to statistics drafted in 2015. The onset of symptoms often takes several weeks, leading to the appearance of warmness, redness, swelling and pain in affected juncture. Nowadays, the therapy to treat RA consists mainly in relieving the symptoms and slowing the evolution of the disease using analgesic, anti-inflammatory and disease-modifying anti-rheumatic drugs (DMARDs) drugs. Nevertheless, there is still no therapy that completely blocks the progression of the disease. A new treatment currently in phase of *in vivo* testing, achieve the goal of halting the development of RA, blocking the destruction of articulations. This is the case of gene silencing therapy mediated by short interfering RNA (siRNA), which hinder the normal production of cytokines in leukocytes. The concept is to obstacle the production of cytokines that cause the inflammatory state which will suppress the auto-immune response. Once the inflammation is arrested, the cartilage reabsorption is also interrupted. One of the mainly issues is to carry siRNAs inside the cells keeping their structure intact, avoiding the extra-cellular environment degradation. Therefore, it is necessary to develop a biocompatible, reliable and efficient drug delivery system. Dendrimers are polymeric hyperbranched nano-carriers that have demonstrate a greater capability to transport numerous different type of cargos inside cells, even siRNAs. In several *in vitro* and *in vivo* experiments, it has been shown that dendrimers can bind siRNAs and release them in the target areas. The purpose of this master thesis work is to explore the supramolecular characteristic of dendrimers-siRNA complexation. Through the use of coarse grained (CG) molecular dynamics (MD) we elucidate some aggregation mechanisms between multiple dendrimers and siRNAs, still unclear. Two types of engineered dendrimers were considered: Pyrrolidinium dendrimers (DP) and Morpholinium dendrimers (DM). Firstly, was investigated the self-assembly behavior of DM and DP dendrimers, highlighting that DP has a greater capability to interact with each other, forming precipitate in solution. Afterwards, DM and DP stoichiometry values in binding siRNA were evaluated to shed light on the more efficient ability of DP to bind 2 siRNAs, while DM can mostly bind 1 siRNA. Lastly, dendrimers-siRNAs binding competition behavior was assessed, verifying if the stoichiometric values are influenced by this mechanism. Analyzing supramolecular aggregation proprieties by MD, makes possible establish the guidelines for developing or modifying the actual dendrimers chemical structure, with aim to realize even more efficient and reliable dendrimers nano-carriers. Moreover, MD simulations can try to determinate molecular phenomena in aggregation of dendrimers-siRNA that may be otherwise unexplained.

1. Introduction

Rheumatoid arthritis (RA) is a chronic autoimmune inflammation disease, which causes the progressive destruction of the articulations^{1,2}. RA affects around 0.5-1% of people in the developed world and according to statistics in 2015, ascertained cases amounted to 24.5 million of people³. RA disorder is a pathology that more commonly begins in middle-aged individuals, with a higher incidence in women than men². According to the most recent statistics, RA has caused 38000 deaths in 2013, increasing by about a third the mortality rate of 1990, attested to 28,000 deaths⁴. Nowadays, the therapy to treat RA consists mainly in relieving the symptoms and slowing the evolution of the disease. Analgesic and anti-inflammatory therapy consist in the administration of:

- Steroid drugs, such as glucocorticoids^{2,5}.
- Non steroid drugs, such as Etoricoxib, Diclofenac^{2,6}.
- Natural compounds, such as capsaicin⁷⁻⁹.

An innovative approach to slowing the progression of the disease¹⁰ is to use disease-modifying anti-rheumatic drugs (DMARDs)^{11,12}, also called biological response modifiers. DMARDs are genetically engineered treat-to-target drugs, designated to reduce joint inflammation by stopping the cascade of events responsible for the inflammatory process. Pro-inflammatory cytokines are the primary targets on which these drugs operate. Certolizumab^{13,14} and Etanercept¹⁵ are examples of cytokine tumor necrosis factor alpha (TNF- α) inhibitor^{16,17}. Recently, a promising therapeutic strategy to interfere in the cytokine signaling pathway is the use of small interfering RNA (siRNA)¹⁸⁻²⁰ that can silence the genes responsible for the pro-inflammatory protein production. siRNA is a class of double-stranded RNA filaments which can undergo a rapid degradation in a chemically aggressive environment such as the human body. For this reason, the development of an efficient drug delivery system plays a key role for the success of siRNA-based medical treatments. Cationic phosphorous dendrimers^{21,22} have proven to be excellent drug delivery carriers for gene therapy after *in vivo* experiments²³⁻²⁶. The stability of dendrimer-siRNA complexation in the delivery phase and the release of siRNAs once the target cell is reached, plays a key role to evaluate the therapeutic potential of the dendrimer delivery system. Deriu *et al.* investigate how the role of dendrimer surface chemistry influence the dendrimer-siRNA binding energies and also elucidates molecular reasons related to complexation stoichiometry²⁷. In this research two dendrimers of third generation which differ only for one atom in the chain terminal were studied. The two different type of functionalization applied at dendrimer's terminal groups are:

- Pyrrolidinium (DP) terminal groups²⁸, which is a cation formed by protonation of a pyrrolidine.
- Morpholinium (DM) terminal groups²⁸, which is the conjugate acid of morpholine.

Results of the study shed light on the molecular mechanism behind higher efficiency of DP in binding siRNA²⁷, while DM demonstrate less efficiency. Nevertheless, the above mentioned study left opened three issues related to dendrimer supramolecular phenomena, listed in the following.

- Dendrimers self-assembly tendencies²⁷.
- Stoichiometry in binding siRNA²⁰.
- Competition in binding siRNA.

This master thesis research is divided according the following pattern: The first (current) section is the Introductory part ([chapter 1.](#)). The second chapter ([chapter 2.](#)) deals with the scientific background about RA disease. The third chapter ([chapter 3.](#)) offers information on materials and methods used to investigate the dendrimer-siRNA supramolecular characteristics. The fourth section ([chapter 4.](#)) provides insights concerning the development and validation of coarse grained (CG) models. Finally, in the last chapter ([chapter 5.](#)) is focus on the investigation about the supramolecular characteristics in dendrimer-siRNA binding stoichiometry.

2. Scientific background

2.1. Introduction to Rheumatoid arthritis

RA (Figure 1) is a chronic autoimmune inflammatory disease that causes pain, swelling, stiffness and loss of function of articulations^{1,2}. It manifests when the immune system, usually responsible for the defense of the organism from external pathological agents, attacks for reasons still partially unknown, the membranes that cover the articular surfaces. The autoimmune response of leukocytes generates inflammation, which slowly extends throughout the joint, get under way the gradual juncture degradation process. In severe cases of the RA disease, joints damage can be very serious and disabling, besides, there may be associated side effects such as: osteoporosis, depression, infection, cancer, cardiovascular disease and interstitial lung disease²⁹. Nowadays there is still no definitive cure for RA and the symptoms of patients affected by this disease are treated with anti-inflammatory and pain-relieving drugs^{2,5-8}. More specific treat-to-target engineered therapy¹⁰⁻¹² is adopted to retard the progression of disease and an innovative gene silencing treatment^{18,20,27} is being tested with the aim of definitive freezing the RA progression.

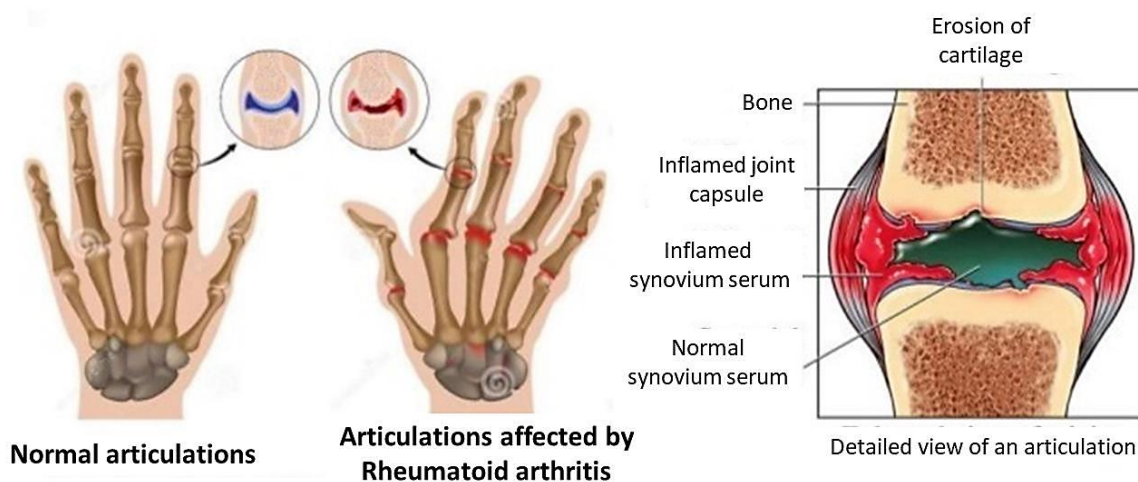


Figure 1: Generic and detailed illustration of the effect on juncture caused by rheumatoid arthritis (RA) disease. We can see how the articulations affected by RA has an area of inflamed synovial fluid, leading to a bone deformation. Furthermore, local inflammatory state causes the reabsorption of neighboring cartilaginous portions, which result in previously mentioned bone deformation.

2.2. Symptoms and risk factors

RA symptoms typically develop within several weeks, but in acute cases can also occur in a few days. The first biological structures that are affected by RA are the articulations, but in some cases the inflammatory phenomenon can also extend to other organs³⁰. Joint inflammation induces limitation in limb motion due to onset of pain, stiffness, warmth, swelling, as mentioned before. Usually the RA symptoms occur in the morning or in resting time and may last for hours. This disease can become disabling, because it starts targeting and deforming the extremities, where the bones are thinner, up to more complex articulations, like knees^{31,32} or shoulders³³. Wrist bone misshapeness may result in non-physiological compression of the median nerve rising up risks of carpal tunnel syndrome^{34,35}. As in the case of carpal tunnel syndrome cited earlier, bone deformation and reabsorption sometimes can lead to osteoporosis^{36,37} or teeth degeneration process, like periodontitis³⁸. Common complication related to RA could be heart and vessels disease: risk of myocardial infarction, endocarditis, pericarditis, atherosclerosis, fibrosis, stroke are strongly increased³⁹⁻⁴¹ and complications can even reach the lungs, because of their proximity. Furthermore, 30% of patients who have RA also manifest a non-joint disorder of the skin which name is rheumatoid nodule⁴², usually situated at bony prominences. As we described in this chapter, RA may occur a variety of more or less serious symptoms, which affect a person's quality of life. The etiology of this pathology is still unclear, but some environmental and genetic⁴³ factors (Figure 2) seem to have an impact on raising the risk of RA. Mutation of genes encoding major histocompatibility complex (MHC) and human leukocyte antigen (HLA) proteins^{44,45}, is a well-known cause associated with the development of RA. In more detail, alteration of HLA system, especially HLA-DRB1 gene, is strongly involved in RA pathogenesis. MHC and HLA complex are responsible for the recognition of endogenous proteins from external antigens by the immune system. Polymorphism of MHC and HLA proteins can lead into an erroneous identification of own cells by leukocytes, which will start the inflammatory response. According to the newest genome-wide association studies, approximately in 50% of RA cases were located genetic trigger mutations, while in 20% of RA episodes weren't found genetic trigger mutations². In addition, further non-genetic factor appears to play a role in RA disease etiology. Smoking, for example, has been proven that increase the disease incidence by 3 times⁴⁶, amplifying also the severity symptoms. Moreover, supplementary environmental factors have been established as potentially involved in the development of the disease, including: *Silica exposure, infection*⁴⁷, *air pollution, high red meat and sodium assumption, obesity and low vitamin D intake*⁴³. Despite major risk factors have been identified, it is still difficult to clearly identify the set of triggering causes, since RA is a chronic autoimmune pathology with many different pathobiological pathways. The best way to prevent the uprising of RA disorder is the reduction of risk factors.

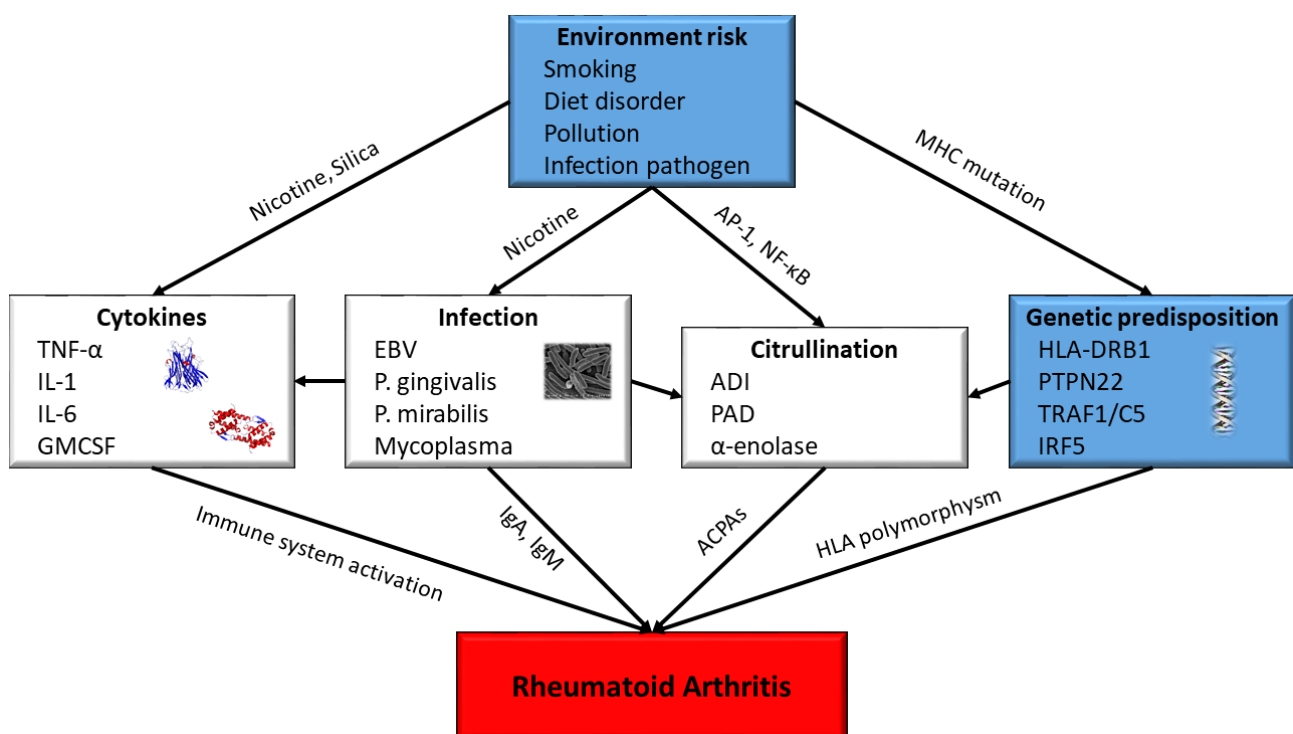


Figure 2: Generic scheme of how genetic and environment risk factor may lead to a cascade of events that cause the development of rheumatoid arthritis (RA).

2.3. Pathophysiology

Nowadays, our comprehension of RA intrinsic biological pathways has definitely improved compared to a decade ago (Figure 3). The discovery of the inflammatory and immunological pathways allowed to identify the chemical factors that underlie the autoimmune destructive process⁴⁸. Moreover, it has been uncovered that once disease initiate, even if we eliminate the trigger element, the progression of pathology is supported by an auto-perpetuating scheme⁴⁸. The process of RA begins when the leucocytes reach the synovial cells membrane starting for reasons not completely known yet, an inflammation process (Figure 3). Probably, the missed recognition of synovial cells by white blood cells, is due to the hyper-citrullination^{49,50} of the arginine residues contented in MHC peptides and to HLA-DRB1⁴⁴ gene polymorphism. Citrullination is a normal process that occur in post-translational modification, which transform amino acid arginine into non-standard amino acid citrulline. When a T-lymphocyte binds one of those MHC degraded peptides, different scenarios can happen: apoptosis, tolerance or activation⁵¹. The event that triggers the RA is certainly the activation of T-cells, which begin production of pro-inflammatory cytokines⁵² including *IL-1*, *IL-6*, *IL-8*,

GM-CSF and *TNF- α* ^{53,54}. Afterwards, the increased concentration of cytokines in the surrounding micro-environment induce the *in situ* migration of other type of leukocytes, such as: *macrophages*, *B-lymphocytes*, *neutrophils*, in addition to the aforementioned *T-lymphocytes*. B-lymphocytes⁵⁵ are activated through direct contact with T-cells or via cytokines signaling and are able to produce anti-citrullinated peptide antibodies (ACPA), which modulate the specific immune response. Instead, macrophages⁵⁶ seem to be the main cause of articular structures erosion. The great joint damage happens because the macrophages are able to produce high quantities of cytokines, which themselves recall other macrophages and other degradation cells. This is the case of chondrocytes and osteoclast, which respectively, produce proteases responsible for structural protein degradation (collagen) and produce enzymes which lead to bone resorption. The cartilage destruction and the over-expressed activity of macrophages and fibroblast manage the formation of Pannus, which is a granulated tissue that is responsible for the most part of pain generation⁵⁷.

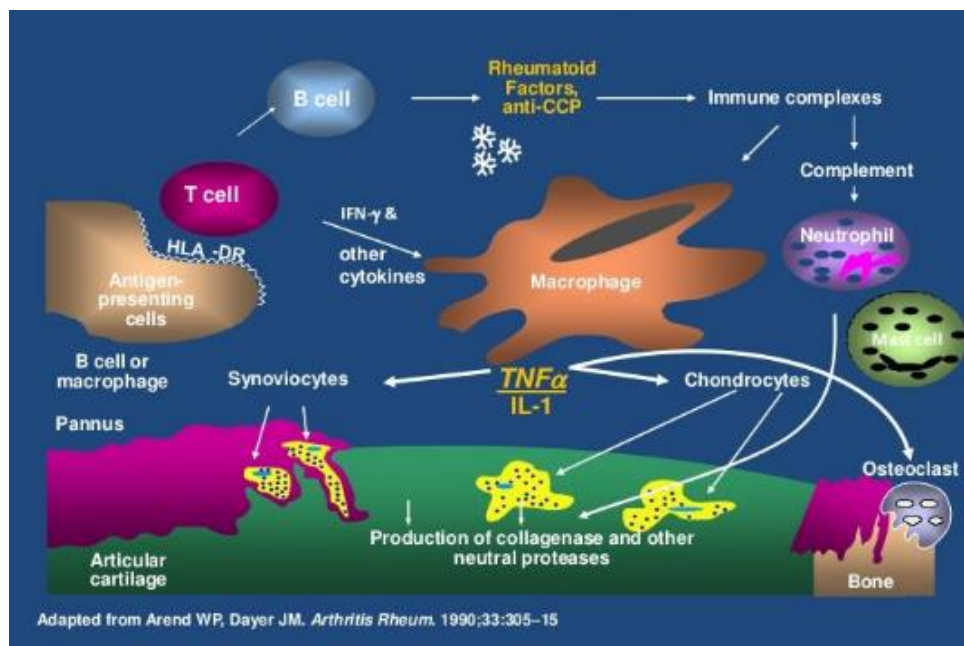


Figure 3: Scheme of the pathogenesis of Rheumatoid arthritis. T-lymphocytes trigger the inflammation recognizing endogenous cell as antigen, starting the production of cytokines. Increased concentration of cytokines induce the above showed sequence of immune response, also activating osteoclast mediated bone reabsorption and chondrocytes production of collagenase and other proteases. All described degeneration process lead into creation of thin layer over cartilage surface called Pannus, which is a granulation tissue derived from hyper production of fibroblast, proteolytic enzymes and inflamed synoviocytes.

2.4. Diagnosis

Early detection of RA may be complicated, due to the gradual appearance of symptoms, as well as a strong variety of symptoms from individual to individual³¹. Initially, the patient's medical history is collected, looking for genetic and environmental risk factors and RA-specific symptoms. Subsequently, if RA is clinically suspected, a blood test is performed searching for immunoglobulins called rheumatoid factor (RF) and ACPA⁵⁸, which are present in the most of people affected by this disease. Further laboratory exams are often prescribed to differentiate the RA from other types of arthritis, such as: *C-reactive protein*, *erythrocyte sedimentation rate (ESR)*, *kidney enzymes*, *liver function* and *ferritin*. Finally, to evaluate the degree of articulation impairment, imaging analysis is performed, which includes x-rays, Magnet resonance (MRI) and ultrasound (US)⁵⁹. X-rays are usually used as an early exam when multiple articulations are involved with the aim to ascertain the RA disorder, as a consequence of their soft tissue poor resolution and harmfulness. Otherwise, Magnet resonance is actually considered the best non-invasive imaging method to estimate the inflammation of joints, tendons and bones. As stated by EULAR (European League Against Rheumatism) board, MRI is suggested for:

- Evaluate the inflammatory lesions (with or without contrast).
- Check out treatment response and monitoring disease progression.
- Assessing early stage of synovitis, tenosynovitis and bursitis.
- Early establishment of RA complications.

As a result of the continuous improvement of US technology, such as Color Doppler imaging, it can be used to assess the degree of synovial inflammation marking vascular signals from junctures⁶⁰. This is a remarkable feature because in the early phase of RA, synovial fluid appears to be primarily affected and synovitis gives the impression of being the best predictive cue for the early diagnosis of RA.

2.5. Medical treatment

Early detection of RA is as important as the therapeutic treatment plan and successive follow-up period. The first strategy for those who have cases of RA in family is to prevent the onset of the disease by reducing the risk factors. If pathology is ascertained, fortunately many medical management options are available⁶¹. The basic concept of RA treatment aims toward achieving the lowest

possible level of inflammation activity, minimizing or stopping articulation deterioration, and enhancing physical function with the purpose of improving the life quality. Medical care options generally include drugs assumption, physical and social therapy, up to surgical intervention in the severe cases⁶¹. Pharmacological strategies are designed for controlling and possibly suppress the major symptoms, which are inflammation and pain. There are three main analgesic and anti-inflammatory used drugs:

- Corticosteroids^{2,5}: are useful in early stages because of their anti-inflammatory and immunoregulatory behavior. They can be administered intramuscularly, orally, intravenously or directly injected into the joint. The most used corticosteroids are *prednisone*, *hydrocortisone*, *dexamethasone* and *methylprednisolone*.
- Non-steroidal anti-inflammatory drugs (NSAID)^{2,5,6}: are anti-inflammatory non-steroidal drugs class which have also a slight analgesic effect. A large number of NSAIDs used for RA are actually in commerce, including *diclofenac*, *ibuprofen*, *naproxen*, *ketoprofen* and many others.
- Natural compound⁷⁻⁹: synthetic steroidal and non-steroidal drugs suffer a lot of side effects, which sometimes may lead to serious complications. Find out natural remedy is a promising strategy that seems to allow a satisfactory control of symptoms, without remarkable side effects. For example, capsaicin has shown an encouraging propriety if used as topic ointment.

A novel approach designated to reduce joint inflammation¹⁰ is the use of disease-modifying anti-rheumatic drugs (DMARDs) also called biological response modifiers. DMARDs^{11,12} are genetically engineered treat-to-target drugs, which can block the activity of specific objective. Nowadays, only these medical agents showed an efficacious slowdown of normal RA pathologic flow. Therefore, once diagnosis is confirmed, DMARDs therapy should be started as soon as possible. Table 1 sheds lights on the commonly prescribed DMARDs compound. Analyzing Table 1 we can carry out that TNF- α is frequently a target cytokine, which suggests its centrality in the various RA pathways^{16,17}. However, even if effective countermeasures to TNF- α activity have been successfully developed over the last decade, such as Certolizumab¹⁴ and Etanercept¹⁵, their application is hindered by the risk of injection site reactions, infusion reactions, or infections⁶². Recently, a new promising therapeutic approach to interfere in the TNF- α signaling pathway is the employment of small interfering RNA (siRNA)¹⁸ that can silence transcription of the genes responsible for this pro-inflammatory protein production¹⁸. siRNAs based medical treatments has many different advantages, including specificity, affordability, minimal side effects and effortless production. On the other hand, the application of

Table 1: Table adapted from <https://en.wikipedia.org/>. In this table are shown DMARDs names with their action mechanisms and drugs type. **csDMARDs** are synthetic traditional drugs; **tsDMARDs** are synthetic treat-to-target drugs; **bDMARD** are biological drugs.

Drug	Mechanism	Type
Abatacept	T-cell costimulatory signal inhibitor	bDMARD
Adalimumab	TNF- α inhibitor	bDMARD
Anakinra	IL-1 receptor antagonist	bDMARD
Azathioprine	Purine synthesis inhibitor	unknown
Certolizumab pegol	TNF- α inhibitor	bDMARD
Chloroquine (anti-malarial)	Suppression of IL-1, induce apoptosis of inflammatory cells and decrease chemotaxis	unknown
Ciclosporin A	calcineurin inhibitor	unknown
D-penicillamine	Reducing numbers of T-lymphocytes etc.	unknown
Etanercept	decoy TNF- α receptor	bDMARD
Golimumab	TNF- α inhibitor	bDMARD
Gold salts	unknown	csDMARD
Hydroxychloroquine (anti-malarial)	TNF- α , induce apoptosis of inflammatory cells and decrease chemotaxis	csDMARD
Infliximab	TNF- α inhibitor	bDMARD
Leflunomide	Pyrimidine synthesis inhibitor	csDMARD
Methotrexate (MTX)	Purine metabolism inhibitor	csDMARD
Minocycline	5-LO inhibitor	unknown
Rituximab	chimeric monoclonal antibody against CD20 on B-cell surface	bDMARD
Sulfasalazine (SSZ)	Suppression of IL-1 & TNF- α , induce apoptosis of inflammatory cells and increase chemotactic factors	csDMARD
Ttocilizumab	IL-6 receptor antagonist	bDMARD
Tofacitinib	kinase inhibitor	tsDMARD

siRNA macromolecules for therapeutic purposes are limited by 1) their structure instability in biological fluids, 2) their low cellular penetration, and 3) their susceptibility to enzymatic degradation guided by nucleases. To get around these issues, the future success of siRNAs genic silencing treatments is strongly related to the design of reliable and efficient drug delivery technologies^{19,23} that ensure the release in the endosomal pathway, the cellular uptake, the structure stability during delivery and subcellular distribution⁶³. Synthetic cationic polymers give the impression of being an attractive perspective as carriers, with the envisioned advantages of high stability, ease of production, low cost, well-defined size, and versatility for different applications⁶⁴. Recently, particular attention has been attributed to dendrimers, which are hyper-branched polymers characterized by near-spherical shape with high monodispersity and vast opportunities for surface tailoring which increase nucleic acids binding capability into the nanoparticle^{23-26,65,66}.

2.5.1. Dendrimer-siRNA based medical treatment

Nowadays, latest medicine doctrine is based on the development of a well-engineered gene therapy, which involves the introduction of small fragments of nucleic acids inside the cell to silence specified gene. siRNAs are a new promising class of drugs for many pathological disorders, as chronic immunological disease²⁵, cancers⁶⁷ and degenerative pathology, like RA^{18,19}. These small molecules are employed in an interference process where expression of a homologous nucleic gene is silenced or even inhibited⁶⁸ (Figure 4). Major obstacle for the use of siRNAs for therapeutic purposes, lies in the high instability in an aggressive environment like the human extra-cellular matrix. Therefore, development of reliable, efficient and non-toxic drug delivery system⁶⁹ plays a key role in making the way for safe release of siRNAs inside desired cells. Dendrimers are a novel category of hyperbranched polymers with an organized molecular structure⁷⁰ that put together well-defined monodispersity and composition with high molecular mass. Moreover, dendrimers seem to have an innovative outcome for new-based medical treatment^{21,23,71} in a plenty diseases. Cationic phosphorous dendrimers have been proved to be excellent candidates for gene and drug delivery carriers through *in vivo* experiments^{23,25,27,28}. In particular a recent study, highlighted the behavior of cationic phosphorous dendrimers to complex with siRNA^{23,24,27}. Consequently, since dendrimer has proved to be a good drug delivery vector and siRNA has established promising features for RA treatment, additional investigations for increasing knowledge about dendrimer-siRNA complexation is needed.

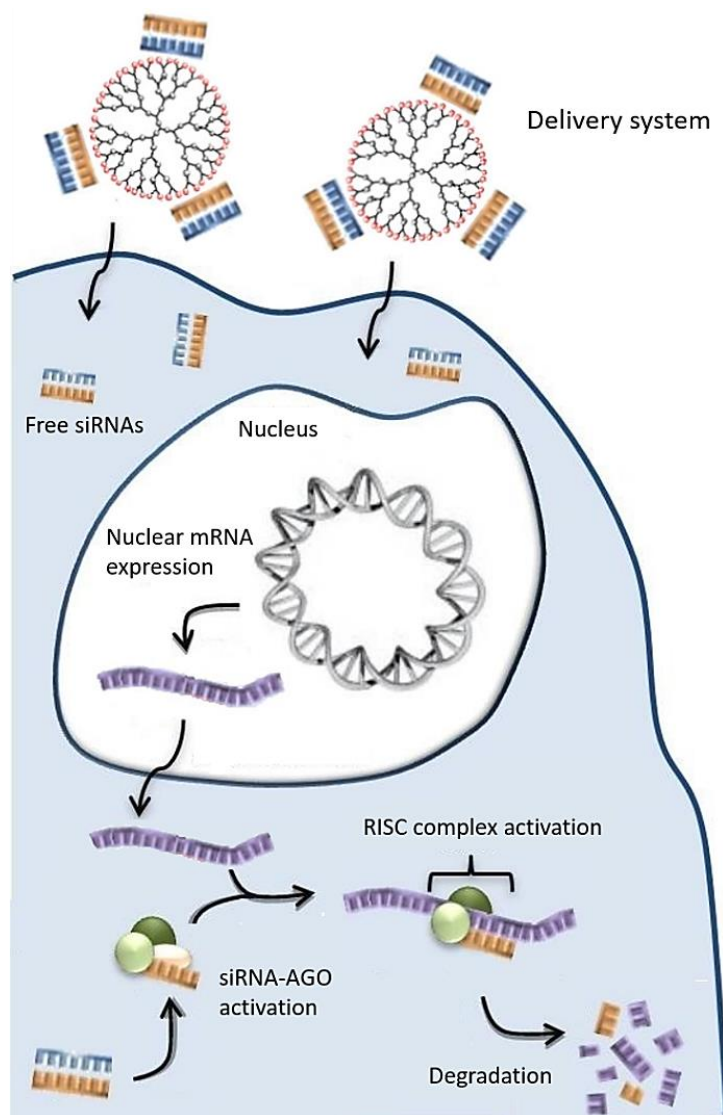


Figure 4: Illustration of overall drug delivery and action mechanism through which siRNA molecules can silence or inhibit genes. Initially dendrimer carriers loaded with siRNAs is phagocytized by target cell, where cargos releasing starts. Afterward, siRNA double stranded filament is recognized and complexed by protein argonaute (AGO), which split siRNA in two separated filament, using one of them as template for mRNA recognizing. Once mRNA bind the activated siRNA-AGO compound, other enzymes belonging to group called RISC (RNA-induced silencing complex) triggers cleaving of mRNA which leads in fast mRNA-siRNA degradation, blocking *de facto* protein transcription. Therefore, if transcription of encoding sequences for target protein is blocked, then it means that the gene responsible for the production of that particular protein has been silenced, explaining why it is called “gene therapy”.

In this master thesis work, the interaction properties between cationic phosphorous dendrimers and siRNAs, will be further researched using Molecular Dynamics tools with the aim to increase comprehension of complexation phenomena. Moreover, deepening inside the aggregation properties of dendrimer-siRNA systems, creation of a platform able to predict the characteristics of upcoming dendrimeric vectors may be possible.

3. Materials and methods

3.1. Introduction to molecular dynamics

In general, the term molecular dynamics⁷² (MD) identifies all computational simulation techniques which, performing the integration of the Newton motion equations, allows to study the dynamics of evolution of a physical and chemical system at the atomistic and molecular level. The way of describing the trajectories and the interactions of particles strongly characterizes the type of molecular dynamics, which can be divided in:

- Classical molecular dynamics.
- Semi-classical molecular dynamics.
- Quantum molecular dynamics (*ab initio* o Car-Parrinello⁷³).

The best description of biological systems is certainly mediated by the quantum MD, which solve the Schrodinger equation. Unfortunately, it is possible to solve exactly the Schrodinger equation only for a few particles, which implies that to find a valid approximate solution for a complex particles system, we need too high computational power. Nowadays, the systems studied through MD are becoming more and more complex, with a greater number of atoms and interactions, making the classical molecular dynamics very versatile to compute these systems. The term classical molecular dynamics indicates an extension through the Newton equations of motion, to the dynamic case of classical molecular mechanics (MM): molecules are characterized computationally as a function of parameters that express their physical characteristics through the laws that belong to classical physics.

In this way it is possible to implement systems with thousands of atoms, and using the MD tools, is possible to understand molecular mechanisms such as: receptor-ligand docking, protein folding and un-folding, drug delivery, protein free energies, polymer aggregation, multiscale modeling and much more.

3.2. Molecular mechanics

Molecular mechanics describes molecular systems through the use of classical mechanics. The potential energy of all particles is estimated as a function of the nuclear coordinates, assuming that the Born–Oppenheimer approximation is valid. Functional form and parameter sets used to calculate the potential energy for each type of atom of system are collected in Force Fields.

In general, MM is based on a simple parametrization model: atoms are represented by balls, which have mass as the real element mass, and bonds are represented by springs (using the Hook law) with an equilibrium distance equal to calculated bond length or equal to experimental data.

3.2.1. The potential energy function

As mentioned previously, potential energy function is defined in MM to modulate atom interactions. The potential energy is the sum of two macro-energy contributions, the potential energy of binding and the potential energy of non-binding interaction:

$$E(r^N) = E_{bonded}(r^N) + E_{non-bonded}(r^N) \quad (3.0)$$

$E(r^N)$ denotes the potential energy, which is in function of the position (r) of the N particles. These 2 categories are further subdivided into:

$$E_{bonded}(r^N) = E_{bonds}(r^N) + E_{angles}(r^N) + E_{dihedrals}(r^N) \quad (3.1)$$

$$E_{non-bond}(r^N) = E_{Van\ der\ Waals}(r^N) + E_{electrostatic}(r^N) \quad (3.2)$$

3.2.2. Bonded interactions

The covalent bond stretching contribution of expression (3.1) can be expressed by a harmonic potential (Figure 5-A):

$$E_{bonds}(r_{ij}) = \frac{1}{2} k_{ij} (r_{ij} - r_{0,ij})^2 \quad (3.3)$$

Where k_{ij} represents the bond stiffness and $r_{0,ij}$ represents the equilibrium distance. These parameters depend on the type of bound particles. For values that deviate a lot from the equilibrium distance, the potential energy increases proportionally a lot.

The angle vibration between 3 atoms i-j-k of expression (3.1) is also represented by a harmonic potential (Figure 5-B):

$$E_{angles}(\theta_{ijk}) = \frac{1}{2}k_{ijk}(\theta_{ijk} - \theta_{0,ijk})^2 \quad (3.4)$$

Where $\theta_{0,ijk}$ represents the angle equilibrium distance between the three atoms and k_{ijk} is the angle stiffness. The energy needed to distort an angle from its equilibrium position is less than the energy required to compress or stretch a bond, so the k_{ijk} applied to the angle harmonic potential is generally lower.

The third term of the expression (3.1) inserts an energy contribution that takes into account the torsional rotations between 4 atoms (Figure 5-C):

$$E_{dihedrals}(\phi_{ijkl}) = k_{ijkl}(1 + \cos(n\phi_{ijkl} - \phi_{0,ijkl})) \quad (3.5)$$

Where k_{ijkl} is the stiffness of the dihedral angle, n is called multiplicity, which gives the number of minimum points in the function, as the angle can rotate through 360° , and $\phi_{0,ijkl}$ determines where the torsional phases cross his minimum value. The imposition of torsion energy barriers is of central importance for understanding the structural properties of the molecules.

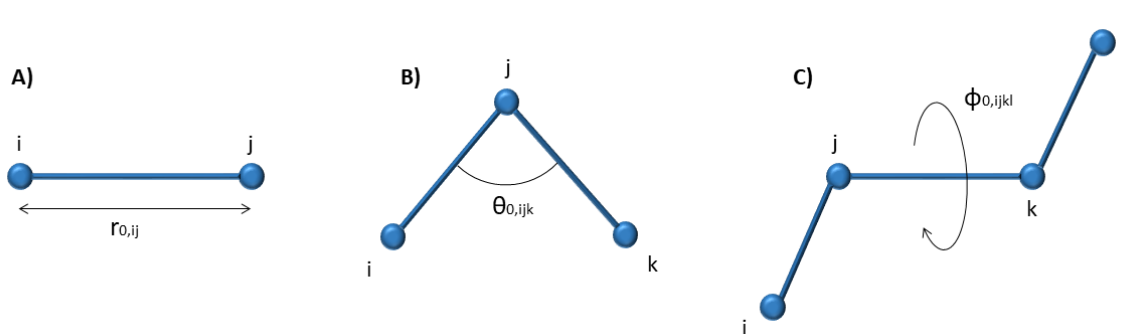


Figure 5: Qualitative representation of bonded parameters: **A)** bond between atoms i-j with equilibrium distance of $r_{0,ij}$ **B)** angle between atoms i-j-k with equilibrium angle of $\theta_{0,ijk}$ **C)** torsional angle between atoms i-j-k-l with equilibrium torsion angle of $\phi_{0,ijkl}$.

3.2.3. Non-bonded interactions

Atoms and molecules interact through non-bonded forces, which play a very important role in determining the structure of molecules. The non-bonded interactions are usually modelled as function of the inverse of distance, and therefore they don't depend upon a specific bond relationship between atoms. In the various force-field, non-bonded interactions are subdivided in two macro categories: Van der Waals interactions and electrostatic interactions (Figure 6).

Very electronegative atoms can attract the electronic cloud to itself, generating an uneven charge distribution in the molecule. The representation of this unequal charge field can be described by generating atomistic partial charges. The electrostatic interactions between different parts of the same molecule, or between different molecules, can be computed using the Coulomb law:

$$E_{electrostatic}(r_{ij}) = \frac{q_i q_j}{4\pi\epsilon_0 r_{ij}} \quad (3.6)$$

Where ϵ_0 is the electrical permittivity in the vacuum, r_{ij} is the distance between the charge q_i of the atom i and the charge q_j of the atom j . Electrostatic interaction is defined at long range interactions, because energy decreases with increasing distance.

In addition to the electrostatic interactions, there are also the Van der Waals interactions that contribute to the definition of the chemical-physical properties of the material. This type of interaction is classified as relatively weak, compared to, for example, a covalent bond, and consists in a repulsion or attraction generated in the neighborhood of 2 atoms due to the generated or induced displacement of the electrons, giving the London dispersion forces, Keesom forces and Debye forces.

The best representation of Van der Waals forces is mediated by the Lennard-Johnson⁷⁴ function:

$$E_{Van\ der\ Waals}(r_{ij}) = 4\epsilon \left[\left(\frac{\sigma_{ij}}{r_{ij}} \right)^{12} - \left(\frac{\sigma_{ij}}{r_{ij}} \right)^6 \right] \quad (3.7)$$

Where σ_{ij} represents the collision diameter, which is the distance where the energy is 0, and the ϵ represents the well depth of the potential energy.

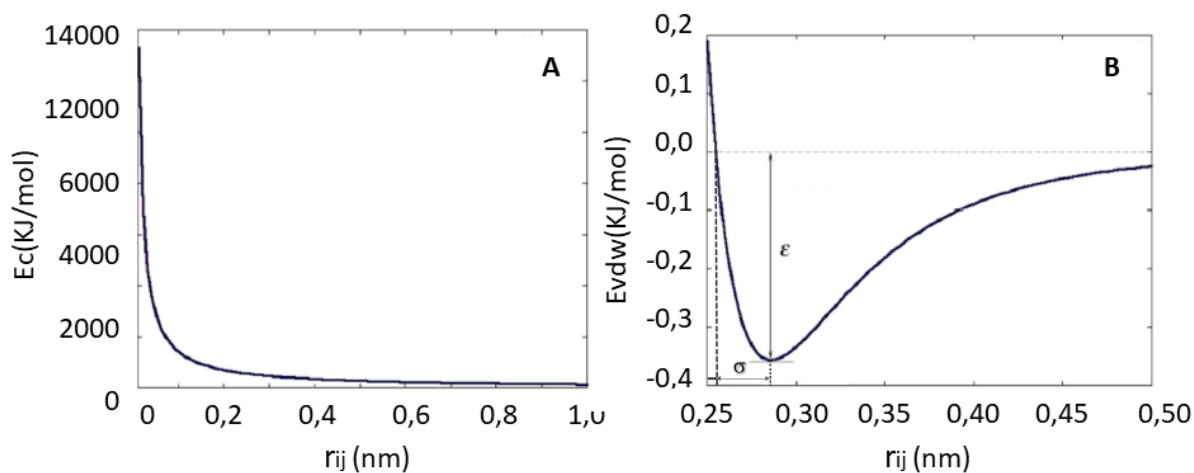


Figure 6: Representation of non-bonded interactions: **A)** Represents the Coulomb energy in function of distance r_{ij} between two atoms with the same charge. **B)** Represents the Lennard-Johnson energy as a function of distance r_{ij} ; where σ represents the collision diameter and the ϵ represents the well depth of the potential energy.

Calculation of non-bonded interactions requires a high computational effort, which can be improved using cut-off radii and using the Particle-mesh Ewald⁷⁵ (PME) for calculating the electrostatic interaction. Using cut-off radius implies that over that distance the non-bonded interactions are no longer calculated, simplifying the calculation of the interactions. PME is a method that places the charges within a grid with a specific spacing, which is transformed into the Fourier domain by means of a 3D FFT. The potential energy at the grid points is calculated by inverse transformation, and through interpolation factors we get the forces on each atom. The PME algorithm manages to scale with a $N \log N$ factor, making the calculation of the electrostatic forces substantially faster. An important requirement for the correct evaluation of the electrostatic energies of this algorithm is the use of periodic conditions.

3.2.4. Periodic boundary condition

Using the periodic boundary condition (PBC) is a very commonly used way to minimize edge effect in a theoretically infinite system. In a computational simulation study, we must necessarily have a finite system of particles in order to be simulated. The atoms of the system are solvated with water and neutralized with ions in a box that can be of the following types: *cubic*, *triclinic*, *dodecahedron*, *octahedron*. The obtained system is surrounded by translated copy of itself in the x, y, z directions (Figure 7). During the simulation only the energies and the properties of the original box must be

saved. When a particle passes from one side of the box, it returns with the same speed on the opposite side of the box. Using PBC inevitably leads to the generation of artifacts, which however are less serious than if we had the vacuum around the main box. As mentioned in the previous chapter, the PBC can be used together within PME algorithm to calculate the electrostatic interactions. In a system where there is the presence of electric charges, the total charge of the system must necessarily be neutralized to 0 coulomb, to avoid adding an infinite charge when the PBC are applied. Finally, the dimensions of the simulation box must be large enough to avoid PBC interaction artifacts.

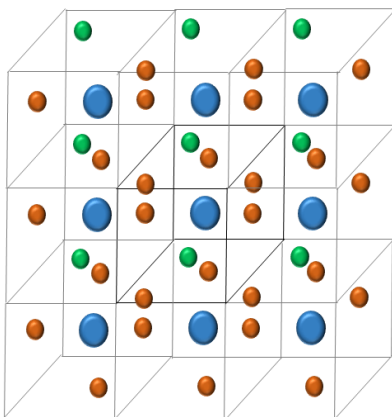


Figure 7: Scheme of system in periodic boundary condition (PBC) in 2D. The box in the center is the original box, surrounded by copy of itself.

3.2.5. Cut-off radius restrictions

As previously mentioned, the cut-off radii are used to truncate the non-bonded interactions beyond a certain threshold. Due to the use of PBC, the so-called minimum image convention is introduced:

$$R_C < \frac{1}{2} \min(\|a\|, \|b\|, \|c\|) \quad (3.8)$$

Where R_C is the cut-off radii and $\min(\|a\|, \|b\|, \|c\|)$ is the shortest box vector. The minimum image convention requires that the cut-off radius must not exceed half the shortest box vector, for not having more than one image within the cut-off radius. This rule may generally not be enough, in fact, extending the concept of minimum image convention we should have a length of the box vector that exceeds at least the length of the studied molecule projected along that direction, plus 2 times the radius of cut-off.

3.3. Molecular dynamics

MD is a discipline that through the integration of Newton's equations manages to predict the dynamics of the evolution of a physical-chemical system. More generally MD is a theoretical/computational algorithm which can calculate average proprieties of a system by sequentially sampling microstates ensemble in time. Generic scheme of the MD operation is shown in Figure 8:

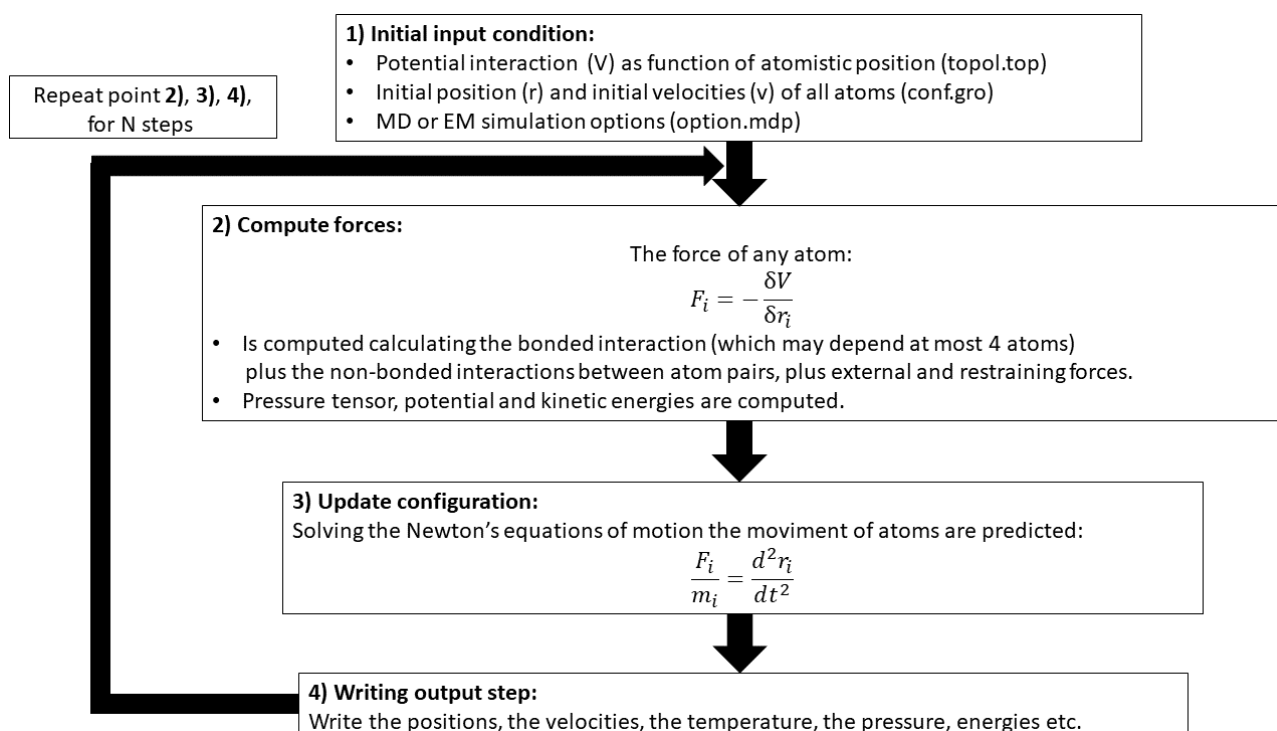


Figure 8: General scheme of MD algorithm. From the initial conditions the potential energies are calculated. Forces acting on the atoms are derived from energies and through the integration of Newton's equations, new positions and velocities of the system are predicted. The cycle is repeated for the N steps set at the start.

3.3.1. Statistical ensembles

In statistical mechanics and in thermodynamics, statistical ensembles are the set of all those different microstates in which the system can be found that have the same macroscopic or thermodynamic state. The microscopic state of a system is defined by the position and the momentum of a particle.

These coordinates, considering a multidimensional space, can be called “phase space”. Every single point in the phase space describes a microstate of the system, and the collection of points that are in the same thermodynamic state, define a thermodynamic ensemble. In 1902 Willard Gibbs defined 3 important thermodynamic ensembles, *Micro-canonical*, *Canonical* and *Grand-canonical*, to whom we also consider a fourth case that is the *Isothermal-isobaric* ensemble⁷⁶ (Figure 9):

- Micro-canonical (NVE): corresponds to a system that can't exchange energy and material with universe (isolated), that has constant number of particles, volume and total energy.
- Canonical (NVT): corresponds to a rigid box vectors system that can't exchange material, but can exchange energy with universe (closed), that has constant number of particles, volume and temperature.
- Grand-canonical (μVT): corresponds to a system that can exchange material and energy with universe (open), that has constant chemical potential, volume and temperature.
- Isothermal-isobaric (NPT): corresponds to a system that can't exchange material, but can exchange energy with universe (closed) with the possibility to change the box vectors, that has constant chemical number of particles, pressure and temperature.

Statistical thermodynamic ensembles

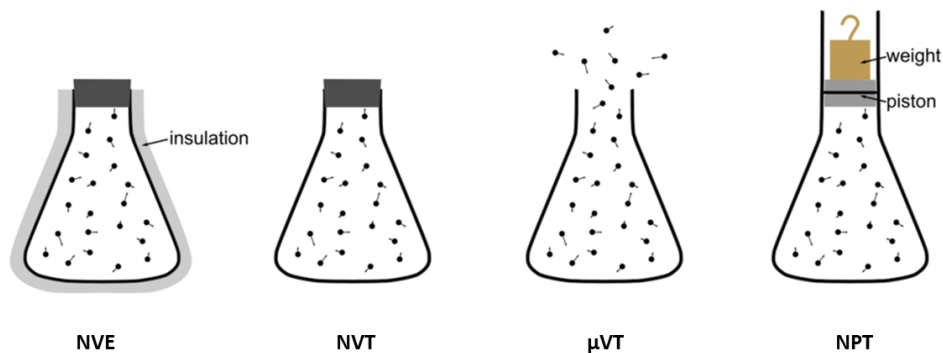


Figure 9: Schematic representation of the 4 thermodynamic ensembles: Micro-canonical (NVE), canonical (NVT), grand-canonical (μVT), isothermal-isobaric (NPT).

There are two ways to generate a representative statistical ensemble of the system taken into consideration: MD simulation or Monte Carlo simulations. These methods are able to calculate the ensemble average of a macroscopic state through the sampling of the microstates from the phase space, in a way that well approximates the equilibrium of the macroscopic state. The ensemble average of a propriety A can be expressed in the following way:

$$\langle A \rangle_{ensemble} = \int \int A(p^N, q^N) \rho(p^N, q^N) dp^N dq^N \quad (3.9)$$

Where $A(p^N, q^N)$ is the observable of interest, p is the position of the N atoms, q is the momentum of the N atoms and $\rho(p^N, q^N)$ is called the ensemble density of probability function:

$$\rho(p^N, q^N) = \frac{1}{Q} \exp \left[-\frac{H(p^N, q^N)}{k_B T} \right] \quad (3.10)$$

Where k_B is the Boltzmann's constant, T is the absolute temperature, $H(p^N, q^N)$ is the Hamiltonian and Q is the expression of the canonical discrete partition function:

$$Q = \sum_i \exp[-\beta E_i] = \sum_i \exp \left[-\frac{1}{k_B T} E_i \right] \quad (3.11)$$

Where k_B is the Boltzmann's constant, T is the absolute temperature and E_i is the total energy of the system in the i -microstates. The canonical partition function describes the thermodynamic and statistical properties of a system by normalizing sum of Boltzmann's factors over all microstates. Discrete partition function is dimensionless and can be further extended to the continuous by replacing the summation with an integral operator:

$$Q = \int \int \exp \left[-\frac{H(p^N, q^N)}{k_B T} \right] dp^N dq^N \quad (3.12)$$

Equation 3.12 is crucial to have the connection between the thermodynamic microstates' variable, which we can't measure, and the thermodynamic macroscopic state, which we can measure. Unfortunately, the calculation of this integral is very complex because it considers all the possible microstates of the system. A way to simplify the problem is to use the *ergodic hypothesis*.

3.3.2. Ergodic hypothesis

The calculation of the integral of equation 3.12 is extremely complex to solve. The use of the ergodic hypothesis is a way to overcome this problem. In thermodynamics and in physics, the statement of ergodic hypothesis expresses that, over long periods of time, all microstates are equiprobable accessible. Practically, it means that the time spent by a particle in a volume in the space phases of the microstate with the same energy is proportional to the volume itself. The usefulness of the ergodic hypothesis is that it allows to evaluate macroscopic quantities, as an average on microstates instead of a temporal average.

$$\langle A \rangle_{ensemble} = \langle A \rangle_{time} \quad (3.13)$$

Therefore, we can compute the ensemble average of propriety A using the time average of the same propriety:

$$\langle A \rangle_{time} = \lim_{\tau \rightarrow \infty} \frac{1}{\tau} \int_{t=0}^{\tau} A(p^N(t), q^N(t)) dt \approx \frac{1}{M} \sum_{t=0}^M A(p^N, q^N) \quad (3.14)$$

Where t is the simulation time, M is the number of time steps and $A(p^N, q^N)$ is the instantaneous value of the propriety A.

3.3.3. Energy minimization

In MD, the energy minimization (EM) process is a method by which the atomic structure of a system is optimized by searching for local minimum potential energy (local stationary point) in the potential energy surface (PES). We can only find the nearest local minimum from the starting point in PES, because most of the optimization algorithms are unidirectional in the minimum searching, allowing only downhill movements. The minimization process is able to reduce the potential energy by lowering the inter-atomic interaction forces, bringing them ideally close to 0. Minimization algorithms can be classified in two categories:

- Derivative methods, like *steepest descent*, *conjugate gradient* and *Newton-Rapson* method.
- Non derivative methods, like *simplex* method.

The most used algorithms are those of a derivative type, which are able to give information about the shape of the energy surface, and can improve the efficiency of the minimum searching. Steepest descent method (Figure 10) is the most used algorithm in molecular dynamics because is the most robust and easy to implement process, even if isn't the most efficient searching method. This EM algorithm firstly calculate di force F from the negative gradient of potential energy V , then new position is computed in the following way:

$$r_{n+1} = r_n + \frac{F_n}{\max(|F_n|)} h_n \quad (3.15)$$

Where r_{n+1} is the new position, r_n is the actual position, F_n is the force and h_n is the maximum displacement initially selected (for example 0.01 nm). If the $V_{n+1} < V_n$ the new positions are accepted and $h_{n+1} = 1.2h_n$, but if the $V_{n+1} > V_n$ the new positions are not accepted and $h_n = 0.2h_n$. The code stops when the maximum number of force evaluation steps has been reached, or when the

maximum of the absolute value of force is less than a certain ϵ value, which is considered acceptable between 1 and 10.

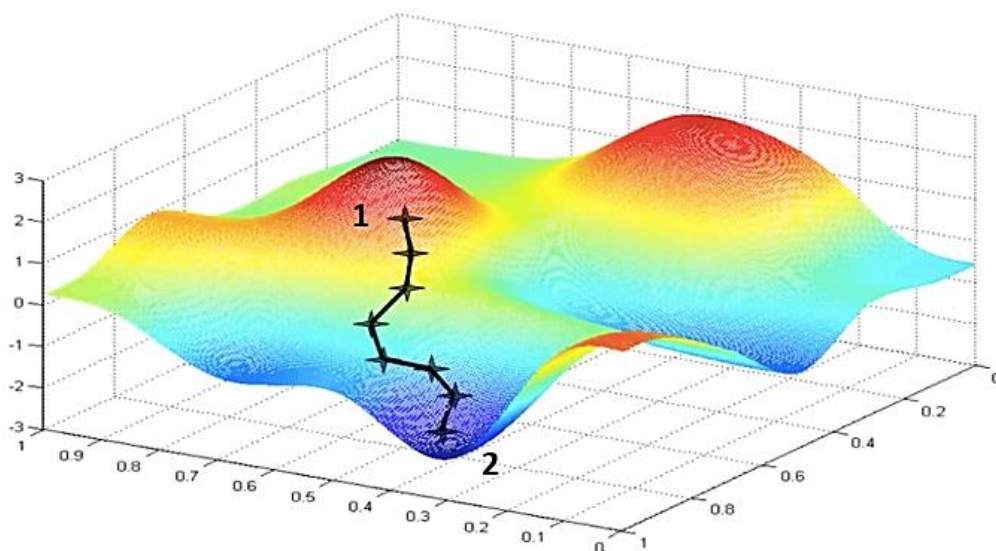


Figure 10: Potential energy surface (PES) with illustrated an example of Energy minimization (EM) sequence by the steepest descent algorithm. **1** represent the initial conformational state which correspond to a point on PES surface. Similarly, **2** represent the final conformational state, after EM, which correspond to a point on PES surface.

3.3.4. Leapfrog integrator

In MD the leapfrog algorithm⁷⁷ is a numerically method that by integrating differential equations of motions produces an output trajectory. The leapfrog integration method (Figure 11) uses the position r of atoms at moment t and the velocity v at a previous time $t = t - \frac{1}{2}\Delta t$ updating positions and velocities using the forces on atoms F at time t , through the following relations:

$$v\left(t + \frac{1}{2}\Delta t\right) = v\left(t - \frac{1}{2}\Delta t\right) + \frac{\Delta t}{m}F(t) \quad (3.16)$$

$$r(t + \Delta t) = r(t) + \Delta t v\left(t + \frac{1}{2}\Delta t\right) \quad (3.17)$$

The leapfrog algorithm is time reversible of third order in r and produces trajectories whit the following position-update equation:

$$r(t + \Delta t) = 2r(t) - r(t - \Delta t) + \frac{1}{m}F(t)\Delta t^2 + O(\Delta t^4) \quad (3.18)$$

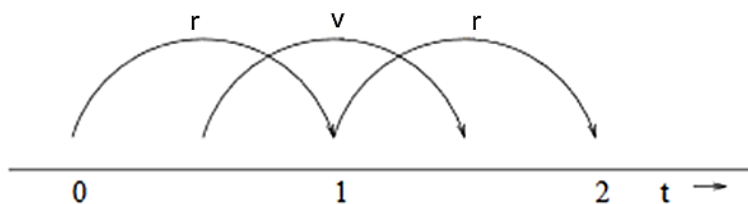


Figure 11: Scheme of the leapfrog algorithm, where r is the position, v is the velocity and t is time. This method is called leapfrog because positions and velocities are leaping like frog over a Δt time difference.

3.3.5. Constraint algorithm

In a simulation process the relative position of atoms from other atoms, described by the topologies, must be maintained in a certain oscillation range. The use of a constraint algorithm serves to prevent that the distance of the masses between 2 atoms come out of the limits imposed by the chemical-physics relations. Generally, in MD the covalent distance between heavy atoms and hydrogen atoms are constrained for enhancing the computational efficiency by reducing the vibrational component along some degrees of freedom. The constraint methods often used in MD simulation are typically: *Shake* and *Lincs*⁷⁸ algorithm.

Lincs is a non-iterative algorithm that use two steps, which can restore bonds to the correct covalent distance after an unconstrained updated. If we consider a N system particles, with $3N$ position saved in a $r(t)$ vector, the dynamic equations of motion using the Newton law will be:

$$\frac{d^2r}{dt^2} = M^{-1}F \quad (3.19)$$

Where M is a $3N \times 3N$ matrix containing the masses of the atoms and F is the $3N$ force vector. In the first step, Lincs algorithm, calculate the projection of the new bonds to the old ones, setting up their values to 0, while in the second step, is applied a correction on the bonds distance caused by the unconstrained rotation. The mathematics behind the Lincs algorithm is complicated but is possible to summarize it by saying that is based on an inversion of a matrix A in which all the directions of the various constraints are contained. The inversion operation is used to calculate the correction to be

applied to the length of the bond, which has undergone an unconstrained rotation. Method used for inverting matrix A is:

$$(I - A)^{-1} = I + A + A^2 + A^3 + A^N \quad (3.20)$$

Where I is the identity matrix, A is the symmetrical invertible matrix which has all 0 on the diagonal and N is the expansion factor which determine the accuracy of the Lincs method. In an atomistic simulation the expansion factor generally used is 4, but for simulation with a higher time step, it may be necessary to use a factor between 6 and 8 to maintain the correct accuracy and stability.

3.3.6. Temperature coupling

MD software can implement a number of weak-coupling scheme to simulate a constant temperature coupling to an external bath, which can be: *Berendsen*⁷⁹, *V-rescale*⁸⁰, *Nosé-Hoover*⁸¹ and *Andersen*⁸² scheme. The aim of these algorithms is to rescale the kinetic velocities of the atoms by considering the temperature coupling of the system to an external bath.

The Berendsen algorithm carry out a weak coupling scheme at a temperature T_0 implementing a correction on the system in accordance with:

$$\frac{dT}{dt} = \frac{T_0 - T}{\tau} \quad (3.21)$$

Which controls the temperature deviation by an exponential decay with a time constant τ , set by user as input parameters. Temperature control is imposed by the velocities rescaling on each atom for each step of the simulation, by time depend factor λ :

$$\lambda = \sqrt[2]{1 + \frac{n_{TC}\Delta t}{\tau_T} \left(\frac{T_0}{T(t-1/2\Delta t)} - 1 \right)} \quad (3.22)$$

Where n_{TC} is the time step, λ is the scaling factor which is limited in the range $0.8 < \lambda < 1.25$ for stability issues and τ_T is a time constant close to τ in equation 3.21, which can be joint by the relation:

$$\tau = \frac{2C_V\tau_T}{N_{df}k} \quad (3.23)$$

Where C_V is the total heat capacity of the system, N_{df} is the total degrees of freedom of the system and k is the constant of Boltzmann.

V-rescale algorithm is essentially based on the previous mentioned Berendsen scheme, with in addition a stochastic term, which implements a greater correctness in the modification of the kinetic energy distribution:

$$dK = (K_0 - K) \frac{dt}{\tau_T} + 2 \sqrt{\frac{KK_0}{N_{df}}} \frac{dW}{\sqrt{\tau_T}} \quad (3.24)$$

Where K is the kinetic energy, dW is a Wiener process. The advantage of this scheme is that produces a correct canonical ensemble by maintaining the positives side of the Berendsen thermostat, which are:

- No oscillation in the velocity rescaling
- First order decay of the temperature deviations

3.3.7. Pressure coupling

As in the case of the temperature coupling mentioned above, the MD algorithms can also perform coupling with an external pressure bath. The Most used pressure barostat are: *Berendsen*⁷⁹ and *Parrinello-Rahman*⁸³ scheme.

The Berendsen weak pressure coupling method can exercise good control over the correct average pressure, but it doesn't yield the correct NPT ensemble, so is a good algorithm to equilibrate systems when they have to be pressure coupled, but is not recommended for MD production runs. The Berendsen algorithm carry out a coupling scheme at a pressure P_0 implementing box vectors rescaling every step n_{PC} with a matrix μ in accordance with:

$$\frac{dP}{dt} = \frac{P_0 - P}{\tau_P} \quad (3.25)$$

The scaling matrix μ is defined as follow:

$$\mu_{ij} = \delta_{ij} - \frac{n_{PC} \Delta t}{3\tau_P} \beta_{ij} \{P_{0ij} - P_{ij}\} \quad (3.26)$$

Where δ_{ij} is the identity matrix, τ_P is the time constant, β_{ij} is the isothermal compressibility of the system, for water at 1 atm and 300K $\beta_{ij} = 4,6 \times 10^{-5} \text{bar}^{-1}$. The Berendsen scaling can be applied in all directions (isotropic) or can be done in anisotropic way, but it may be necessary to increase the time constant τ_P or reduce the time step n_{PC} to avoid errors from the constraint algorithm.

Parrinello-Rahman approach in theory, can yield the true NPT ensemble, but also allow a higher pressure fluctuations. For this reason, it is a good scheme for MD production run, but isn't a recommended coupling barostat for equilibration, because it can crush the simulation for the large box vectors oscillation. Parrinello-Rahman algorithm scales the box vectors, represented by the matrix b in accordance with the equation:

$$\frac{db^2}{dt^2} = VW^{-1}b'^{-1}(P - P_0) \quad (3.27)$$

Where V is the box volume, W^{-1} is the matrix with the coupling strength parameters and P is the pressure. The equations of motions for the atoms are also rescaled:

$$\frac{d^2r_i}{dt^2} = \frac{F_i}{m_i} - \left\{ b^{-1} \left[b \frac{db'}{dt} + \frac{db}{dt} b' \right] b'^{-1} \right\} \frac{dr_i}{dt} \quad (3.28)$$

The box deformation is determined by the matrix W^{-1} which determines the strength of pressure coupling:

$$W^{-1}_{ij} = \frac{4\pi^2 \beta_{ij}}{3\tau_p^2 L} \quad (3.29)$$

Where β_{ij} is the isothermal compressibility, τ_p is the pressure time constant and L is the largest box matrix element.

3.4. Simulated annealing

In computational bio-chemistry, simulated annealing^{84,85} (SA), showed in Figure 12, is a probabilistic technique of enhanced sampling, which aims to find a global minimum by providing the system with the energy needed to get out of the current local minimum and fall into another minimum. Energy is supplied to the system by increasing the temperature. By exploring a different minimum each time, the probability of ending the global minimum increases.

Simulated annealing process

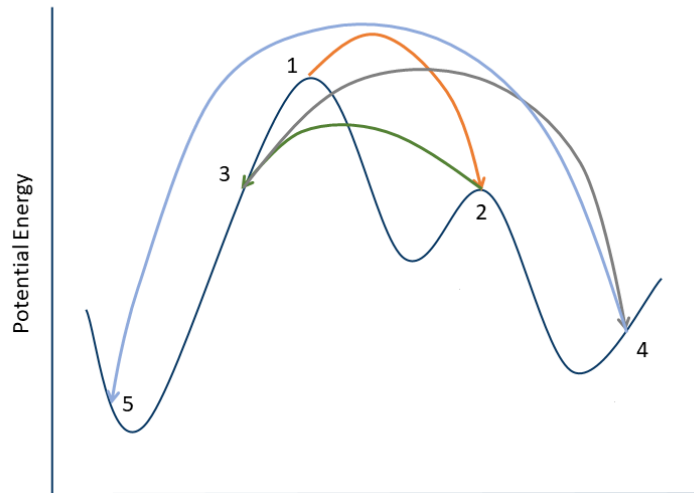


Figure 12: Simulated annealing procedure scheme: The system starts at point 1 then with cycles of increasing and decreasing temperature, the system explores other potential energy minimum, finishing at the end at point 5.

The annealing protocol is set as a series of reference temperature that correspond to a specific time implemented for each group, and computed with a specific sequence:

- *Single*, for a single annealing sequence and then coupled to the reference T_0 temperature until the end of simulation.
- *Periodic*, with a periodic annealing sequence until the finish of simulation.

3.5. Coarse Grained modelling

Coarse grained (CG) modelling⁸⁶ is a way to reduce the degrees of freedom of a system of atoms in order to increase integration time steps allowing faster simulation. To obtain this result, groups of atoms are replaced by a single bead, positioned in the center of mass or center of geometry of the atoms group. This procedure inevitably leads to the loss of degrees of freedom, with consequent greater easiness for the calculation of the potential energy function, due to the reduced presence of bonded parameters and the increased simplicity of the non-bonded parameters. The greater simplicity of the non-bond parameters is due to the use of cut-offs for the calculation of Van der Waals and electrostatic potential energy, which allow faster computation instead of using, for example, the

expensive algorithm PME for the electrostatic potential energy. CG models to be usable must reproduce the same properties of the original atomistic model. There are different methods for deriving the CG force field depending on the type of property we want to preserve:

- Conserving forces: *Force matching*⁸⁷.
- Conserving free energies: *Simplex* method, *Martini* force field⁸⁸.
- Conserving the distribution function: *Iterative Boltzmann Inversion*^{89,90}, *Inverse Monte Carlo*⁹¹.

3.5.1. Martini force-field

The first CG force-field developed thanks to the group headed by Siewert Marrink, professor at the University of Groningen in 2004 was exclusively for lipids. The name “Martini” was coined only later, with the release of the version 2.0 for lipids because it interestingly reflects the universality of the famous cocktail with the same name: how a few simple ingredients, in force-field specific cases the chemical building blocks, can be endlessly varied to create a complex combination of taste. Due to the notably success achieved, Marrink’ group subsequently extended the force-field to a plenty of biomolecules, including proteins and peptides⁹², carbohydrates⁹³, polymers⁹⁴ and DNA⁹⁵. The philosophy behind Martini methodology wasn’t to capture every single detail of a given atomistic simulation, but rather to create an extendable CG model based on simple modular building blocks, using few parameters and standard interaction potentials to maximize applicability and transferability⁸⁸. Instead of focusing on the accurate emulation of conformational details at a selected state for a specific system, they aimed for a wider range of applications without the necessity to re-parameterize the model each time. Martini methodology follow a top-down approach by extensive calibration of the non-bonded interactions of the chemical building blocks based on experimental data. In particular, a specific thermodynamic parameter, the free energy (ΔG), was used as the reference data set to calibrate CG blocks by computing oil/water partitioning coefficients.

Force-field details

Most updated interaction sites model consists on average a four-to-one atom condensation in a single interaction center. Hydrogen atoms are not considered in the mapping strategy, because they have low molecular weight. On the one hand, maps are aimed to achieve a good computational efficiency

and on the other hand, are aimed to reach a well chemical representation. In order to keep the model as simple as possible, four main types of interaction sites are developed: polar (P), nonpolar (N), apolar (C), and charged (Q)⁸⁸. Each particle type has a number of subtypes, which allow more accurate representation of the chemical nature of the underlying atomic structure. In total, 18 different type of interacting particles are generated. Particles subtype are furthermore distinguished by division in hydrogen bonding capabilities (“d” indicates donor, “a” indicates acceptor, “da” for both, 0 for no-one), or by a number which indicate the polarity degree (from 1, low polarity, to 5, high polarity). Moreover, for preserving purposes of the small ring compounds geometry, a four-to-one mapping procedure isn’t the best choice. The strategy adopted to model rings is typically composed by 2 or 3 atoms into CG beads 1 mapping⁸⁸. With this more detailed mapping, enough geometrical detail is kept to mimic the geometry of small compounds such as cyclohexane or benzene and sterol bodies such as cholesterol.

Bonded interaction

Bonded interactions are described by a standard set of potential energy functions, as commonly used in standard force fields, including as usual harmonic bond and angle potentials, and multimodal dihedral potentials ([section 3.2.2.](#)). To parameterize the bonded interactions, structural data are used either directly derived from the underlying atomistic geometry (such as bond lengths of rigid structures) or obtained from comparison to atomistic simulations. To parametrize CG bonded interaction the following procedure is adopted:

1. Higher resolution simulations are firstly converted into a mapped CG structure by identifying the center of mass (COM) of the corresponding atoms.
2. Secondly, the distribution functions are derived for the atomistic mapped simulation and compared to those obtained from a real CG simulation.
3. Finally, the CG parameters are systematically tuned in an iterative way until satisfactory overlap of the distribution functions is obtained (for example iterative Boltzmann inversion).

Non-bonded interactions

Non-bonded interactions are described by a Lennard-Jones 12-6 potential ([section 3.2.3.](#)). The strength of the interaction, determined by the value of the Lennard-Jones well-depth ϵ_{ij} , depends on the interacting particle types i ; j . The value of ϵ ranges from $\epsilon_{ij} = 5,6\text{kJ} = (\text{mol A})$ for interactions

between strongly polar groups to $\epsilon_{ij} = 2,0\text{kJ} = (\text{mol A})$ for interactions between polar and apolar groups, mimicking the hydrophobic effect. The effective size of the particles is governed by the Lennard-Jones parameter $\sigma = 0.47\text{nm}$ for all normal particle types. As a consequence of the large density of CG beads, the interaction parameters for ring particles need special treatment: a further site labelled S is used, whose effective interaction size and strength is reduced compared to the normal set. Specifically, the σ of the LJ potential is set to 0.43 rather than 0.47 nm and the ϵ is scaled to 75% of the value of normal particles. This allows ring particles to pack more closely together without freezing, which allows reproduction of the liquid densities of small ring compounds while retaining the correct partitioning behavior. In addition to the LJ interaction, charged groups (type Q) bear a charge $\pm e$ and interact via a Coulomb energy function ([section 3.2.3.](#)). Coulomb interactions are screened implicitly with a relative dielectric constant $\epsilon_{\text{rel}} = 15$ to account for the reduced set of partial charges and resulting dipoles that occur in an atomistic force field. The non-bonded interactions of the Martini model have been parameterized based on a systematic comparison to experimental thermodynamic data. Specifically, the free energy of hydration, the free energy of vaporization, and the partitioning free energies between water and a number of organic phases were calculated for each of the 18 different CG particle types.

Water

Antifreeze particles. Main problem suffered by the CG water model, modelled as P₄ particles, is the freezing temperature that is too high compared to real water. Depending on the simulation conditions, the CG water may frequently freeze between 280 K and 300 K. In order to hinder such unpleasant freezing of the CG water an antifreeze bead is needed. The so-called antifreeze beads, which interact as a special particle type denoted BP₄⁸⁸ (which mean Big P₄), has been introduced to prevent water freezing. Special BP₄ particle is projected to disturb the lattice packing of the solvent particles using an different Lennard-Jones parameter σ , scaled up to 0.57 nm from the standard value of 0.47 nm⁸⁸. Nevertheless, the interactions of BP₄ particle with all of the other type of particle, even including the self-interaction, remain the same as for normal CG water. If only a small amount (substitution of 10% of normal P₄ bead appears to work effectively) of the normal water beads is replaced by the antifreeze particles, freezing phenomenon is no more observed unless the temperature reach a level well below the freezing temperature of real water. For example, if 10% of normal water particles is replaced by antifreeze particles, the freezing condition occurs below 250 K.

Polarizable water. Martini water beads, as many other CG water models present in literature, isn't provided with charges, making them blind to external electrostatic fields and local polarization effects. In order to compensate the neglect of explicit polarization, screening of electrostatic interactions is done implicitly, assuming a uniform relative dielectric constant. Martini normal water beads seems to be a reasonable approximation for bulk water, but problems arise at the interfaces between water and other phases and in the proximity of charged particles. For this reason, to allow the modelling of water interaction with charged particles (Q) in a more realistic way a polarizable CG water model⁹⁶ has been developed. The polarizable CG water is composed by three particles instead of the one used in the standard MARTINI force field⁸⁸. The central particle "W" is neutral and interacts with other particles present in the system by standard Lennard-Jones interactions. Additional particles WP and WM are bound to the central one "W" and carry a positive and negative charge respectively, of +q and -q. Just mentioned charged particles interact with the environment particles by only the Coulomb long range electrostatics force. In addition, the bonds between W-WP and W-WM are constrained to a distance of 0.14 nm⁹⁶. Compared to the standard MARTINI water model, the polarizable model has improved properties, not only in comparison to its dielectric attitude, but also for instance in the reducing of water freezing point. Evidences indicate that the polarizable water model reproduces most of the crucial properties, like dielectric constant, radial distribution functions and the diffusion behavior, in satisfactorily agreement with atomistic force field results and experimental findings when a rescaling approach is used.

Ions

Martini force field models atomistic ions as CG charged bead⁸⁸, with 1:1 equivalence:

- Positive charged particle for Na ions with unitary +1 charge.
- Negative charged particle for Cl ions with unitary -1 charge.

Non-bonded parameters. The non-bonded interactions are set with a cut-off distance of, $r_{\text{cut}} = 1.2$ nm like in the atomistic simulation. To avoid generation of unwanted noise, in the original papers of MARTINI CG force-field, the standard shift function of the GROMACS software package is used in which both the energy and force vanish at the cut-off distance: the Lennard-Jones potential is shifted from $r_{\text{shift}} = 0.9$ nm to r_{cut} . The electrostatic potential is shifted from $r_{\text{shift}} = 0.0$ nm to r_{cut} . However, this type of implementation doesn't allow the use of GPUs to accelerate the computation in GROMACS package. Besides that, Lennard-Jones and Coulomb potentials are implemented with the

potentials shifted to zero when is reached the cutoff distance using the so called “Potential modifiers” provided by the software package. The modified potentials, in addition to allowing the implementation of GPUs to accelerate the elaboration process in GROMACS, are demonstrated to have little influence on most of the properties of the system, including partitioning free energies, bulk liquid properties and bilayer properties, keeping the energy conservation within reasonable bounds. In recent developments, r_{cut} has been demonstrated to allow well computation of the non-bonded potential even with a value of 1.1⁹⁷, still maintaining the potential modifiers. Assuming this recent values of r_{cut} , MD simulations might additionally benefit of a boosting time performance, which further improve efficiency of computational hardware⁹⁷.

Time-step. Generally, a time-step varying from 40 fs to 20 fs is used. However, the use of the correct time-step leads to a controversial debate. In their work Winger *et al.* state that, since the MARTINI CG model involves the same functional form of the all-atom force-field (where a time-step varying from 0.5 to 2 fs is used) for the interaction function (a r^{-12} , r^{-6} , and r^{-1} distance-dependence) of the non-bonded interaction, it is unlikely that it can be used with a ten or more times longer time step. They investigated this issue and showed that time steps larger than 10 fs lead to very poor integration of the equations of motion, resulting in average values of properties, e.g. temperatures, which are different from the correct ones. Following this publication, the group of Marrink answered that Martini simulations generally are stable with time-steps of up to 40 fs or 20 fs in the presence of rings such as in cholesterol or proteins. Lower values than 20 fs is considered an inefficient use of computer time as errors in the model will strongly dominate errors due to numerical integration time steps.

Interpretation of the time scale

In general, the interpretation of the time scale in CG simulations is not straightforward. In comparison to atomistic models, the dynamics observed with CG models is faster. The main reason is that the underlying energy landscape is much smoother as a result of the larger particle sizes. On the basis of comparison of diffusion constants in CG and atomistic modelled systems, the effective time sampled using MARTINI CG model was found to be 2- to 10-fold larger. The standard conversion factor used is a factor of 4, which is the speed up factor in the diffusional dynamics of CG water compared to real water.

3.5.2. Modified Boltzmann inversion

CG simulation method⁸⁶ has been proven in recently years as efficient and reliable commonly used technique to explore biological systems for greater length and time scales in comparison with atomistic method. To allow the switching from atomistic to CG models significant efforts must be performed in generating the correct bond parameters in order to emulate also the atomistic mechanical proprieties. Topological parameters adopted in CG simulations are often derived using one of the cited technics in previously chapter, like for example iterative Boltzmann inversion^{89,90} (IBI). IBI methodology is based on the Boltzmann inversion^{98,99} equation:

$$V(r) = -k_B T \ln(g(r)) \quad (3.30)$$

Where $V(r)$ is the potential energy, k_B is the constant of Boltzmann, T is absolute temperature and $g(r)$ is the distribution function between a pair of sites. Afterwards, iteration process begins, leading in a correction of starting potential:

$$V_{i+1}(r) = V_i - \alpha k_B T \frac{\ln(g(r)_i)}{\ln(g(r)_{i+1})} \quad (3.31)$$

Where V_{i+1} is the actual potential energy, V_i is the previous potential energy, k_B is the constant of Boltzmann, T is absolute temperature, $g(r)_{i+1}$ is the distribution function and α is called dumping factor which prevents abnormal variation of the potential energy, during the iteration procedure. Extracting the distribution function $g(r)$ from equation (3.30) we can obtain the following equivalence:

$$e^{-V(r)/k_B T} = e^{-K(x-\mu)^2/2k_B T} \quad (3.32)$$

$$e^{-(x-\mu)^2/2\sigma^2} \leftrightarrow e^{-K(x-\mu)^2/2k_B T} \quad (3.33)$$

Where $\frac{K(x-\mu)^2}{2}$ is a generic harmonic potential $V(r)$. Equivalence 3.33 is valid only if is true that the standardized normal distribution (Gauss distribution) can be considered equivalent to the target functional form, since taking the assumption of independent degrees of freedom, and hence no correlation. Finally, simply replacing new assumed $g(r)$ in the equation 3.30, it results:

$$V(r) = -k_B T \ln(g(r)) = -k_B T \ln(e^{-(x-\mu)^2/2\sigma^2}) = -k_B T \frac{-(x-\mu)^2}{2\sigma^2} \quad (3.34)$$

$$V(r) = -\frac{K(x-\mu)^2}{2} = -k_B T \frac{-(x-\mu)^2}{2\sigma^2} = \frac{k_B T}{\sigma^2} \quad (3.35)$$

Such particular computing method of Boltzmann inversion^{98,99} technique is applicable for the estimation of the bonds, angles and constraint topological parameters, only using standard deviation σ to get harmonic constant K . As for IBI computation, even equation 3.35 can be used to implement an iterative modified Boltzmann inversion:

$$V_{i+1}(r) = V_i(r) \pm \beta V_i(r) \frac{\sigma_{i+1}^2}{\sigma_i^2} \quad (3.35)$$

Where β is a value with the aim of modulating abrupt variation of potential energy values, like IBI-dumping constant, which range is from 0 to 1. In conclusion, the correction factor $+\beta V_i(r) \frac{\sigma_{i+1}^2}{\sigma_i^2}$ is adopted if σ_{i+1}^2 is greater than σ_i^2 , contrariwise $-\beta V_i(r) \frac{\sigma_{i+1}^2}{\sigma_i^2}$ is selected if σ_{i+1}^2 is lower than σ_i^2 .

4. Coarse Grained dendrimers models

4.1. Introduction

Interaction properties between dendrimer-dendrimer and between dendrimer-siRNA are the key investigation topics to achieve in this master thesis work. To increase the knowledge of the aggregation phenomena which occurs between morpholinium (DM) or pyrrolidinium (DP) dendrimers and siRNAs, requires the simulation of systems composed of high number of atoms. Molecular dynamics (MD) simulations of a system at the atomic level are very expensive from a computational point of view. An alternative way to perform these investigations over longer time periods, maintaining the same computational effort, is the use of the coarse grained (CG) method through Martini force-field^{88,100}. CG approach is one of the most used way to find compromise between increased simulation times with an acceptable loss of accuracy, due to decreased degrees of freedom⁸⁶. Nowadays, many CG models for PAMAM¹⁰¹ or poly(L-lysine)¹⁰² dendrimers has been used to carry out long time MD for aggregation purposes¹⁰³ or for interaction with cellular membrane^{104,105}. Despite the long time since Martini force-field was adopted in computational studies, in recent literature, no CG models of DM and DP cationic phosphorous dendrimers were developed yet. The lack of data around these specific class of dendrimer, paved the way for the development of a new DM and DP dendrimer models. To achieve this goal, we adopted a method for constructing the CG model based on the atomistic MD trajectory, from which the starting bonded parameters were obtained. Calculation of topological parameters has been carried out using a variant of iterative Boltzmann inversion⁸⁹ technique. Subsequently, the CG models have been optimized following two different strategies: A) suit the bonded parameters as similar as possible to the atomistic models and B) try to optimize the conformational features of the dendrimers as close as possible to the atomistic simulations. Then supramolecular characteristics of above mentioned dendrimers were investigated by CG molecular dynamics as for example DM and DP self-assemble behavior highlighted by *in vitro* experiments²⁷.

4.2. Materials and methods

4.2.1. Atomistic Simulation

DM and DP dendrimer 3D models has been generated using Avogadro chemical editor¹⁰⁶. RESP fitting method at the HF/6-31G level of theory using AM1-BCC charges was adopted to define atoms partial charge. The General Amber Force Field (GAFF)¹⁰⁷ has been chosen to describe dendrimers topologies. Therefore, each dendrimer was set in the center of dodecahedron box, solvated with water and filled with ions (Cl⁻ and Na⁺) at concentration of 0.15M. GROMACS 5.0^{108,109} package was adopted for performing MD simulations. Position restrain MD of 100 ps in respectively NVT ensemble using v-rescale⁸⁰ thermostat at 300 K and NPT ensemble using Berendsen⁷⁹ barostat at 1 atm was carried out after a process of 1000 steps of steepest descent energy minimization. Production MD simulation of 500 ns in NPT ensemble using Parinello-Rahman⁸³ barostat, was performed on both dendrimers (Figure 13). We used previously simulation parameters as described in the paper of Deriu *et al*²⁷. Longer simulation time has been set up in order to gather more samples at equilibrium. Long-ranged electrostatic interactions were calculated at every step with the Particle-Mesh Ewald⁷⁵ (PME) method with a cut-off of 1 nm. A cut-off of 1 nm was also applied to Lennard-Jones⁷⁴ interactions.

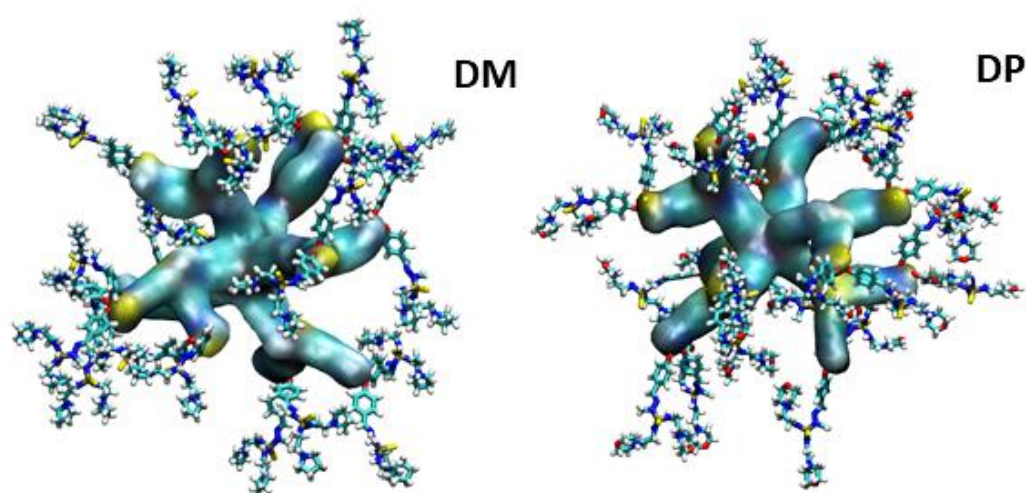


Figure 13: Snapshot of Morpholinium Dendrimer (DM) on left side, and Pyrrolidinium Dendrimer (DP) on the right, during standard molecular dynamics (MD) simulation.

Subsequently, to refine the identification of bonded parameters distributions, a simulated annealing protocol⁸⁵ (SA) was performed. This protocol of enhanced sampling is characterized by the linear union of a series of times referred to specific temperatures, which forms a series of SA cycles. We implement two different SA protocols using before mentioned parameters in NVT ensemble as follow in Table 2:

Table 2: Description of the two Simulated Annealing (SA) cycles adopted to improve the exploration of bonded parameters distributions. The only difference is in the peak of temperature respectively, 600K for cycle-1 and 800K for cycle-2.

Cycle 1	Cycle 2
at 0 ns correspond 300K	at 0 ns correspond 300K
at 10 ps correspond 600K	at 10 ps correspond 800K
at 10 ns correspond 300K	at 10 ns correspond 300K
at 20 ns correspond 300K	at 20 ns correspond 300K

One SA cycle (Figure 14) consists of heating the system from a temperature of 300 K to a temperature of 600 K or 800 K depending on the cycle, in 20 ps. Subsequently the system is cooled by the temperature of 600 K or 800 K at the temperature of 300 K, in 10 ns. Finally, the system is maintained at a temperature of 300 K for 10 ns. 10 cycles were performed for a total of 200 ns of MD simulation. Each one of the just described cycles has been repeated for 10 times, generating a series of complete SA cycles¹¹⁰.

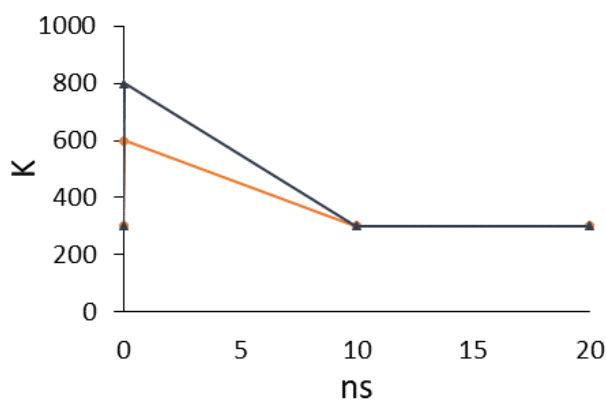


Figure 14: Representation of the two simulated annealing (SA) cycles. The protocol starts at time 0 ns with $T=0K$, proceeds with heating at $T = 600K$ or $T = 800K$ in 20 ps, continues with cooling at $T = 300K$ in 10 ns and finally remains for 10 ns at $T = 300K$.

Concatenating the last 50 ns of the classical MD with the last 5 ns of the last 5 cycles of the SA MD an ensemble trajectory of 100 ns was built, on which the topological parameters of the CG model was calculated.

4.2.2. CG System setup

The Coarse Grained (CG) molecule maps have been developed following the CG Martini⁸⁸ strategy, which implies to group atomistic particles in CG beads each composed by 2-3 or 4-5 heavy atoms. These maps have been designed to allow conformational changes and rotations (*Figure 15*) of specific atoms zones in dendrimers CG models, seen in molecular dynamics (MD) atomistic simulations:

- Flipping between methyl and thiophosphoric groups, around the nitrogen atoms, which allows translation of the next connected branches.
- Torsion of the bond between nitrogen and phosphorus atoms which allows rotations of the next connected branches.

These two characteristics, in addition to controlling movements of branches that starts from cyclophosphazene ring, are crucial to mimic the dendrimers mobility showed in atomistic MD to the CG models.

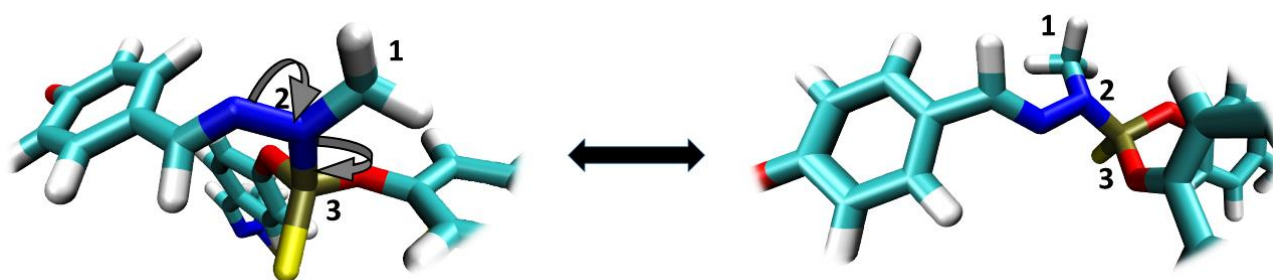


Figure 15: Representation of flipping between methyl (1) and thiophosphoric (3) group, around the nitrogen (2) atom, and torsion of the bond between nitrogen (2) and phosphorus atom (3).

PyCGTOOL¹¹¹ was used to generate CG bond terms of each separate residues (bond, angle). To achieve this result was used as input for PyCGTOOL, the previously mentioned atomistic ensemble trajectory file. Then starting topology files was created using the *martini_v2.2* force-field⁸⁸ by

homemade scripts. Iterative modified Boltzmann inversion technique (3.5.2. Modified Boltzmann inversion), which is similar to the iterative Boltzmann inversion method^{89,90} was used to derive potentials of the bonded terms in order to match the properties of reference atomistic models. Both dendrimers, pyrrolidinium (DP) and morpholinium (DM) type, were positioned in center of a dodecahedron box filled with normal water beads, using 0.21 nm as van der Waals distance, and ions (NA⁺ and CL⁻) at a physiological concentration (0.15 M). To prevent unwanted CG water freezing, 20% of normal P4 water beads were replaced with special type BP4 antifreeze water beads⁸⁸. The maps^{92,100,112–114} adopted to generate CG models are shown below:

Pyrrolidinium Dendrimer type 1.

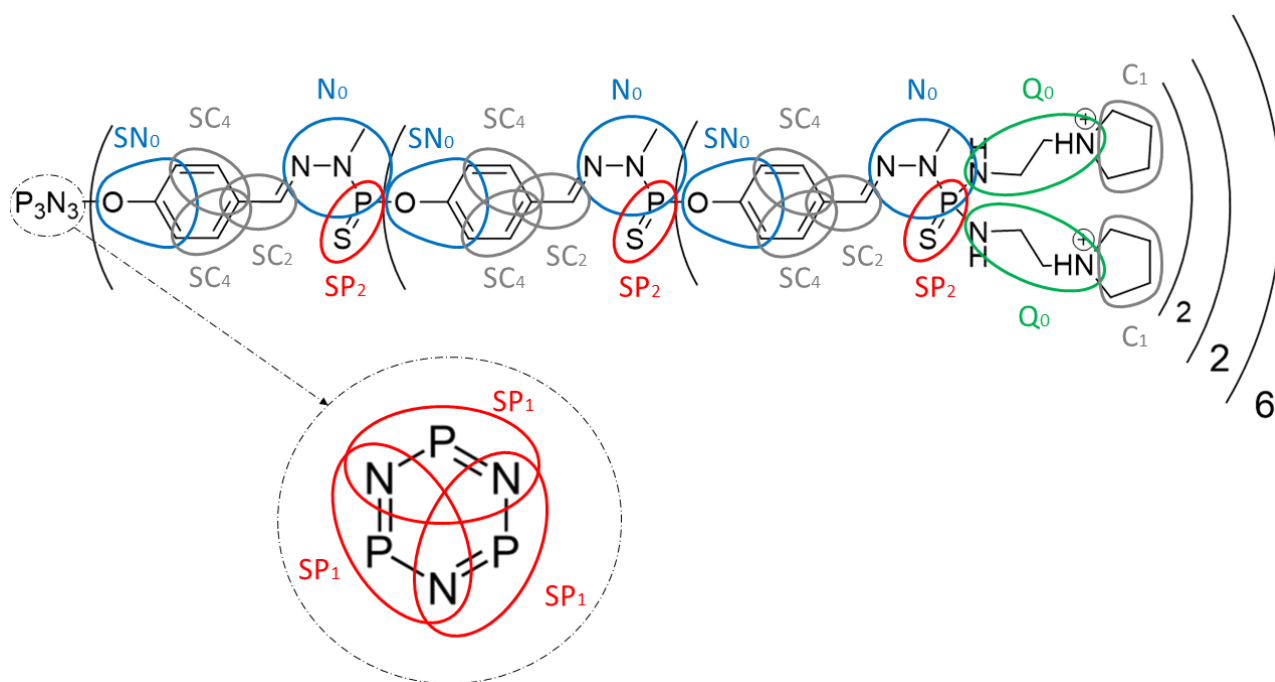


Figure 16: Pyrrolidinium dendrimer heavy atoms mapped in CG beads. Beads are subdivided by color: non polar (BLUE), apolar (GREY), polar (RED) and charged (GREEN).

Indication of CG particles employed to define CG beads are shown in *Table 3*, where Beads, Smiles code of the mapped atomistic groups and Particle type is reported. Mapping employed only existent CG particles⁸⁸.

Table 3: Description of the pyrrolidinium dendrimer CG Mapping. Beads, Smiles code of the mapped atomistic groups and particle type are reported.

Bead	Smiles (Atomistic Structure)	Type
SP ₁	NP=N	POLAR
SN ₀	OC(=C)C	NON POLAR
SC ₄	C =CC	APOLAR
SC ₂	CC	APOLAR
N ₀	N(C)NP	NON POLAR
SP ₂	P=S	POLAR
Q ₀	NCC[N+]	CHARGED (+1)
C ₁	CCCC	APOLAR

More in detail:

- ✓ SP₁ bead has been chosen to describe the atomic group [NP=N]; the presence of the phosphorous and the nitrogen atoms may justify the choice of slightly polar bead. Low polar bead has been chosen also for avoid too high affinity with the water beads, which could give anomalous movements to the central ring.
- ✓ SN₀ bead (4 CG particles [OC(=C)C]) maps oxygen atom and orto benzene atoms. The chosen SN₀ particles are smaller than regular N₀ beads⁸⁸. All particles are connected by constraints to preserve rigidity of the structure and avoid fast oscillation of the ring.
- ✓ SC₄ bead (3 CG particles [C=CC]) maps meta and para benzene atoms^{88,113}. All particles are connected by constraints to preserve rigidity of the structure and avoid fast oscillation of the ring.
- ✓ SC₂ bead represents the atomic group [(C=N)NC]. The group is considered non-polar. Reasons lies in double bonds made by nitrogen atoms. Those double bonds make the establishment of hydrogen bonds unlikely. Moreover, the non-polar characteristics is also justified by the shield effect of the methyl group.
- ✓ N₀ bead maps the atomic group [N(C)NP]. The group is considered non-polar. Reasons lies in double bonds made by nitrogen atoms. Those double bonds make the establishment of hydrogen bonds unlikely. Moreover, the non-polar characteristics is also justified by the shield

Table 4: Description of the morpholinium dendrimer CG Mapping. Beads, Smiles code of the mapped atomistic groups and Particle type are reported.

Bead	Smiles (Atomistic Structure)	Type
SP ₁	NP=N	POLAR
SN ₀	OC(=C)C	NON POLAR
SC ₄	C=CC	APOLAR
SC ₂	CC	APOLAR
N ₀	N(C)NP	NON POLAR
SP ₂	P=S	POLAR
Q ₀	NCC[N+]	CHARGED (+1)
N ₀	CCOCC	APOLAR

More in detail:

- ✓ SP₁ bead has been chosen to describe the atomic group [NP=N]; the presence of the phosphorous and the nitrogen atoms may justify the choice of slightly polar bead. Low polar bead has been chosen also for avoid too high affinity with the water beads, which could give anomalous movements to the central ring.
- ✓ SN₀ bead (4 CG particles [OC(=C)C]) maps oxygen atom and orto benzene atoms. The chosen SN₀ particles are smaller than regular N₀ beads⁸⁸. All particles are connected by constraints to preserve rigidity of the structure and avoid fast oscillation of the ring.
- ✓ SC₄ bead (3 CG particles [C=CC]) maps meta and para benzene atoms^{88,113}. All particles are connected by constraints to preserve rigidity of the structure and avoid fast oscillation of the ring.
- ✓ SC₂ bead represents the atomic group [(C=N)NC]. The group is considered non-polar. Reasons lies in double bonds made by nitrogen atoms. Those double bonds make the establishment of hydrogen bonds unlikely. Moreover, the non-polar characteristics is also justified by the shield effect of the methyl group.
- ✓ N₀ bead maps the atomic group [N(C)NP]. The group is considered non-polar. Reasons lies in double bonds made by nitrogen atoms. Those double bonds make the establishment of hydrogen bonds unlikely. Moreover, the non-polar characteristics is also justified by the shield effect of the methyl group. Phosphorous atoms are used only for center the bead around the planar chiral nitrogen.

- ✓ SP_2 bead maps the atomic group [P=S] as previously done in literature⁸⁸.
- ✓ Q_0 bead maps the atomic group [NCC[N+]]. The CG particle is positively charged (+1). The choice is in agreement with the coordinated covalent bond between nitrogen and hydrogen. Similar chemical groups have been mapped with Q_0 in DPPC phospholipids in literature⁸⁸.
- ✓ N_0 bead maps the atomic group [CCOCC]. Five atoms single bead was chosen to maintain the symmetry of the cyclic structure in comparison to the pyrrolidinium terminal, just increasing polarity to N type bead for the presence of oxygen atom.

An example of the application of the resulting CG map overlapped on the atomistic structure of the morpholinium dendrimer is shown in *Figure 18*:

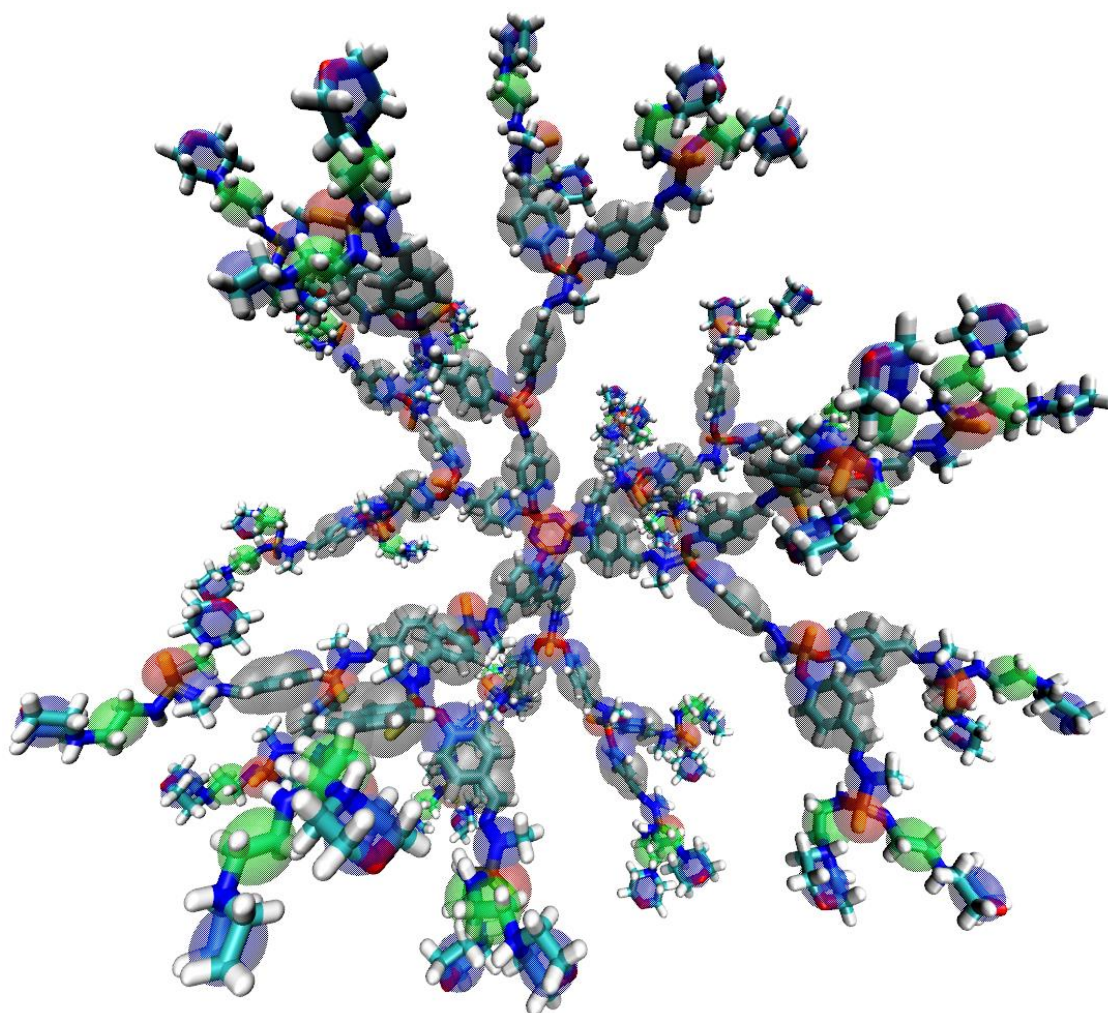


Figure 18: tridimensional view CG beads after application of DM dendrimer map on reference atomistic structure. In red are show bead P type, in grey are show bead C type, in blue are show bead N type and in green are show bead Q.

4.2.3. Molecular dynamics

For both dendrimers the following procedure was followed. Each system was energy minimized by 1000 steps of steepest descent energy minimization algorithm. A 500 ps position restrained MD was performed at 320 K using v-rescale⁸⁰ thermostat in NVT ensemble. Then was performed a 5 ns position restrained MD at 320 K and 1 atm using Berendsen⁷⁹ barostat in NPT ensemble. Atom velocities were randomly initialized following a Maxwell-Boltzmann distribution. GROMACS 5 package was used for all MD simulations and data analysis^{108,109}. Long ranged electrostatic interactions were calculated at every step with the reaction-field method¹¹⁵, using relative dielectric constant value of 15, with a cut-off of 1.1 nm⁹⁷. A cut-off of 1.1 nm was also applied to Lennard-Jones interactions⁹⁷. The LINCS algorithm⁷⁸ approach allowed an integration time step of 10 fs. The Visual Molecular Dynamics (VMD)¹¹⁶ package was used for qualitative inspection of the simulated systems. Finally was done 500 ns MD without position restrains, in the NPT ensemble using Parrinello-Rahman barostat⁸³ to validate CG models. An examples of DM dendrimer before production dynamics is shown in Figure 19. Validation analysis was performed taking into account the last 100 ns of production run MD.

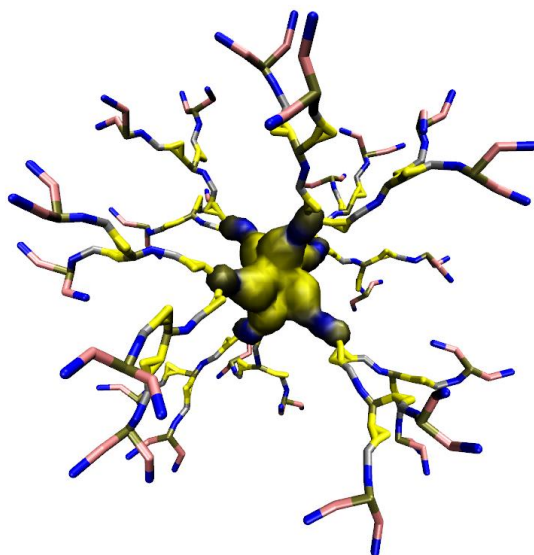


Figure 19: Coarse grained (CG) model of DM dendrimer used as starting model for production dynamics.

4.3. Results and discussion

An important procedure when CG models are created, is the validation of their accuracy in reproducing the topological and conformational characteristics evinced in atomistic simulations. As pointed out previously, validation of dendrimer CG models has followed two main pathways: firstly, topological bonded parameters has been tuned up with the goal to achieve convergence on all the bond terms distribution^{111,117,118}, paving the way to an interpretation of the atomistic topological information. Once satisfactory correlation has been proven, the second part of validation process starts by checking conformational characteristics, analyzing radius of gyration (RG) and root mean square fluctuation (RMSF), as described in literature^{111,117,118}. Accordingly to our validation strategy, CG DP and DM models bonds, angles and dihedrals terms, has been analyzed. Ratio of mean and standard deviations (SDEV) between atomistic and CG bonds term distributions $\left(\frac{mean_{ATOMISITC}}{mean_{COARSE-GRAINED}}; \frac{sdev_{ATOMISITC}}{sdev_{COARSE-GRAINED}}\right)$ over the time are shown in *Figure 20*. Value in the range from 0.7 to 1.3 are considered acceptable.

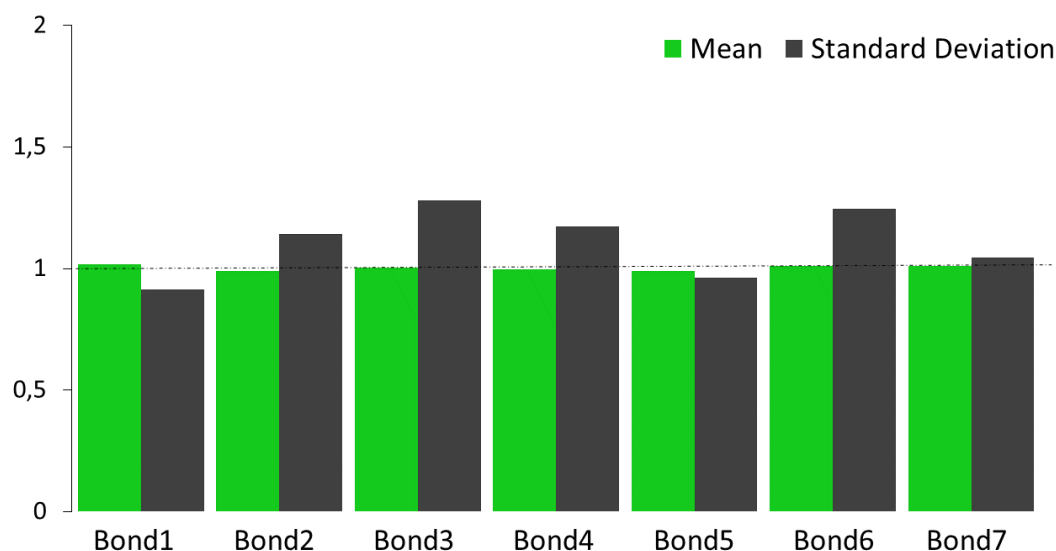


Figure 20: Bar diagram which evidence the comparison of bond parameters, in light-green is show mean of each bond ratio, in dark green is show standard deviation of each bonds ratio. Ratio between value 0.7 and 1.3 are considered satisfactory for validation. Ratio are computed making the quotient between the atomistic mean or standard deviation and CG mean or standard deviation.

Notably, *Figure 20* shows a perfect matching values for means of each bonds, while SDEV tends to be greater than 1.0, because CG Martini⁸⁸ models need higher potential energy to maintain the same mean in comparison with atomistic mean. This behavior leads into generation of slightly stiffer CG model. Therefore, some bonds have not been taken into consideration because they were set as constraints. These bonds were assumed as constraints when the force constant (K_b) were greater than 10^6 (KJ mol⁻¹ nm⁻²). Indication of each number of bonds illustrated in *Figure 20* is show in *Table 5*, where bonds number and bonds type are reported.

Table 5: Description of the bond parameters with bond number and bond bead type.

Bond number	Bond type
Bond 1	SP ₂ - Q ₀
Bond 2	Q ₀ - N ₀
Bond 3	SP ₂ - SN ₀
Bond 4	SC ₂ - N ₀
Bond 5	N ₀ - SP ₂
Bond 6	SP ₁ - SN ₀
Bond 7	Q ₀ - C ₁

Next topological terms tuned up are the angles parameters following the same procedure adopted before. Then, ratio of the averages and SDEV between atomistic and CG angles distributions $\left(\frac{mean_{ATOMISITC}}{mean_{COARSE-GRAINED}}; \frac{sdev_{ATOMISITC}}{sdev_{COARSE-GRAINED}} \right)$ over the time are shown in *Figure 21*. Even in this case, value in the range from 0.7 to 1.3 are considered acceptable. Also in angle terms matching analysis, we can clearly observe that keeping the average in the desired range is easier than keeping the SDEV in the right zone. Remarkably, as we can see in both *Figure 20* and *Figure 21* the values of SDEV has the tendency to be higher than 1.0, which means that the SDEV of the atomistic bonded parameters is higher than that of the CG bonded parameters. This is in agreement with the general characteristics of the Martini force field^{88,100} which has a greater rigidity on the model's bonded parameters in comparison to atomistic models, due to the reduction of the degrees of freedom. Indication of each number of angles considered is show in *Table 6*, where bonds number and bonds type are reported.

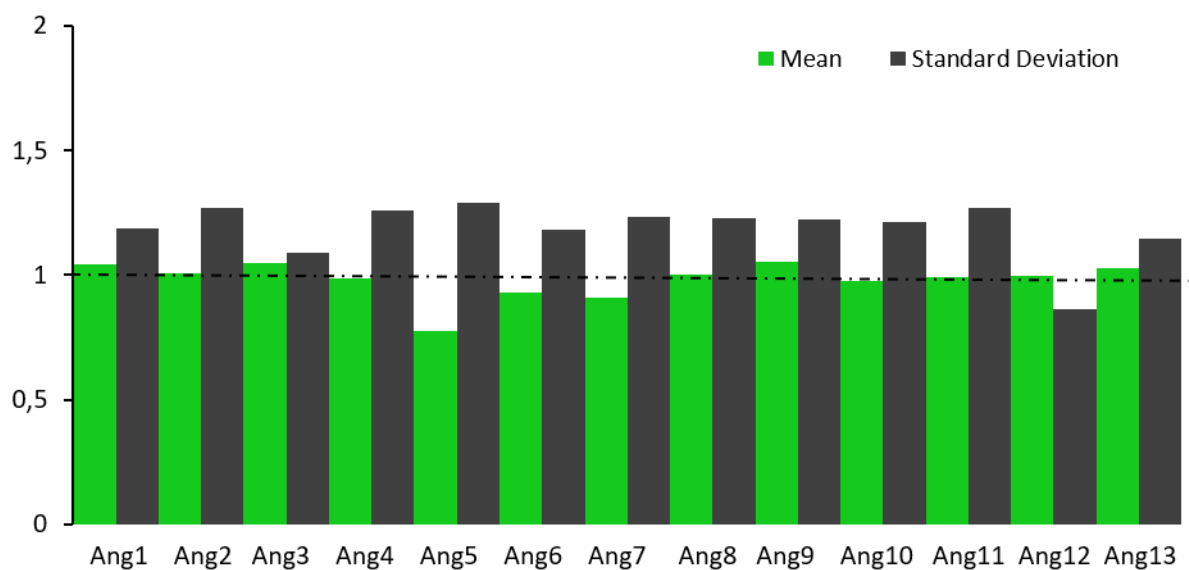


Figure 21: Bar diagram which evidence the comparison of angle parameters, in light-green is show mean of each angle ratio, in dark green is show standard deviation of each angles ratio. Ratio between value 0.7 and 1.3 are considered satisfactory for validation. Ratio are computed making the quotient between the atomistic mean or standard deviation and CG mean or standard deviation.

Table 6: Description of the angle parameters with bond number and angle type.

Angle number	Angle type
Ang 1	Q ₀ - SP ₂ - Q ₀
Ang 2	SC ₂ - N ₀ - SP ₂
Ang 3	SP ₂ - Q ₀ - N ₀
Ang 4	SN ₀ - SP ₂ - SN ₀
Ang 5	N ₀ - SP ₂ - SN ₀
Ang 6	N ₀ - SP ₂ - Q ₀
Ang 7	SC ₄ - SC ₂ - N ₀
Ang 8	SP ₂ - SN ₀ - SC ₄
Ang 9	SN ₀ - SP ₁ - SN ₀
Ang 10	SP ₁ - SP ₁ - SN ₀
Ang 11	SP ₁ - SN ₀ - SC ₄
Ang 12	SN ₀ - SC ₄ - SC ₂
Ang 13	SP ₂ - Q ₀ - C ₁

Since mean and SDEV were used to validate bond and angle parameters assuming that the distributions are Gaussian, some examples of distribution are shown in *Figure 22*. The extreme attention in the choice of the GC maps was done to have Gaussian-like distributions that can be easily reproduced with the Martini⁸⁸ system. In addition, it must be remembered that the iterative process of tuning the bonds and angles was done assuming that the distributions are Gaussian-like.

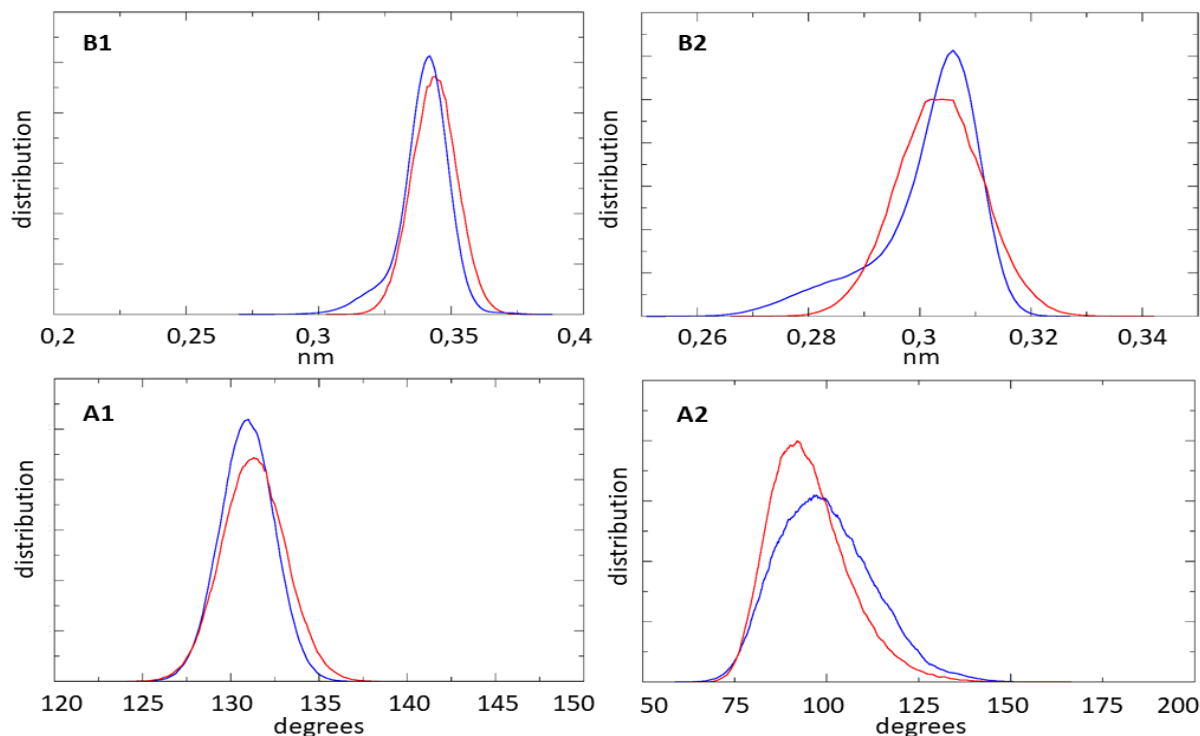


Figure 22: Example of distributions of 4 bonded parameters: **B1** and **B2** are distributions of two bonds terms, instead **A1** and **A2** are distributions of two angles terms. In blue is shown atomistic distribution, in red is shown CG distribution.

Furthermore, to keep the vibrations of the chains in comparison to the central core such as in the atomistic model range, 3 Ryckaert-Bellemans potential¹¹⁹ has been introduced at the dihedral angles between the core and the 6 chains (Figure 23). The beads involved into before mentioned dihedral potential are shown in the Table 7:

Table 7: Description of the dihedral parameters with dihedral number and dihedral type.

Dihedral angle	Dihedral type
Dih 1	SN ₀ - SP ₁ - SP ₁ - SN ₀

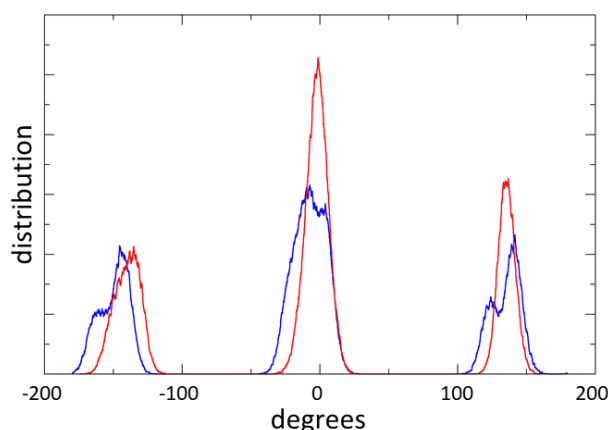


Figure 23: Ryckaert-Bellemans dihedral potential applied between core and the 6 chains. In **blue** is represented atomistic distribution in **red** is shown CG distribution. It is observable that imposed CG dihedral well emulate the reference atomistic dihedral.

Controlling the core-branches dihedral potential also strongly influence the whole 3D conformation of the dendrimer, avoiding for examples, uncontrolled collapsing of the branches. Use of dihedral potentials is the key to develop even more correct CG models, but their employment affects the simulation stability, forcing the adoption of a smaller time-step. Hence, modulation of bonded terms was done, we continue the validation exploring the conformational characteristics. Structural conformation of both CG models was evaluated comparing mean and standard deviation of the RGs. Figure 24 shows a bar diagram where averages of the CG models RGs are very close to the reference atomistic RGs, and also the SDEV seems to have same behavior.

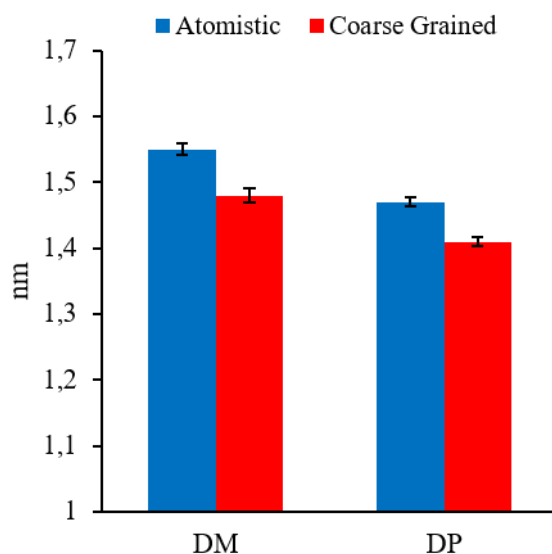


Figure 24: Radius of gyration of morpholinium dendrimer (**DM**) and pyrrolidinium dendrimer (**DP**): comparison between atomistic model (blue) and coarse grained model (red).

Controlling the RGs SDEV is crucial to preserve, because it might modulate the “flexible” or “rigid” binding behavior¹²⁰ and therefore afflict the complexing capability⁶⁶. Finally, RMSF was evaluated for each dendrimer subdividing the structure *per* residue. Fluctuation of the chain terminals is very important for the binding capacity of the dendrimers. If CG terminals (FFF - EEE) results too much stiff in confrontation with atomistic one, probably they will be no more able to properly bind target molecule. Furthermore, even the management of other residues (BBB-CCC-DDD) has an important role in coupling mechanism, since the allow reorganization of dendrimer structure when aggregation occur²⁷. In Figure 25 is shown the mean and SDEV of RMSF divided by residues, as stated before, of the atomistic dendrimers chain structure (blue), which are also quite good maintained in CG models (red). The core residue (AAA) wasn't analyzed because is composed by an aromatic ring of phosphorene which in CG is parametrized with 3 SP₁ bead linked each one with constraints, that no permit fluctuations.

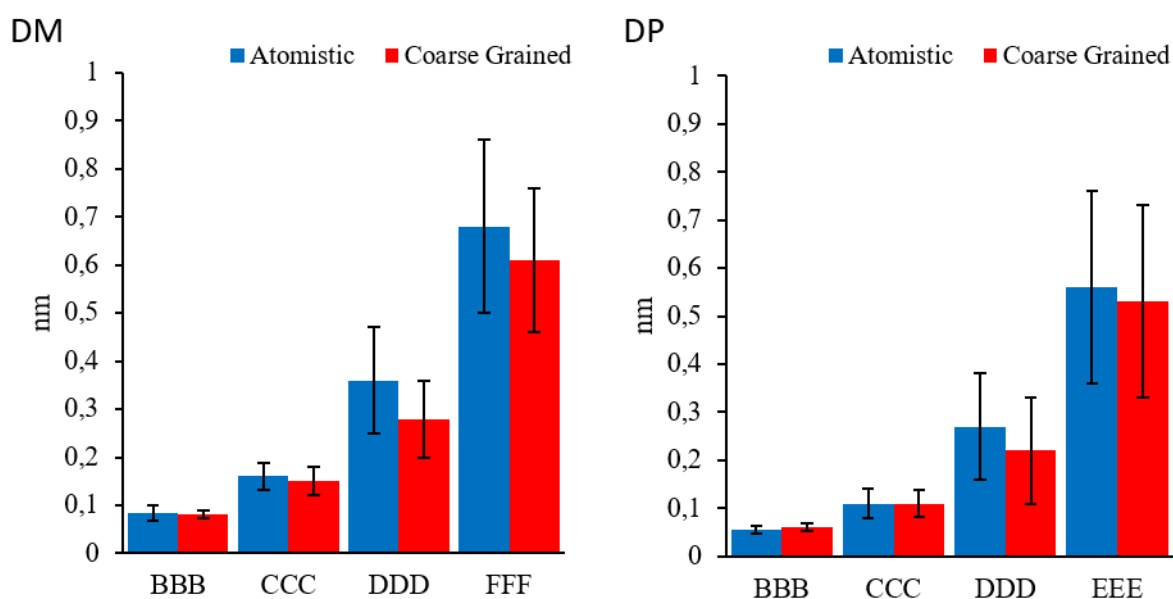


Figure 25: Root mean square fluctuation (RMSF) of morpholinium dendrimer (DM) and pyrrolidinium dendrimer (DP) calculated and divided by residues, represented through mean with standard deviation. In blue are shown atomistic RMSF, in red CG RMSF.

Overall conformational analysis evidence that CG models reflect quite well the atomistic models characteristics. Noteworthy, SDEV of RGs and RMSF CG analysis appear to be particularly close to atomistic reference, which plays a key role in modulating dendrimer binding attitude^{66,101,120}. In the next section we are going to investigate the self-assembly behavior by DM-DM and DP-DP dendrimer, intrinsically gathering further evidence of the well-parametrized CG dendrimer models.

4.4. Dendrimers self-assembly proprieties

4.4.1. Introduction

Elucidating characteristic of dendrimers self-assembly mechanism is crucial for the development of biocompatible, not dangerous drug delivery system. More generally, uncontrolled aggregation of synthetic (such as dendrimers) or biological (such as proteins) substrates, may lead in severe health complication, like cardio-vascular problems¹²¹, cytotoxicity¹²² or chronic/degenerative disorders. For this reasons, in this master thesis work self-assembly behavior of both Pyrrolidinium (DP) and Morpholinium (DM) dendrimers was investigated to shed light upon the driving mechanisms of such phenomenon. Nowadays, *in vitro* evaluation of complexation attitude is explored by a refined technique called isothermal titration calorimetry^{123–125} (ITC). ITC is able to measure binding free energy (ΔG), dissociation constant (k_D), enthalpy (ΔH), stoichiometry (N) and entropy (ΔS). In recent literature, a plenty of research works used ITC method to investigate aggregate or receptor-ligand binding proprieties^{103,126–128}. Therefore, in a previously study present in literature was discovered analyzing ITC binding curves (Figure S 1, picture on top-left), that DP dendrimers have increased capability to aggregate and make solid precipitation from solution²⁷. Instead, still analyzing ITC binding curves, DM dendrimers didn't showed the same kind of behavior²⁷ (Figure S 1 picture on top-right). Understanding with the aim to modulate this susceptible peculiarity will give knowledge to get over this problem and optimize even better novel class phosphorous dendrimer. For this purpose, 2 CG systems composed by homologous dendrimers has been set up to study the self-assembly pattern.

4.4.2. Materials and methods

DP-DP and DM-DM dendrimers systems was generated using dodecahedron box and positioning dendrimers at 3 nm minimum distance from each other, as represented in Figure 26. Topology files was created using *martini v_2.2* force-field⁸⁸ with previously validated parameters. Subsequently, systems was solvated with non-polarizable water beads and was added Na-Cl ions at concentration of 0,15M. Normal water beads have been replaced at 20% with heavy water bead (BP4)⁸⁸ to prevent systems water freezing. Each system was energy minimized by 2000 steps of steepest descent energy

minimization algorithm. A 1 ns position restrained molecular dynamics (MD) was performed at 320 K using v-rescale⁸⁰ thermostat in NVT ensemble. Then was performed a 5ns position restrained MD at 320 K and 1 atm using Berendsen⁷⁹ barostat in NPT ensemble. Atom velocities were randomly initialized following a Maxwell-Boltzmann distribution. GROMACS 5 package was used for all MD simulations and data analysis^{108,109}. Long ranged electrostatic interactions were elaborated with the reaction-field method¹¹⁵, using relative dielectric constant value of 15, with a cut-off of 1.1 nm⁹⁷. A cut-off of 1.1 nm was also applied to Lennard-Jones interactions⁹⁷. The LINCS algorithm⁷⁸ approach allowed an integration time step of 10 fs. The Visual Molecular Dynamics (VMD)¹¹⁶ package was used for the visual inspection of the simulated systems. Finally was done 10 MD replicas of 500ns for each dendrimer type, without position restrains, in the NPT ensemble using Parrinello-Rahman barostat⁸³ to evaluate the aggregation proprieties.

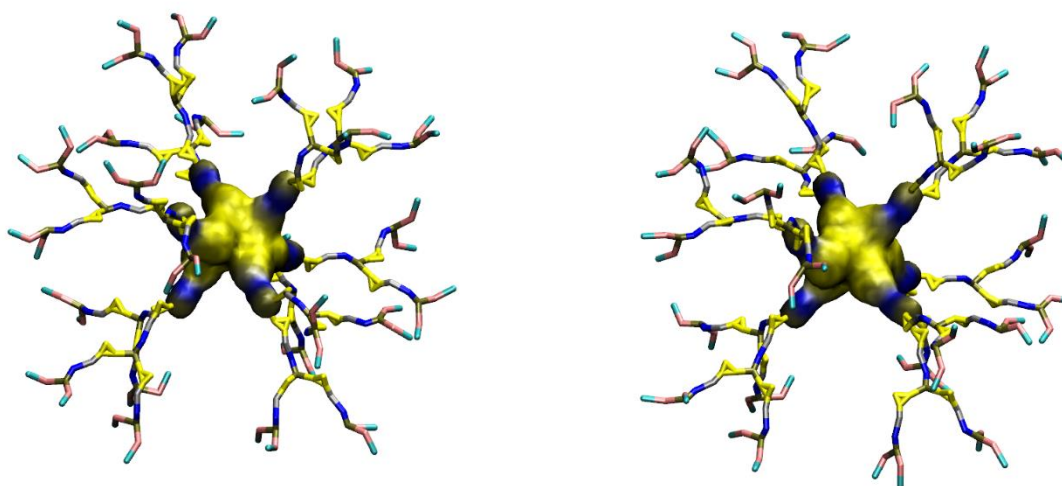


Figure 26: Representation of two dendrimers system generated to evaluate the self-aggregation behavior. In this picture are shown as example, DP dendrimer positioned at minimum distance of 3 nm from each other.

4.4.3. Results and discussion

The choice to perform 10 MD replicas has significantly increased the statistical ensemble for the data extraction. Furthermore, the three-dimensional compartment of CG models is similar but not equal if compared with atomistic one, which can even result in decreased accuracy of simulation. To avoid this problem a greater number of replicas is necessary to identify the trend and try to evince the supramolecular assembly. As shown in the experimental study from the ITC data (Figure S 1, picture

on top-left), DP dendrimers has a tendency to aggregate in bulk structures higher than DM dendrimers (Figure S 1, picture on top-right). In Figure 27 is exhibited the count of how many times aggregation between the two dendrimers has been observed and viceversa, how many times aggregation between the two dendrimers has not been occurred. It's clear that the tendency of the DP dendrimer to aggregate, with 7 times on 10 replicas, is decidedly greater than the DM one, with 3 time on 10 replicas. In other words, Figure 27 indicates that in 70% of DP dendrimers replicas aggregation occurs, while in DM dendrimers replicas self-assembly results only in 30% of cases.

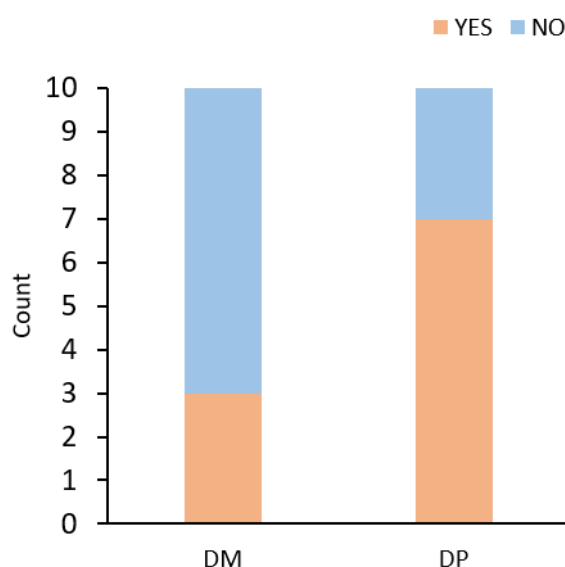


Figure 27: Stacked column graphic which shown the count of replicas where self-assembly was observed, and the count of replicas where wasn't observed. The left bar represent DM dendrimer (3-yes and 7-no), contrariwise the right bar represent DP dendrimers (7-yes and 3-no).

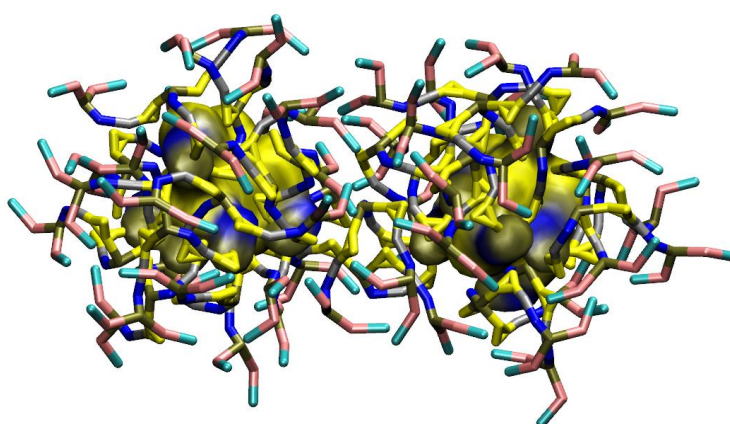


Figure 28: Snapshot of molecular trajectory were is highlighted self-assembly of two DP dendrimers.

Deeping inside the aggregation potential of DP dendrimer (Figure 28), for replicas where was checked self-assembly, distance analysis of the respective center of mass (COM) was performed. Figure 29 shows the average distance (AD) between two dendrimers COM, considering them bounded for values under 3.2 nm, which is slightly higher than two time RG of DM dendrimer. The choice of this threshold value is because we assume that interaction occurs when measured distance value is two times the RG. Since dendrimer shape is near-spherical, assumption that RG is approximation of the dendrimer radius might be acceptable. The Figure 29 reveals that distance between DP dendrimers (2.83 nm) is moderately lower than DM dendrimers (3.13 nm), indicating a greater capacity to bulk into more tight aggregate, which may lead in a more stable cluster.

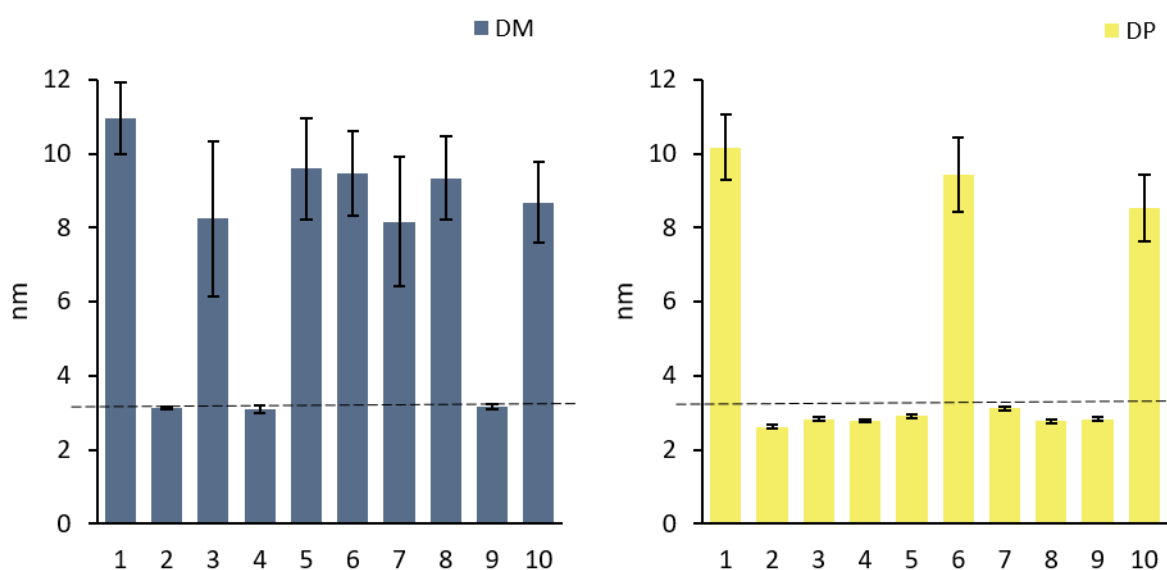


Figure 29: Average distance (AD) representation between center of mass (COM) of the two dendrimers. On left is shown DM dendrimers AD, on the right is shown DP dendrimers AD. The dotted line represent the value of 3.2nm that is considered as threshold under below which aggregation occur. This value has been chosen because is almost 2 times RG of dendrimers, with the assumption that, since dendrimer are near-spherical, RG the approximation of RG with the radius of the dendrimer may be acceptable.

Furthermore, to strengthen the previous analysis, solvent accessible surface area (SASA) and buried surface (BS) estimation was carry out to confirm the data of the AD analysis. Figure 30-A shed light on the higher total BS demonstrated by DP dendrimers, which, in addition, illustrate that the hydrophilic area remain quite similar for both dendrimers type, contrariwise the hydrophobic area is higher in the case of DP dendrimers. The huge difference in dendrimer structural chemistry is only the terminal bead, which for DM molecules is polar than DP one, which is completely apolar. Since systems is immersed in an aqueous solvent, which is composed by polar bead, the behavior of non-polar bead affinity to aggregate is enhanced and probably result in these demonstrated tighter self-

assembly showed by DP dendrimers. In support of BS analysis, was also carried out SASA valuation (Figure 30-B), which underline that solvent accessible area is great for DM dendrimers in comparison with DP dendrimers, highlighting that the difference is again quite almost to appanage of the hydrophobic area.

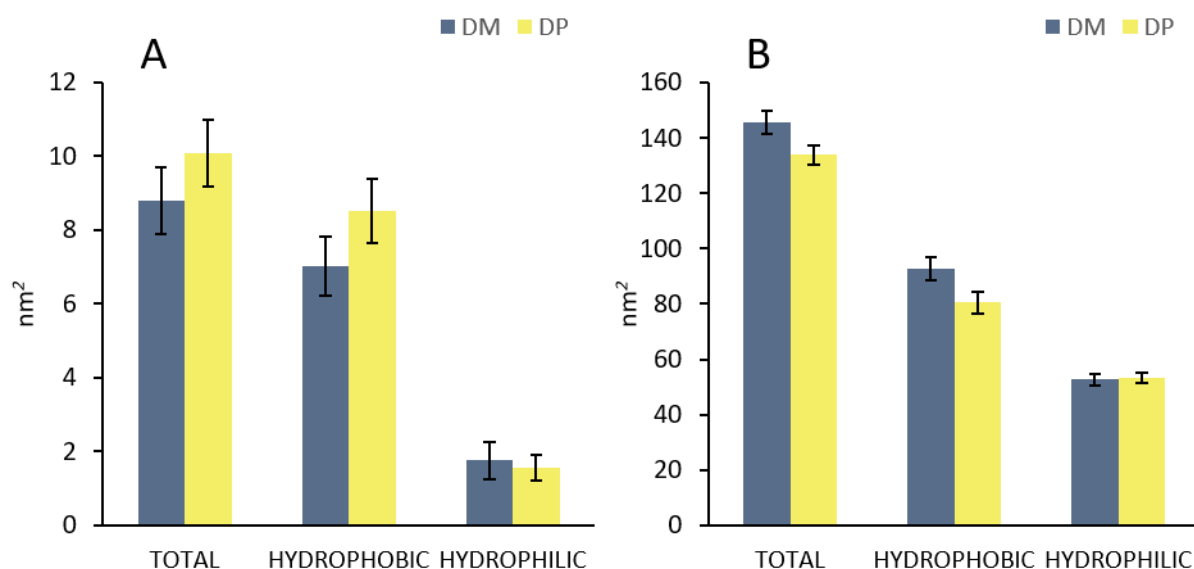


Figure 30: figure 28-A shows buried surface (BS) of DM and DP dendrimers; figure 28-B shows solvent accessible surface area (SASA) of DM and DP dendrimers. In this chart is emphasized the hydrophobic variation between the DP-DP and DM-DM systems, which may be the driver of DP tighter self-assembly.

In conclusion, the DM and DP dendrimers self-assembly mechanism elucidation was mainly in agreement with the ITC experimental data²⁷, which revealed precipitation phenomenon of DP dendrimers, intrinsically further confirming the CG models fidelity to the atomistic one. Notably, binding DP curve showed in Figure S 1 on top-left, decreases linearly till reaching a final plateau. An interesting development for the future could be the study of the size and stability of DP dendrimer aggregates, and if they are biocompatible or cytotoxic for human cells. In our investigation we focused on the comprehension of base mechanism that allow self-aggregation behavior, rather than elucidate supramolecular properties of high number dendrimers.

4.5. Conclusions

The first goal to explore the dendrimer bulk aggregation^{126,129,130} characteristic was the development of a CG model for the atomistic dendrimer structure. Initially, CG models of DM and DP dendrimers were generated using atomistic trajectory, afterwards a number of MD strategies were adopted to replicate the same atomistic behavior. The validation of CG models, as can be evinced from the sequence of analyzes carried out, followed 2 path strategy. The firstly strategy used to design the CG models was to searching for the best matching results of topological parameters in comparison with atomist models, which would ensure a perfect correspondence of the binding parameters. Instead, the second followed strategy was focused around reproduction of the conformational properties as similar as possible compared with atomistic models, which implies similarity of conformational behavior between atomistic and CG models. The validation evidence shows that CG generated models faithfully reproduce the topological characteristics and conformational properties of the atomistic dendrimer. In addition, aggregation proprieties carried out from experimental analysis²⁷ were investigate. Noteworthy, DP dendrimers shows a self-aggregation trend much higher than DM dendrimers, which is in agreement with in vitro performed tests, were ITC curves evidence a precipitate formation by DP dendrimers²⁷. The realist-like trend reproduced performing MD simulations is also intrinsically an additional validation of the models quality. In the next chapter, we will try to shed lights on the different stoichiometric value showed by DM and DP dendrimers.

5. Elucidating interaction mechanism between dendrimers and siRNA

5.1. Stoichiometry of dendrimer-siRNAs binding capability

5.1.1. Introduction

The modern medicine doctrine of specific cellular targeting, conceived to minimize the side effects of drugs, involves the use of smart engineered drug delivery systems⁶⁹. The knowledge of interaction mechanisms between carrier and drug plays a central role for the design of an optimal drug delivery system. Consequently, molecular dynamics (MD) studies were carried out to make clear interaction properties of morpholinium (DM) and pyrrolidinium (DP) dendrimers with novel experimental drugs, like siRNAs. MD simulations have been set up to shed light mainly on dendrimer-siRNA stoichiometry. Evaluating dendrimer-siRNA binding stoichiometry is crucial for understanding which of our two dendrimers (DM and DP) is more suited for siRNA delivery purposes. As mentioned before, ITC experimental curves²⁷ show that DP-siRNA stoichiometry stands at 2.25 ± 0.03 (Table S 1), while DM-siRNA stoichiometry stands at 0.60 ± 0.03 (Table S 1), which definitively crown the DP dendrimer as most efficient nano-carrier. However, the greater capacity in the transport of drugs is in contrast with the tendency to form bulky aggregates that lead to the creation of precipitate, which for example, may cause immune reactions or thrombi. In this section we are going to perform MD simulations with a system formed by one dendrimer and two siRNAs with the aim to assess the binding stoichiometry of both DM and DP dendrimers. The comprehension of interaction behavior with drugs of these slightly different dendrimers can show the way to engineering increasingly optimized carriers for drug delivery.

5.2.2. Materials and methods

Initially siRNA CG model was created using *martinize-nucleotide.py* script¹¹⁷ starting from the structure previously used in Deriu *et al.* paper²⁷. Then siRNA-DP-siRNA (DP-2s) and siRNA-DM-

siRNA (DM-2s) systems was generated positioning dendrimer at the center of the used dodecahedron box, with around 2 nm minimum distance from each siRNAs, as represented in Figure 31. Subsequently, systems were solvated with non-polarizable water beads and was added Na-Cl ions at concentration of 0,15M, such as human extra-cellular ions concentration. *Martini v_2.2*⁸⁸ force-field was adopted for CG simulation. To avoid freezing of the solvent beads, 20% of normal water beads (P4) was replaced with heavy water beads (BP4)⁸⁸. Each created system was energy minimized by 3000 steps of steepest descent energy minimization algorithm. A 1 ns position restrained MD was performed at 320 K using v-rescale⁸⁰ thermostat in NVT ensemble. Then was performed a 10ns position restrained MD at 320 K and 1 atm using Berendsen⁷⁹ barostat in NPT ensemble, giving the time to equilibrate the system density. Atom velocities were randomly initialized following a Maxwell-Boltzmann distribution. GROMACS 5 package was used for all MD simulations and data analysis^{108,109}. Long ranged electrostatic interactions were calculated at every step choosing the reaction-field method¹¹⁵, using relative dielectric constant value of 15, with a cut-off of 1.1 nm⁹⁷. A cut-off of 1.1 nm was also applied to Lennard-Jones interactions⁹⁷. The LINCS constraint algorithm⁷⁸ allowed an integration time step of 10 fs. The Visual Molecular Dynamics (VMD)¹¹⁶ package was used for the visual inspection of the simulated systems and for systems snapshot rendering. Finally, was done 12 replicas each of 500ns, without position restrains, in the NPT ensemble using Parrinello-Rahman barostat⁸³ to shed light on binding stoichiometry behavior. All the performed analysis was done extracting the last 50 ns of each replica.

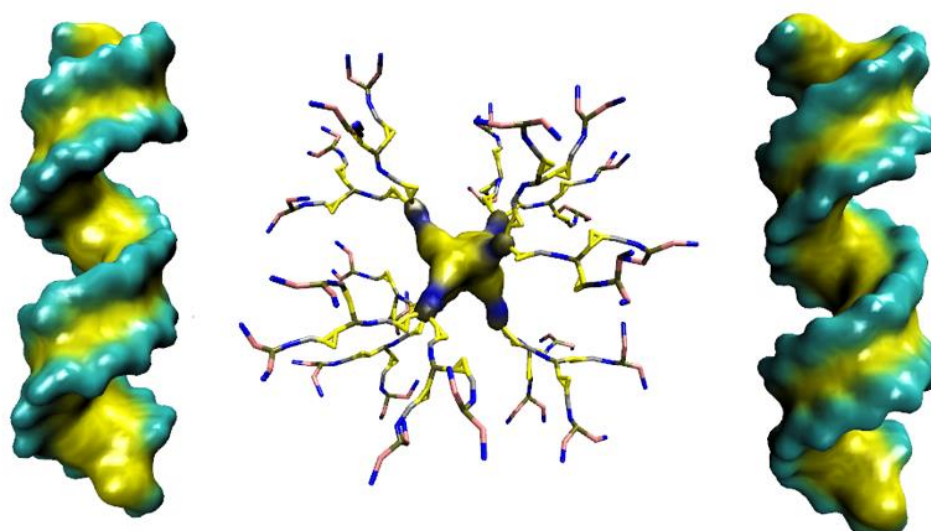


Figure 31: Starting molecular configuration for stoichiometry MD simulations without position restrains. In the picture the siRNAs are positioned with a minimum distance of 2 nm from the dendrimer, to allow interaction more easily but to avoid positioning below Van der Waals and electrostatic radius.

5.2.3. Results and discussion

Dendrimer surface chemistry²⁰ plays an important role in modulating mechanical properties and cargo binding efficiency. For example, slight changes in the terminal groups may lead in significant complexation behavior divergence, which can result in altered biological effect of the dendriplexes^{20,28}. Third generation dendrimers studied in this master thesis work (DM and DP) differ only for 1 bead in the terminal groups, but is sufficient difference to completely change the biological effect and the efficacy of these nanocarriers. Stoichiometry value of DM and DP dendrimer shows a strong discrepancy which still remain unexplained. In this context, MD simulations performed as described in materials and methods section, confirm the experimental data observed in previous work^{20,27}. A first analysis (Figure 32) was carried out by counting the number of occurrences that the two types of dendrimers succeeded in complexing with 1 siRNA or with 2 siRNA. Impressively, DP-2s system is believed to bind 2 siRNAs in 9 replicas out of 12, while the DM-2s system manages to bind 2 siRNAs only in 4 out of 12 replicas. From this first raw data emerges the greater capacity of DP dendrimer to bind 2 siRNAs, which corresponds to 75% of the replicas, whereas for DM dendrimer, 2 siRNAs are complexed only in 33% of cases.

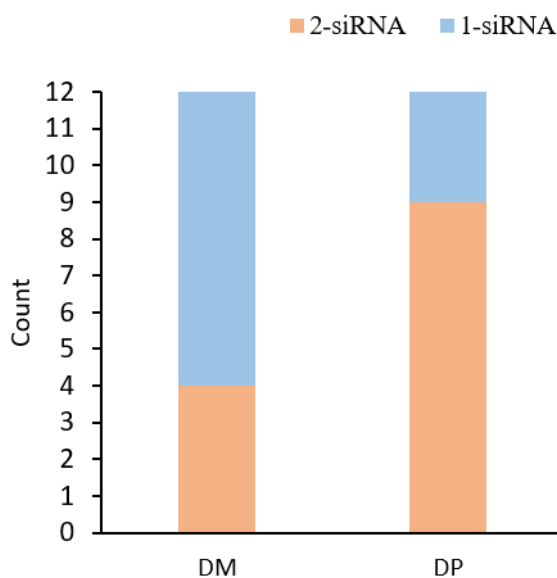


Figure 32: Complexation occurrences bar diagram of DM dendrimer (on the left) and of DP dendrimer (on the right). DP dendrimer can bind 2 siRNAs in 9 replicas out of 12 (75%), instead DM dendrimer may complex with 2 siRNAs in 4 replicas out of 12 (33%).

Figure 33 shows a further qualitative observation of the dendrimer-siRNAs bulk structure, after the complexation, where is appreciable the different binding attitude exhibited by DM and DP dendrimer.

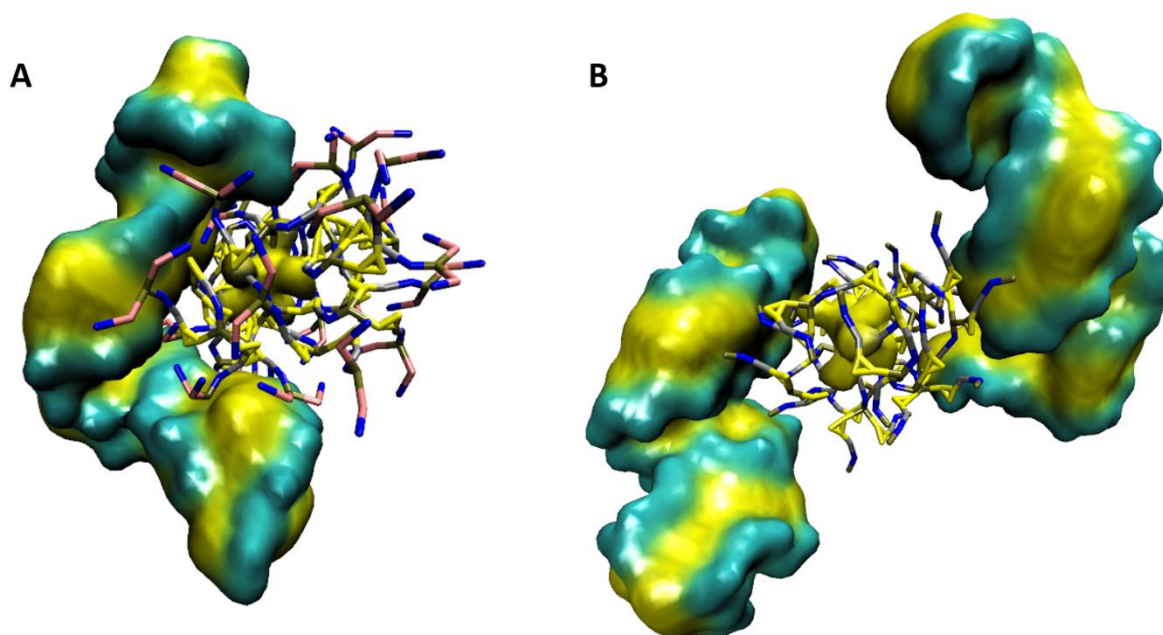


Figure 33: Figure-A shows DM dendrimer in close complexation with 1 siRNA which lead in a stretching of siRNA filament, whilst figure-B shows DP dendrimer which binds 2 siRNAs in blander way than DM dendrimer, leaving the siRNAs structure less flexed.

As recognizable by qualitative illustration of Figure 33, DM dendrimer can interact closer with 1 siRNA, which also suffer a stretching of its structure, while DP dendrimer may complex with 2 siRNAs, which are slight flexed. Initially, investigation of the mechanism of these behavior buried surface analysis was performed for estimate the contact area between the ligand and the receptor. To compute buried surface we considered the 3 replicas of DP-siRNA where 1 dendrimer binds 1 siRNA, and randomly choose 3 replicas of DM-siRNA where 1 dendrimer binds 1 siRNA; then we considered in addition the 4 replicas of DM-siRNA where 1 dendrimer binds 2 siRNA, and randomly choose 4 replicas of DP-siRNA where 1 dendrimer binds 2 siRNA, to get the same statistical ensemble. In average, total interaction surface is remarkably larger in both the analyzed ensemble (DM-1siRNA, DM-2siRNA) for DM-2s systems in comparison with the DP-2s systems ensemble (DP-1siRNA, DP-2siRNA), even if we consider separately the hydrophobic or the hydrophilic components.

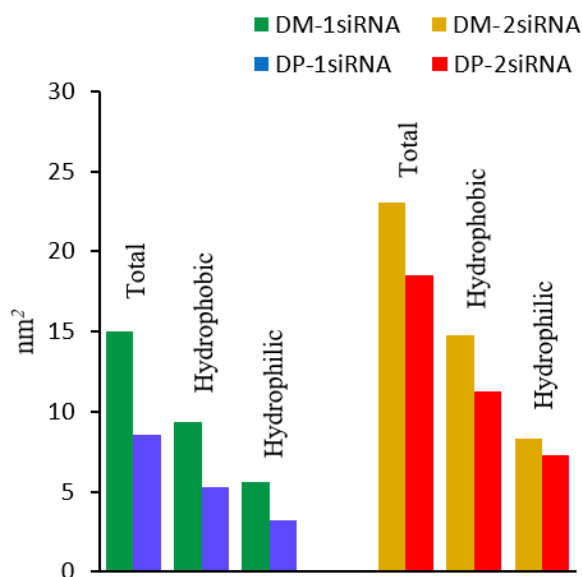


Figure 34: Buried surface analysis computed for DM-1siRNA ensemble (**green**), DM-2siRNA ensemble (**orange**), DP-1siRNA ensemble (**blue**), DP-2siRNA ensemble (**red**). It is observable that in each compared case, DM dendrimer systems have a larger interaction surface in comparison with DP dendrimer systems.

MD simulations highlighted a significant conformational change toward siRNA may happen when complexation with dendrimer occurs, as already detected in earlier literature¹³¹. With the aim to quantitatively measure the before-mentioned siRNA conformational modification, we have adopted the angle parameter φ , which is the angle between two vectors, each connecting the siRNA's center to an extremity (Figure 35, right pictures). siRNA center and the extremity positions were considered as points identified by the center of mass (COM) of 3 selected basis pairs (Figure 35 top). In order to preserve the statistical ensemble, we considered the first 10 DM-siRNA complexes, the first 10 DP-siRNA complexes and 10 free siRNAs, extracting only one attached siRNA if more than one is bound.

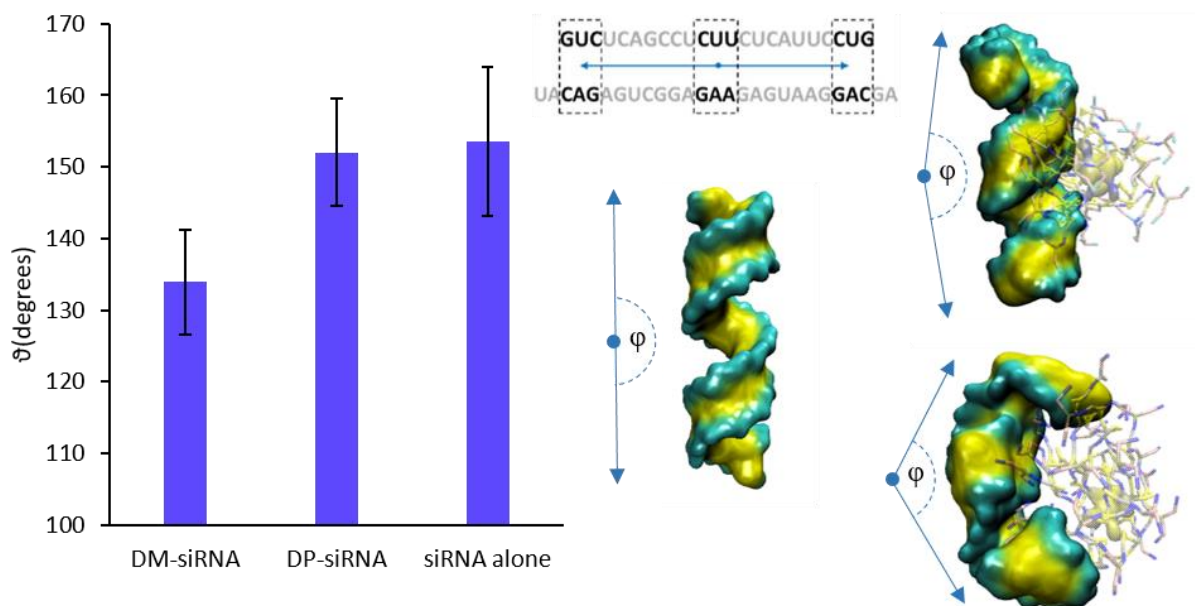


Figure 35: Conformational analysis of siRNA computed using parameter φ , which quantify the flexion strength applied by dendrimer that may lead in stretching momentum. In top side is shown the chosen point for calculating angle φ , estimated as center of mass of selected nucleotides. In the right side of figure is shown how angle φ can change depending on the dendrimer type that binds siRNA, while on left side is shown a bar diagram with mean and standard deviation of the computed angles for DM-siRNA, DP-siRNA and siRNA alone.

Interestingly, DP dendrimer induce only a slight conformational changing in the siRNA structure, stretching the filament from around 154° of free siRNA to 152° (Figure 35 left pictures). Instead, DM dendrimer has the capacity to significant stretch the siRNA's structure, from 154° of free siRNA to 133° (Figure 35 left pictures). Deeping inside the interaction area of siRNA and dendrimer we computed a radial distribution function (RDF) as function of distance dendrimer-siRNA. RDFs was calculated between DM dendrimer beads N_0 and siRNAs groove (Figure 36 right pictures) and between DP dendrimer beads C_1 and siRNAs backbone (Figure 36 right pictures). RDFs analysis was performed using all 12 replicas as statistical set, selecting when necessary, one siRNA rather than two. Notably, DM dendrimer has significant peak around area of 0.47nm if compared with the small peak of DP dendrimer (Figure 36), indicating a remarkable higher affinity for the groove of siRNA. Unfortunately, Martini CG method struggle to estimate value less than 0.47nm because the bead collision diameter σ (Section 3.2.3.) is 0.47 resulting in model limitation.

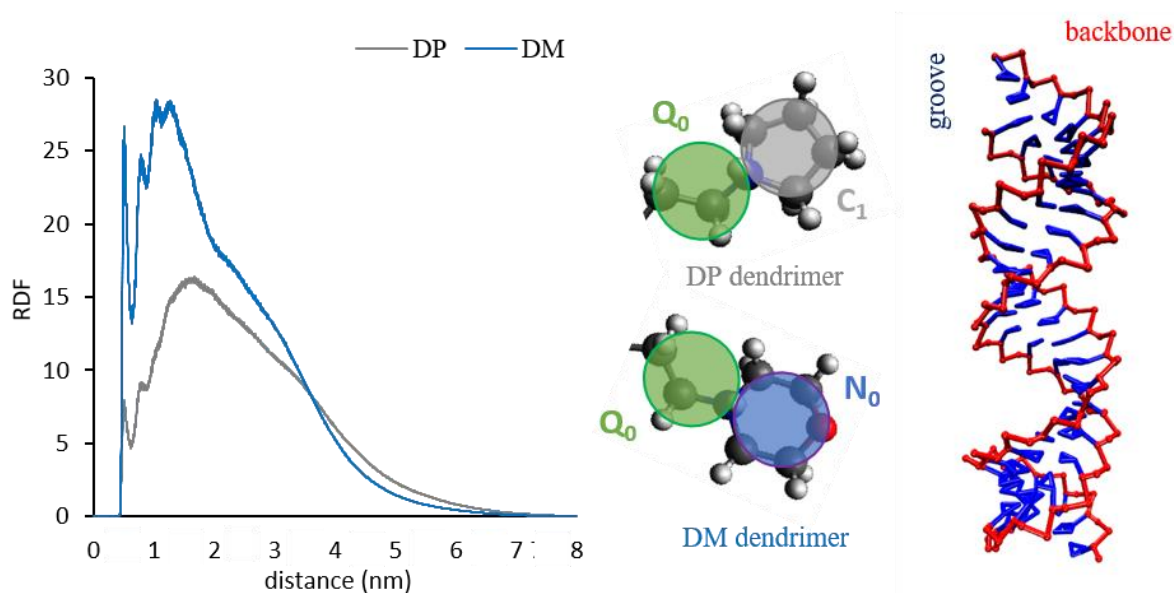


Figure 36: Radial distribution function (RDF) computed as function of dendrimer-siRNA distance. Description of the reference group adopted for RDF calculation is shown on the right side of the picture. On the other hand, on left side is shown RDF chart, which exalts a higher peak around 0.47 nm for the DM dendrimer if compared to the low peak pointed out by the DP dendrimer.

However, DM dendrimer behavior is probably due to the higher affinity of the bead N_0 with the polar bead embedded in the siRNA groove. Contrariwise, DP dendrimer bead C_1 hasn't the same affinity for the siRNA polar bead, exhibiting worse capability to bind the siRNA's groove. To further improve before mentioned evidence, dendrimer terminals-siRNA distance analysis carries out additional information about the interaction attitude of the dendrimer-siRNA complex. As for RDF analysis, statistical set was composed by all 12 replicas, selecting when necessary, only one siRNA rather than two and plotting the data as percentage. Four main different distance ranges were specified in Table 8: "PRIMARY INTERACTIONS ($d \leq 0.6$ nm)" range indicates terminals mostly involved in stabilizing the dendrimer-siRNA complexation; "SECONDARY INTERACTIONS ($0.6\text{nm} < d \leq 1.2\text{nm}$)" range indicates terminals which still contribute to dendrimer-siRNA complexation; "CLOSE TO SIRNA ($1.2\text{nm} < d \leq 2.0\text{nm}$)" range indicates terminals which can be recruited to enhance or stabilize the complex; "FREE TERMINALS ($d > 2.0\text{nm}$)" range indicates terminals considered free to move under thermal fluctuations and not involved into interactions. Setting up the short-range cut off parameter to 1.1nm, the Van der Waals interaction aren't computed behind this range, resulting an acceptable threshold above which no interactions occurs. Table 8 shed light on the different terminal strategies employment adopted by DM and DP dendrimers, evidencing that on average DM dendrimer use 33% of its terminals for primary interaction, contrariwise DP dendrimer involve only

22% of its terminals for primary interaction. In contrast, DM dendrimer has only 19% free fluctuating terminals, instead DP dendrimer has a significant 35% of its terminal not employed in interaction.

Table 8: Distance analysis of the dendrimer terminals from siRNA. Four main range were selected: “Primary interaction” indicates terminals involved in close interaction with siRNA; “secondary interaction” indicates terminals used to further stabilize complexation; “close to siRNA” indicates terminals that aren’t employed in any kind of interaction but can become active; “free terminals” which group the free terminals.

	PRIMARY INTERACTION ($d \leq 0.6\text{nm}$)	SECONDARY INTERACTION ($0.6\text{nm} < d \leq 1.2\text{nm}$)	CLOSE TO SIRNA ($1.2\text{nm} < d \leq 2.0\text{nm}$)	FREE TERMINALS ($d > 2.0\text{nm}$)
DM	33%	20%	28%	19%
DP	22%	15%	28%	35%

All before exhibited evidences seems to indicate that DM dendrimer may involve more terminals for binding and stabilizing purposes, compared to DP dendrimer. Furthermore, DM dendrimer seems to interact more closely with the groove of siRNA due to the higher affinity of N_0 terminal beads, which lead in wrapping the double strained filament around dendrimer. The results shown so far are in synergy with the data present in the literature^{27,131}. As mentioned in the introduction, ITC stoichiometry value for DP dendrimer declares that it can complex with almost 2 siRNAs molecules. This behavior has been largely explained among this chapter, but still remain a last question which is partial unexplained yet. We having noticed that DM dendrimer in 66% of replicates may binds only 1 siRNA, but how can in few circumstances complex even with 2 siRNA. To investigate this issue, distance analysis between COM of whole molecules (dendrimer and siRNAs) was evaluated. Figure 37 carry out the average distance between the COM of dendrimers and each siRNAs for all 12 replicas. Significant differences were observed considering 3 main distance range (Figure 37 bottom picture), divided as follows: A) 1.5-3nm range in which is observable interaction of dendrimer approximately on the lateral side of siRNA; B) 3-4nm range in which is observable complexation of dendrimer with the ends of siRNA around the 2 un-paired nucleotides; C) 3-10nm range in which no interaction occurs. In particular, is clearly detectable that DM dendrimer when hook one siRNA at one of the ends, the other one siRNA may easily be complexed (Figure 37 replicas 9-10-11-12). Contrariwise, when DM dendrimer bind on the lateral side of siRNA, second siRNA aggregation is hindered. Interaction with siRNA’s ends, probably is caused by the easiness to bind 2 un-paired nucleotides by the dendrimer terminals, but this primary interaction decreases the employment of the

other terminals. Consequently, higher number of terminals are free to fluctuate in the space, increasing the possibility to interact with another siRNA.

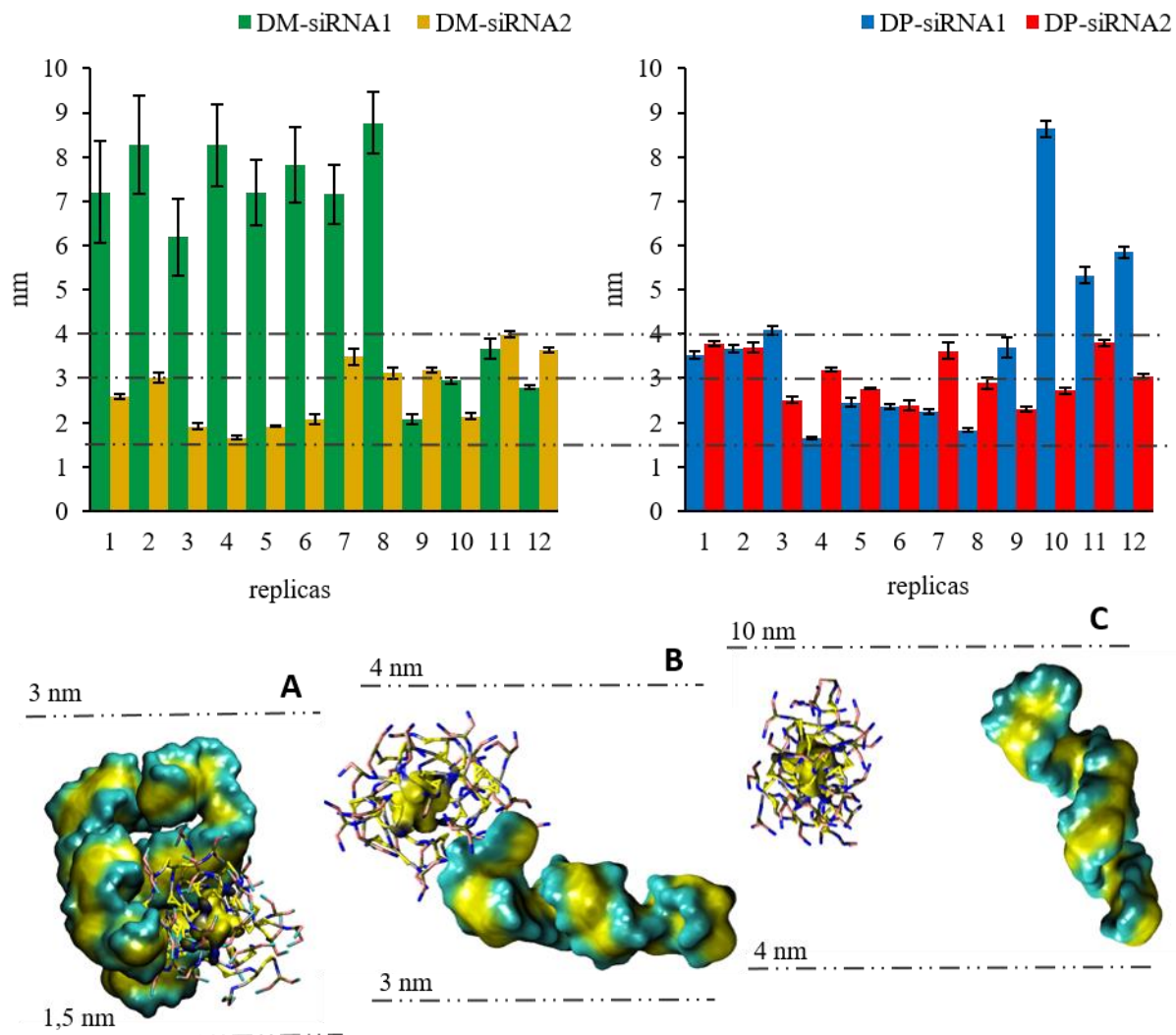


Figure 37: Distance bar diagram between center of mass (COM) of dendrimer and siRNAs represented by average and standard deviation. In the figure 3 main distance range is selected: **A)** 1.5-3nm range in which is observable interaction of dendrimer approximately on the lateral side of siRNA; **B)** 3-4nm range in which is observable complexation of dendrimer with the ends of siRNA around the 2 un-paired nucleotides; **C)** 3-10nm range in which no interaction between dendrimer and siRNA occurs.

To further improve the understanding of before mentioned phenomenon, two distance average graphs between COM of dendrimer and siRNAs over the time, where results double siRNAs complexation, is shown in Figure 1Figure 38 (central picture). Noteworthy, Figure 38 evidence shows that double siRNAs cluster aggregation occur after firstly has taken place dendrimer-siRNA ends binding.

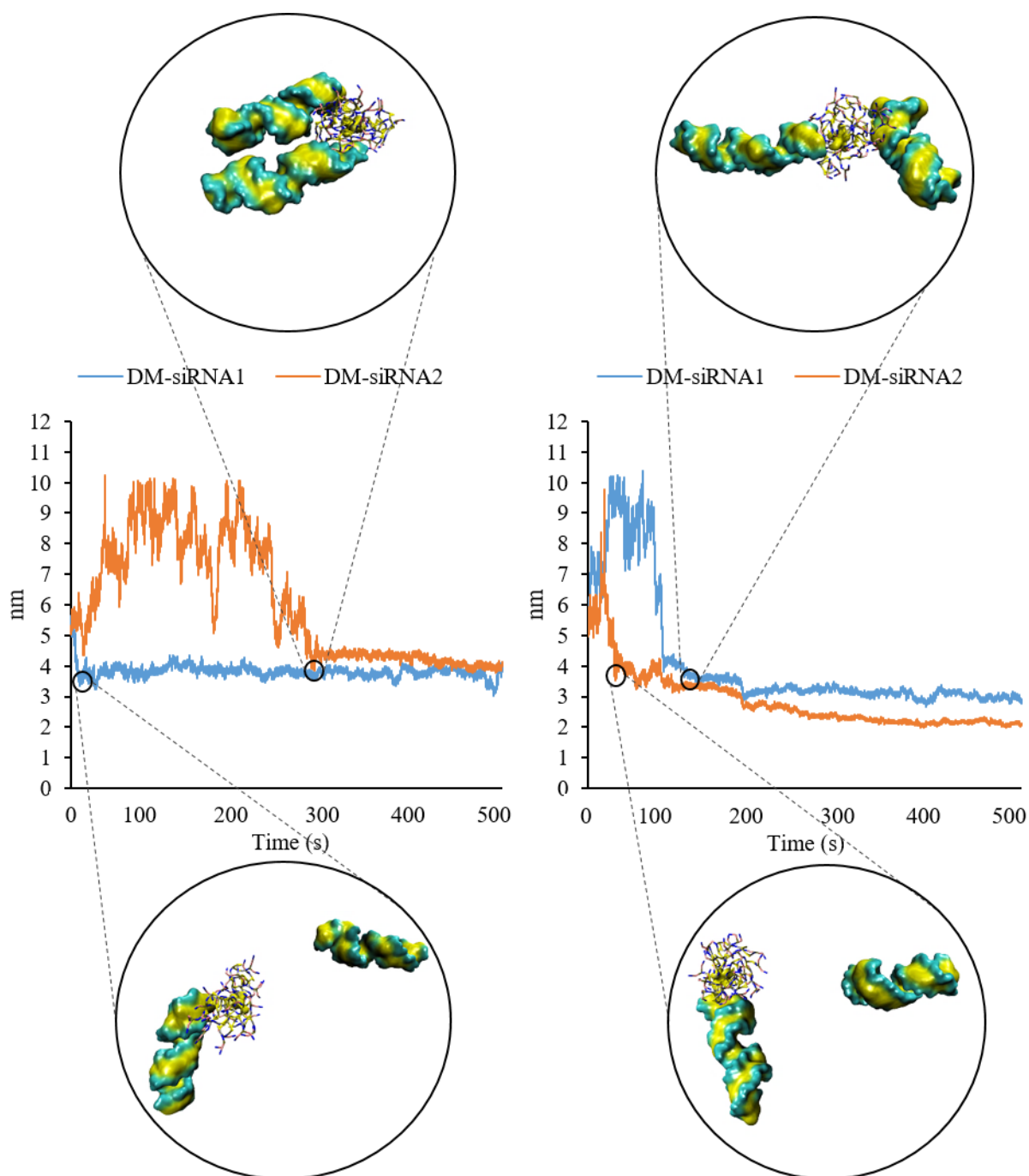


Figure 38: Dendrimer-siRNAs distance average over the time of replicas where results double siRNAs complexation, is shown in the central section of the picture. Instead on the top and bottom part of the figure snapshots of examined systems are extracted from the trajectory. Remarkably, the evidence shows than to achieve double siRNAs dendrimer complexation, is necessary that the dendrimer initially binds one of the first siRNA's ends.

As proof of these interaction mechanism, snapshots of dendrimer-siRNAs coupling are highlighted in the top and bottom part of Figure 38. Analyzing Figure 38 the first distinguishable consequence is that the ability to stretch the siRNA structure by the DM dendrimer is almost lost. Probably, the attitude showed by the DM dendrimer to wrap siRNA molecule is the key factor that implicitly

doesn't allow binding with another siRNA. Indeed, Figure 37 (replicas 1 to 8) notably carry out that in most of the cases when dendrimer-siRNA complexation occur on the lateral side, no more siRNA can be attached by dendrimer, suggesting a successful stretching of the siRNA structure. In general, taking together all previously computational results, stoichiometric values may be explained in the following way: DP dendrimer has clearly proved their enhanced affinity in binding 2 siRNA in comparison with DM dendrimer, demonstrating experimental results of 2.25 ± 0.03 . Further computational simulation of 1 dendrimer with 3 siRNAs might be useful to definitively evidence such stoichiometric value. Contrariwise, DM dendrimer has experimental stoichiometric value of 0.60 ± 0.03 , which was partially explained in this research work. An interesting hypothesis on the pathway to reach the real DM dendrimer data may be as following: DM behavior to complex with only 1 siRNA was observed in the 66% of replicas, instead in 33% of simulation, aggregation happen with 2 siRNAs. The main difference between these two cases is the conformation structure of bonded siRNAs. When dendrimer aggregate with only 1 siRNA, mostly of times it results in wrapping siRNA's filament around dendrimer, which strongly decrease the capability of another dendrimer to bind the same siRNA. On the other hand, when DM dendrimer complex 2 siRNAs, it no more can significantly stretch siRNA's structure, leaving them in more natural shape. The keystone lies precisely in this subtle fact, which implies a siRNA's greater surface area exposed in the solvent, resulting in more easiness for other dendrimers to bind the same siRNA. This competition mechanism may explain the reason of the 0.60 ± 0.03 stoichiometric value observed in vitro experiments.

5.2. Conclusions

The study here proposed investigated how small surface modification might lead in significant changing on the dendrimer-siRNA complexation dynamics and mechanism. More in detail, stoichiometric value of DM and DP dendrimer was explored using MD simulations to understand the different aggregation pathway. Outcome of this research work indicate DP to be significantly more efficient in binding 2 siRNAs molecules. Instead, DM dendrimer seems to complex siRNA more closely and probably suffer a competition mechanism, two key factors that explain the lower stoichiometric value. Furthermore, ITC binding curves (Figure S 2) indicates a drop for the DP-siRNA curve beyond 1.0 of DP/siRNA molar ratio, which let us suppose a competition mechanism between DP-DP and DP-siRNA. Competition mechanism evaluation would be interesting future development to achieve a more deep knowledge of the driving forces which results in experimental observed

dendrimer-siRNA binding behavior. In conclusion, this master thesis work provides a further evidence on the suitability of computational Coarse Grained molecular modeling, in generating reliable platform for investigating supramolecular characteristic of dendrimers delivery systems.

6. Conclusions and future developments

Achieving the comprehension of the supramolecular mechanism showed by Pyrrolidinium dendrimers (DP) and Morpholinium dendrimers (DM) in binding siRNA cargos, was the goal of this master thesis work. To explore such phenomenon, Molecular Dynamics (MD) simulation tools was adopted with the aim to investigate at the atomistic level the molecular process which lead in the different binding attitude showed by DM and DP dendrimers. Since atomistic MD has limitation on the computational effort needed to simulate huge systems for long scale period, a particular MD methodology called Coarse Grained (CG) was employed to permit large system and time scale simulations. CG technique has been proven in recent literature as well approximation of atomistic scale systems for studying the underlying mechanisms of aggregation or receptor-ligand phenomenon. DM and DP dendrimer CG models, as well as siRNA CG model were developed and validated with standard used methods. Therefore, dendrimer self-assembly behavior has been evaluated as further proof of CG models correctness. Results indicate that DP dendrimer has increased self-aggregation capability in comparison with DM dendrimer, which shows poor attitude to self-assembly. Subsequently, we tried to shed lights on the stoichiometry experimental values, which reveal that DP dendrimer can bind with approximately 2 siRNAs, while DM dendrimer complex with less than one. Interestingly, in our performed MD simulations we have observed the DM dendrimer can mainly couple with 1 siRNA, contrariwise, DP dendrimer might complex often with 2 siRNAs. Even if our MD results was in agreement with experimental data, we weren't able to observe the real exact experimental stoichiometric value for CG, methodology issues. However, we developed a basilar platform which goodly reflects the *in vitro* evidence and which may further be ameliorated. Future development of this platform may be for example the switching from non-polarizable water, to polarizable water, with the goal of emulating even better the realistic water-solvent. Another possible improvement might be an additional tuning up of topological terms, with greater attention to the dihedral angles, to better mimic the realistic dendrimer. Besides just mentioned improvable features, our platform seems on the right way for a future implementation of a routine that can predict the binding behavior between cationic phosphorous dendrimer and various ligand.

Acknowledgment

Seems like a month ago since I met him for the first time, the one who would become my actual supervisor...but here I am, writing the last lines of this work. It was like a dream, beautiful, powerful, exceptional ... an adventure started in Switzerland at "Dalle Molle institute for Artificial intelligence" ended here in front of Politecnico of Turin, giving my last "exam" ... and now?

Before anyone else, a major Thanks is for my thesis advisor Marco Agostino Deriu because makes possible such extraordinary and amazing experience. A Thanks for the constant support and brilliant teaching that was able to give me, during the time spent with him. But most of all... thank you for giving me the passion, the determination and the dream to become a Molecular Dynamics modeler.

I want also thanks my co-advisor Umberto Morbiducci for his great support and reviews during my thesis period.

A huge thank goes to Gianvito Grasso that was able to teach to me with so easiness and devotion, so complicated stuffs, and thanks in advance for future support.

I need to express my sincere Thanks to Alessia Chiaro, who endured me, between an egg white and gym handlebars, who always supported and helped me, but I actually thank you for never giving up.

I obviously send special thank you to my sisters, Diana and Gabriela, but for me "Bruta" and "Babu", which always supported and advised me...powerful girls that I am fortunate to have and that everyone should have.

Big thanks goes to Antonella Giacomuzzo, who hosted me for such long period and for been something like second mom in the time passed with her.

Last but not the least, I have no words to say Thank you mom and dad, Mirjana Stojceska and Tome Stojceski, for just everything you can imagine! No word is enough to describe how grateful I am to you.

...and now when everything is finished ... is only now that everything begins

-Filip Stojceski-

Bibliography

1. Strodthoff, C. Pathophysiology of rheumatoid arthritis. *Nurse Pract.* **7**, 32–35 (1982).
2. Smolen, J. S., Aletaha, D. & McInnes, I. B. Rheumatoid arthritis. *Lancet* **388**, 2023–2038 (2016).
3. Vos, T. *et al.* Global, regional, and national incidence, prevalence, and years lived with disability for 310 diseases and injuries, 1990–2015: a systematic analysis for the Global Burden of Disease Study 2015. *Lancet* **388**, 1545–1602 (2016).
4. Krokstad, S. *et al.* Global, regional, and national age–sex specific all-cause and cause-specific mortality for 240 causes of death, 1990–2013: a systematic analysis for the Global Burden of Disease Study 2013. *Lancet* **385**, 117–171 (2015).
5. Singh, J. A. *et al.* 2015 American College of Rheumatology Guideline for the Treatment of Rheumatoid Arthritis. *Arthritis Care Res. (Hoboken)*. **68**, 1–25 (2016).
6. Tarp, S. *et al.* Effect of nonsteroidal antiinflammatory drugs on the C-reactive protein level in rheumatoid arthritis: A meta-analysis of randomized controlled trials. *Arthritis Rheum.* **64**, 3511–3521 (2012).
7. Deal, C. L. *et al.* Treatment of arthritis with topical capsaicin: a double-blind trial. *Clin. Ther.* **13**, 383–95 (1991).
8. Matucci-Cerinic, M., Marabini, S., Jantsch, S., Cagnoni, M. & Partsch, G. Effects of capsaicin on the metabolism of rheumatoid arthritis synoviocytes in vitro. *Ann. Rheum. Dis.* **49**, 598–602 (1990).
9. Richards, B. L., Whittle, S. L. & Buchbinder, R. Neuromodulators for pain management in rheumatoid arthritis. *Cochrane Database Syst. Rev.* **26**, 172 (2012).
10. Burmester, G. R. & Pope, J. E. Novel treatment strategies in rheumatoid arthritis. *The Lancet* **389**, 2338–2348 (2017).
11. Benjamin, O. & Lappin, S. L. *Disease Modifying Anti-Rheumatic Drugs (DMARD)*. *StatPearls* (StatPearls Publishing, 2018).
12. Tanaka, E. & Yamanaka, H. [DMARDs (disease-modifying antirheumatic drugs)]. *Nihon Rinsho.* **71**, 1199–206 (2013).

13. Strojil, J. & Ciferská, H. Certolizumab pegol. *Klinická Farmakologie a Farmacie* **24**, 155–160 (2010).
14. Kaushik, V. & Moots, R. CDP-870 (certolizumab) in rheumatoid arthritis. *Expert Opin. Biol. Ther.* **5**, 601–606 (2005).
15. Moreland, L. W. *et al.* Etanercept therapy in rheumatoid arthritis: A randomized, controlled trial. *Ann. Intern. Med.* **130**, 478–486 (1999).
16. Scott, D. L. & Kingsley, G. H. Tumor Necrosis Factor Inhibitors for Rheumatoid Arthritis. *N. Engl. J. Med.* **355**, 704–712 (2006).
17. Feldmann, M. & Maini, R. N. TNF defined as a therapeutic target for rheumatoid arthritis and other autoimmune diseases. *Nat. Med.* **9**, 1245–1250 (2003).
18. Schiffelers, R. M., Xu, J., Storm, G., Woodle, M. C. & Scaria, P. V. Effects of treatment with small interfering RNA on joint inflammation in mice with collagen-induced arthritis. *Arthritis Rheum.* **52**, 1314–1318 (2005).
19. Kim, M. J. *et al.* Notch1 targeting siRNA delivery nanoparticles for rheumatoid arthritis therapy. *J. Control. Release* **216**, 140–148 (2015).
20. Andreana, I. *et al.* Anti-Inflammatory Effect of Anti-TNF- α SiRNA Cationic Phosphorus Dendrimer Nanocomplexes Administered Intranasally in a Murine Acute Lung Injury Model. *Biomacromolecules* **18**, 2379–2388 (2017).
21. Meunier, B., Zanta, M.-A., Loup, C., Majoral, J.-P. & Caminade, A.-M. Preparation of Water-Soluble Cationic Phosphorus-Containing Dendrimers as DNA Transfecting Agents. *Chem. - A Eur. J.* **5**, 3644–3650 (2005).
22. Caminade, A. M. & Majoral, J. P. Water-soluble phosphorus-containing dendrimers. *Progress in Polymer Science (Oxford)* **30**, 491–505 (2005).
23. Shcharbin, D. *et al.* Fourth generation phosphorus-containing dendrimers: Prospective drug and gene delivery carrier. *Pharmaceutics* **3**, 458–473 (2011).
24. Ferenc, M. *et al.* Phosphorus dendrimers as carriers of siRNA-characterisation of dendriplexes. *Molecules* **18**, 4451–4466 (2013).
25. Madrid, R. *et al.* Validation of a Generation 4 Phosphorus-Containing Polycationic Dendrimer for Gene Delivery Against HIV-1. *Curr. Med. Chem.* **19**, 5044–5051 (2012).

26. Caminade, A. M., Turrin, C. O. & Majoral, J. P. Biological properties of phosphorus dendrimers. *New Journal of Chemistry* **34**, 1512–1524 (2010).
27. Deriu, M. A. *et al.* Elucidating the role of surface chemistry on cationic phosphorus dendrimer-siRNA complexation. *Nanoscale* **10**, 10952–10962 (2018).
28. Padié, C. *et al.* Polycationic phosphorus dendrimers: Synthesis, characterization, study of cytotoxicity, complexation of DNA, and transfection experiments. *New J. Chem.* **33**, 318–326 (2009).
29. Cutolo, M., Kitas, G. D. & van Riel, P. L. C. M. Burden of disease in treated rheumatoid arthritis patients: Going beyond the joint. *Seminars in Arthritis and Rheumatism* **43**, 479–488 (2014).
30. Turesson, C., O’Fallon, W. M., Crowson, C. S., Gabriel, S. E. & Matteson, E. L. Extra-articular disease manifestations in rheumatoid arthritis: Incidence trends and risk factors over 46 years. *Ann. Rheum. Dis.* **62**, 722–727 (2003).
31. Majithia, V. & Geraci, S. A. Rheumatoid Arthritis: Diagnosis and Management. *American Journal of Medicine* **120**, 936–939 (2007).
32. Yamato, M., Tamai, K., Yamaguchi, T. & Ohno, W. Mri of the knee in rheumatoid arthritis: Gd-dtpa perfusion dynamics. *J. Comput. Assist. Tomogr.* **17**, 781–785 (1993).
33. Petersson, C. J. Painful shoulders in patients with rheumatoid arthritis: Prevalence, clinical and radiological features. *Scand. J. Rheumatol.* **15**, 275–279 (1986).
34. Feldon, P. & Terrono, A. L. Carpal tunnel syndrome in rheumatoid arthritis. *Techniques in Orthopaedics* **21**, 42–47 (2006).
35. Inoue, H. *et al.* Carpal tunnel syndrome grading system in rheumatoid arthritis. *J. Orthop. Sci.* **7**, 188–193 (2003).
36. Hoes, J. N., Bultink, I. E. & Lems, W. F. Management of osteoporosis in rheumatoid arthritis patients. *Expert Opin. Pharmacother.* **16**, 559–571 (2015).
37. Heidari, B. & Hassanjani Roushan, M. R. Rheumatoid arthritis and osteoporosis. *Casp. J. Intern. Med.* **3**, 445–6 (2012).
38. de Pablo, P., Chapple, I. L. C., Buckley, C. D. & Dietrich, T. Periodontitis in systemic rheumatic diseases. *Nat. Rev. Rheumatol.* **5**, 218–224 (2009).

39. Alenghat, F. J. The Prevalence of Atherosclerosis in Those with Inflammatory Connective Tissue Disease by Race, Age, and Traditional Risk Factors. *Sci. Rep.* **6**, 20303 (2016).
40. Aviña-Zubieta, J. A. *et al.* Risk of cardiovascular mortality in patients with rheumatoid arthritis: A meta-analysis of observational studies. *Arthritis Care Res.* **59**, 1690–1697 (2008).
41. Cathey, M. A. *et al.* The mortality of rheumatoid arthritis. *Arthritis Rheum.* **37**, 481–494 (2007).
42. Turesson, C. Extra-articular rheumatoid arthritis. *Curr. Opin. Rheumatol.* **25**, 360–366 (2013).
43. Deane, K. D. *et al.* Genetic and environmental risk factors for rheumatoid arthritis. *Best Practice and Research: Clinical Rheumatology* **31**, 3–18 (2017).
44. Yarwood, A., Huizinga, T. W. J. & Worthington, J. The genetics of rheumatoid arthritis: Risk and protection in different stages of the evolution of RA. *Rheumatol. (United Kingdom)* **55**, 199–209 (2015).
45. Kurkó, J. *et al.* Genetics of rheumatoid arthritis - A comprehensive review. *Clinical Reviews in Allergy and Immunology* **45**, 170–179 (2013).
46. Sugiyama, D. *et al.* Impact of smoking as a risk factor for developing rheumatoid arthritis: A meta-analysis of observational studies. *Ann. Rheum. Dis.* **69**, 70–81 (2010).
47. Yinshi Yue, Y. Y. Microbial Infection and Rheumatoid Arthritis. *J. Clin. Cell. Immunol.* **04**, (2014).
48. Calabresi, E., Petrelli, F., Bonifacio, A. F., Puxeddu, I. & Alunno, A. One year in review 2018: pathogenesis of rheumatoid arthritis. *Clin. Exp. Rheumatol.* **36**, 175–184
49. Gazitt, T., Lood, C. & Elkon, K. B. Citrullination in Rheumatoid Arthritis—A Process Promoted by Neutrophil Lysis? *Rambam Maimonides Med. J.* **7**, e0027 (2016).
50. Darrah, E. & Andrade, F. Rheumatoid arthritis and citrullination. *Current Opinion in Rheumatology* **30**, 72–78 (2018).
51. Fournier, C. Where do T cells stand in rheumatoid arthritis? *Jt. Bone Spine* **72**, 527–532 (2005).
52. McInnes, I. B. & Schett, G. Cytokines in the pathogenesis of rheumatoid arthritis. *Nature Reviews Immunology* **7**, 429–442 (2007).

53. Asquith, D. L., Bryce, S. A. & Nibbs, R. J. B. T cell migration in rheumatoid arthritis. *Current Opinion in Rheumatology* **27**, 204–211 (2015).
54. Feldmann, M., Brennan, F. M. & Maini, R. N. ROLE OF CYTOKINES IN RHEUMATOID ARTHRITIS. *Annu. Rev. Immunol.* **14**, 397–440 (1996).
55. Marston, B., Palanichamy, A. & Anolik, J. H. B cells in the pathogenesis and treatment of rheumatoid arthritis. *Current Opinion in Rheumatology* **22**, 307–315 (2010).
56. Kinne, R. W., Brauer, R., Stuhlmüller, B., Palomo-Kinne, E. & Burmester, G.-R. Review - Macrophages in rheumatoid arthritis. *Arthritis Res.* **2**, 189–202 (2000).
57. Chen, L. *et al.* Tissue factor expression in rheumatoid synovium: A potential role in pannus invasion of rheumatoid arthritis. *Acta Histochem.* **115**, 692–697 (2013).
58. De Jong, B. A. W. *et al.* The diagnostic properties of rheumatoid arthritis antibodies recognizing a cyclic citrullinated peptide. *Arthritis Rheum.* **43**, 155–163 (2002).
59. Sudoł-Szopińska, I., Jans, L. & Teh, J. Rheumatoid arthritis: what do MRI and ultrasound show. *J. Ultrason.* **17**, 5–16 (2017).
60. Bruyn, G. A. *et al.* Scoring ultrasound synovitis in rheumatoid arthritis: a EULAR-OMERACT ultrasound taskforce — Part 1: definition and development of a standardised, consensus-based scoring system. *RMD Open* **3**, e000428 (2017).
61. O’Dell, J. R. Therapeutic Strategies for Rheumatoid Arthritis. *N. Engl. J. Med.* **350**, 2591–2602 (2004).
62. Ali, T. *et al.* Clinical use of anti-TNF therapy and increased risk of infections. *Drug. Healthc. Patient Saf.* **79** (2013). doi:10.2147/DHPS.S28801
63. Fattal, E. & Bochot, A. State of the art and perspectives for the delivery of antisense oligonucleotides and siRNA by polymeric nanocarriers. *Int. J. Pharm.* **364**, 237–248 (2008).
64. Lou, D. & Saltzman, W. M. Synthetic DNA delivery systems. *Nat. Biotechnol.* **18**, 33–37 (2000).
65. Lee, C. C., MacKay, J. A., Fréchet, J. M. J. & Szoka, F. C. Designing dendrimers for biological applications. *Nat. Biotechnol.* **23**, 1517–1526 (2005).
66. Pavan, G. M. *et al.* PAMAM dendrimers for siRNA delivery: computational and experimental insights. *Chemistry* **16**, 7781–95 (2010).

67. Xu, Y. *et al.* Specific delivery of delta-5-desaturase siRNA via RNA nanoparticles supplemented with dihomo- γ -linolenic acid for colon cancer suppression. *Redox Biol.* **21**, 101085 (2019).
68. Hannon, G. J. RNA interference. *Nature* **418**, 244–251 (2002).
69. Bannerjee, S. *et al.* Drug delivery systems: An updated review. *Int. J. Pharm. Investig.* **2**, 2 (2012).
70. Tomalia, D. A. *et al.* A New Class of Polymers: Starburst-Dendritic Macromolecules. *Polym. J.* **17**, 117–132 (2006).
71. Solassol, J. *et al.* Cationic phosphorus-containing dendrimers reduce prion replication both in cell culture and in mice infected with scrapie. *J. Gen. Virol.* **85**, 1791–1799 (2004).
72. Alder, B. J. & Wainwright, T. E. Studies in molecular dynamics. I. General method. *J. Chem. Phys.* **31**, 459–466 (1959).
73. Car, R. & Parrinello, M. Unified approach for molecular dynamics and density-functional theory. *Phys. Rev. Lett.* **55**, 2471–2474 (1985).
74. Johnson, J. K., Zollweg, J. A. & Gubbins, K. E. The lennard-jones equation of state revisited. *Mol. Phys.* **78**, 591–618 (1993).
75. Lee, H. *et al.* A smooth particle mesh Ewald method. *J. Chem. Phys.* **103**, 8577–8593 (2002).
76. Gibbs, J. W. *Elementary principles in statistical mechanics: Developed with especial reference to the rational foundation of thermodynamics. Elementary Principles in Statistical Mechanics: Developed with Especial Reference to the Rational Foundation of Thermodynamics* (Cambridge University Press, 2010). doi:10.1017/CBO9780511686948
77. Van Gunsteren, W. F. & Berendsen, H. J. C. A Leap-Frog Algorithm for Stochastic Dynamics. *Mol. Simul.* **1**, 173–185 (1988).
78. Hess, B., Bekker, H., Berendsen, H. J. C. & Fraaije, J. G. E. M. LINCS: A Linear Constraint Solver for molecular simulations. *J. Comput. Chem.* **18**, 1463–1472 (1997).
79. Berendsen, H. J. C., Postma, J. P. M., Van Gunsteren, W. F., Dinola, A. & Haak, J. R. Molecular dynamics with coupling to an external bath. *J. Chem. Phys.* **81**, 3684–3690 (1984).
80. Bussi, G., Donadio, D. & Parrinello, M. Canonical sampling through velocity rescaling. *J.*

- Chem. Phys.* **126**, 014101 (2007).
81. Nosé, S. & Klein, M. L. Constant pressure molecular dynamics for molecular systems. *Mol. Phys.* **50**, 1055–1076 (1983).
 82. Andersen, H. C. Molecular dynamics simulations at constant pressure and/or temperature. *J. Chem. Phys.* **72**, 2384–2393 (1980).
 83. Parrinello, M. & Rahman, A. Polymorphic transitions in single crystals: A new molecular dynamics method. *J. Appl. Phys.* **52**, 7182–7190 (1981).
 84. Bernardi, R. C., Melo, M. C. R. & Schulten, K. Enhanced sampling techniques in molecular dynamics simulations of biological systems. *Biochimica et Biophysica Acta - General Subjects* **1850**, 872–877 (2015).
 85. Yi, J. Y., Bernholc, J. & Salamon, P. Simulated annealing strategies for molecular dynamics. *Comput. Phys. Commun.* **66**, 177–180 (1991).
 86. Riniker, S., Allison, J. R. & Van Gunsteren, W. F. On developing coarse-grained models for biomolecular simulation: A review. *Physical Chemistry Chemical Physics* **14**, 12423–12430 (2012).
 87. Ercolesi, F. & Adams, J. B. Interatomic potentials from first-principles calculations: The force-matching method. *EPL* **26**, 583–588 (1994).
 88. Marrink, S. J., Risselada, H. J., Yefimov, S., Tieleman, D. P. & Vries, A. H. De. The MARTINI Force Field : Coarse Grained Model for Biomolecular Simulations The MARTINI Force Field : Coarse Grained Model for Biomolecular Simulations. *J. Phys. Chem. B* **111**, 7812–7824 (2007).
 89. Moore, T. C., Iacovella, C. R. & McCabe, C. Derivation of coarse-grained potentials via multistate iterative Boltzmann inversion The multiscale coarse-graining method. I. A rigorous bridge between atomistic and coarse-grained models On the representability problem and the physical meaning of coarse. *Cit. J. Chem. Phys.* **140**, 44108 (2014).
 90. Reith, D., Pütz, M. & Müller-Plathe, F. Deriving effective mesoscale potentials from atomistic simulations. *J. Comput. Chem.* **24**, 1624–1636 (2003).
 91. Lyubartsev, A. P., Karttunen, M., Vattulainen, I. & Laaksonen, A. On coarse-graining by the Inverse Monte Carlo method: Dissipative Particle Dynamics simulations made to a precise tool in soft matter modeling. *Soft Mater.* **1**, 121–137 (2003).

92. Monticelli, L. *et al.* The MARTINI coarse-grained force field: Extension to proteins. *J. Chem. Theory Comput.* **4**, 819–834 (2008).
93. López, C. A. *et al.* Martini coarse-grained force field: Extension to carbohydrates. *J. Chem. Theory Comput.* **5**, 3195–3210 (2009).
94. Ala-Nissila, T., Vattulainen, I., Monticelli, L., Puisto, S. R. & Rossi, G. Coarse-graining polymers with the MARTINI force-field: polystyrene as a benchmark case. *Soft Matter* **7**, 698–708 (2010).
95. Uusitalo, J. J., Ingólfsson, H. I., Akhshi, P., Tieleman, D. P. & Marrink, S. J. Martini Coarse-Grained Force Field: Extension to DNA. *J. Chem. Theory Comput.* **11**, 3932–3945 (2015).
96. Yesylevskyy, S. O., Schäfer, L. V., Sengupta, D. & Marrink, S. J. Polarizable water model for the coarse-grained MARTINI force field. *PLoS Comput. Biol.* **6**, 1–17 (2010).
97. De Jong, D. H., Baoukina, S., Ingólfsson, H. I. & Marrink, S. J. Martini straight: Boosting performance using a shorter cutoff and GPUs. *Comput. Phys. Commun.* **199**, 1–7 (2016).
98. Milano, G., Goudeau, S. & Müller-Plathe, F. Multicentered Gaussian-based potentials for coarse-grained polymer simulations: Linking atomistic and mesoscopic scales. *J. Polym. Sci. Part B Polym. Phys.* **43**, 871–885 (2005).
99. Kremer, K., Bürger, T., Batoulis, J., Hahn, O. & Tschöp, W. Simulation of polymer melts. I. Coarse-graining procedure for polycarbonates. *Acta Polym.* **49**, 61–74 (2002).
100. Marrink, S. J. & Tieleman, D. P. Perspective on the Martini model. *Chem. Soc. Rev.* **42**, 6801 (2013).
101. Zhong, T., Ai, P. & Zhou, J. Structures and properties of PAMAM dendrimer: A multi-scale simulation study. *Fluid Phase Equilib.* **302**, 43–47 (2011).
102. Rahimi, A., Amjad-Iranagh, S. & Modarress, H. Molecular dynamics simulation of coarse-grained poly(L-lysine) dendrimers. *J. Mol. Model.* **22**, 1–10 (2016).
103. Elizondo-García, M., Márquez-Miranda, V., Araya-Durán, I., Valencia-Gallegos, J. & González-Nilo, F. Self-Assembly Behavior of Amphiphilic Janus Dendrimers in Water: A Combined Experimental and Coarse-Grained Molecular Dynamics Simulation Approach. *Molecules* **23**, 969 (2018).
104. Lee, H. & Larson, R. G. Molecular dynamics simulations of PAMAM dendrimer-induced

- pore formation in DPPC bilayers with a coarse-grained model. *J. Phys. Chem. B* **110**, 18204–18211 (2006).
105. Wang, Y. L., Lu, Z. Y. & Laaksonen, A. Specific binding structures of dendrimers on lipid bilayer membranes. *Phys. Chem. Chem. Phys.* **14**, 8348–8359 (2012).
 106. Curtis, D. E. *et al.* Avogadro: an advanced semantic chemical editor, visualization, and analysis platform. *J. Cheminform.* **4**, 17 (2012).
 107. Wang, J., Wolf, R. M., Caldwell, J. W., Kollman, P. A. & Case, D. A. Development and testing of a general amber force field. *J. Comput. Chem.* **25**, 1157–1174 (2004).
 108. Hess, B., Kutzner, C., Van Der Spoel, D. & Lindahl, E. GROMACS 4: Algorithms for highly efficient, load-balanced, and scalable molecular simulation. *J. Chem. Theory Comput.* **4**, 435–447 (2008).
 109. Abraham, M. J. *et al.* Gromacs: High performance molecular simulations through multi-level parallelism from laptops to supercomputers. *SoftwareX* **1–2**, 19–25 (2015).
 110. Hao, G. F., Xu, W. F., Yang, S. G. & Yang, G. F. Multiple simulated annealing-molecular dynamics (MSA-MD) for conformational space search of peptide and miniprotein. *Sci. Rep.* **5**, 15568 (2015).
 111. Graham, J. A., Essex, J. W. & Khalid, S. PyCGTOOL: Automated Generation of Coarse-Grained Molecular Dynamics Models from Atomistic Trajectories. *J. Chem. Inf. Model.* **57**, 650–656 (2017).
 112. Marrink, S. J., de Vries, A. H. & Mark, A. E. Coarse Grained Model for Semiquantitative Lipid Simulations. *J. Phys. Chem. B* **108**, 750–760 (2004).
 113. Mantha, S. & Yethiraj, A. Conformational Properties of Sodium Polystyrenesulfonate in Water: Insights from a Coarse-Grained Model with Explicit Solvent. *J. Phys. Chem. B* **119**, 11010–11018 (2015).
 114. Shelley, J. C. *et al.* Simulations of phospholipids using a coarse grain model. *J. Phys. Chem. B* **105**, 9785–9792 (2001).
 115. Tironi, I. G., Sperb, R., Smith, P. E. & Van Gunsteren, W. F. A generalized reaction field method for molecular dynamics simulations. *J. Chem. Phys.* **102**, 5451–5459 (1995).
 116. Humphrey, W., Dalke, A. & Schulten, K. VMD: Visual molecular dynamics. *J. Mol. Graph.*

- 14**, 33–38 (1996).
117. Uusitalo, J. J., Ingólfsson, H. I., Marrink, S. J. & Faustino, I. Martini Coarse-Grained Force Field: Extension to RNA. *Biophys. J.* **113**, 246–256 (2017).
118. Ramírez, C. L. *et al.* Coarse-grained simulations of heme proteins: Validation and study of large conformational transitions. *J. Chem. Theory Comput.* **12**, 3390–3397 (2016).
119. Monticelli, L. *et al.* Improved Angle Potentials for Coarse-Grained Molecular Dynamics Simulations. *J. Chem. Theory Comput.* **9**, 3282–3292 (2013).
120. Pavan, G. M. & Danani, A. The influence of dendron’s architecture on the ‘rigid’ and ‘flexible’ behaviour in binding DNA--a modelling study. *Phys. Chem. Chem. Phys.* **12**, 13914–13917 (2010).
121. Mulcock, C. *et al.* Cationic PAMAM Dendrimers Aggressively Initiate Blood Clot Formation. *ACS Nano* **6**, 9900–9910 (2012).
122. Duncan, R. & Izzo, L. Dendrimer biocompatibility and toxicity. *Advanced Drug Delivery Reviews* **57**, 2215–2237 (2005).
123. Duff, Jr., M. R., Grubbs, J. & Howell, E. E. Isothermal Titration Calorimetry for Measuring Macromolecule-Ligand Affinity. *J. Vis. Exp.* (2011). doi:10.3791/2796
124. Bouchemal, K. & Mazzaferro, S. How to conduct and interpret ITC experiments accurately for cyclodextrin-guest interactions. *Drug Discovery Today* **17**, 623–629 (2012).
125. Wang, C. & Tam, K. C. Interactions between poly(acrylic acid) and sodium dodecyl sulfate: Isothermal titration calorimetric and surfactant ion-selective electrode studies. *J. Phys. Chem. B* **109**, 5156–5161 (2005).
126. Sun, X. *et al.* Hierarchical self-assembly of zwitterionic dendrimer–anionic surfactant complexes into multiple stimuli-responsive dynamic nanotubes. *Nanoscale* **10**, 1411–1419 (2017).
127. Jensen, L. B. *et al.* Elucidating the molecular mechanism of PAMAM-siRNA dendriplex self-assembly: effect of dendrimer charge density. *Int. J. Pharm.* **416**, 410–8 (2011).
128. Feng, X. *et al.* Host-guest chemistry of dendrimer-drug complexes. 5. Insights into the design of formulations for noninvasive delivery of heparin revealed by isothermal titration calorimetry and NMR studies. *J. Phys. Chem. B* **114**, 11017–11026 (2010).

129. Zhang, P. *et al.* Self-Aggregation of Amphiphilic Dendrimer in Aqueous Solution: The Effect of Headgroup and Hydrocarbon Chain Length. *Langmuir* **31**, 7919–7925 (2015).
130. Chen, C. *et al.* Mastering Dendrimer Self-Assembly for Efficient siRNA Delivery: From Conceptual Design to In Vivo Efficient Gene Silencing. *Small* **12**, 3667–3676 (2016).
131. Vasumathi, V. & Maiti, P. K. Complexation of siRNA with dendrimer: A molecular modeling approach. *Macromolecules* **43**, 8264–8274 (2010).

Supporting Information

Table S 1: Table extracted from Deriu et al. paper²⁷. ITC technique main results of DM-siRNA and DP-siRNA experimental analysis which evidence stoichiometry (N), dissociation constant (k_d) and binding enthalpy (ΔH), entropy (ΔS) and free energy (ΔG).

Property	Unit	DP	DM	DP/DM
$N_{siRNA/dendrimer}$	#	2.25 ± 0.03	0.60 ± 0.03	3.75 ± 0.53
k_d	μM	5.60 ± 0.85	21.49 ± 2.11	4.02 ± 1.06
ΔH	$kcal/mol$	-47.00 ± 2.83	-53.25 ± 0.21	0.88 ± 0.06
$T\Delta S$	$kcal/mol$	-39.65 ± 2.95	-46.96 ± 0.21	0.84 ± 0.07
ΔG	$kcal/mol$	-7.35 ± 0.12	-6.29 ± 0.00	1.17 ± 0.02

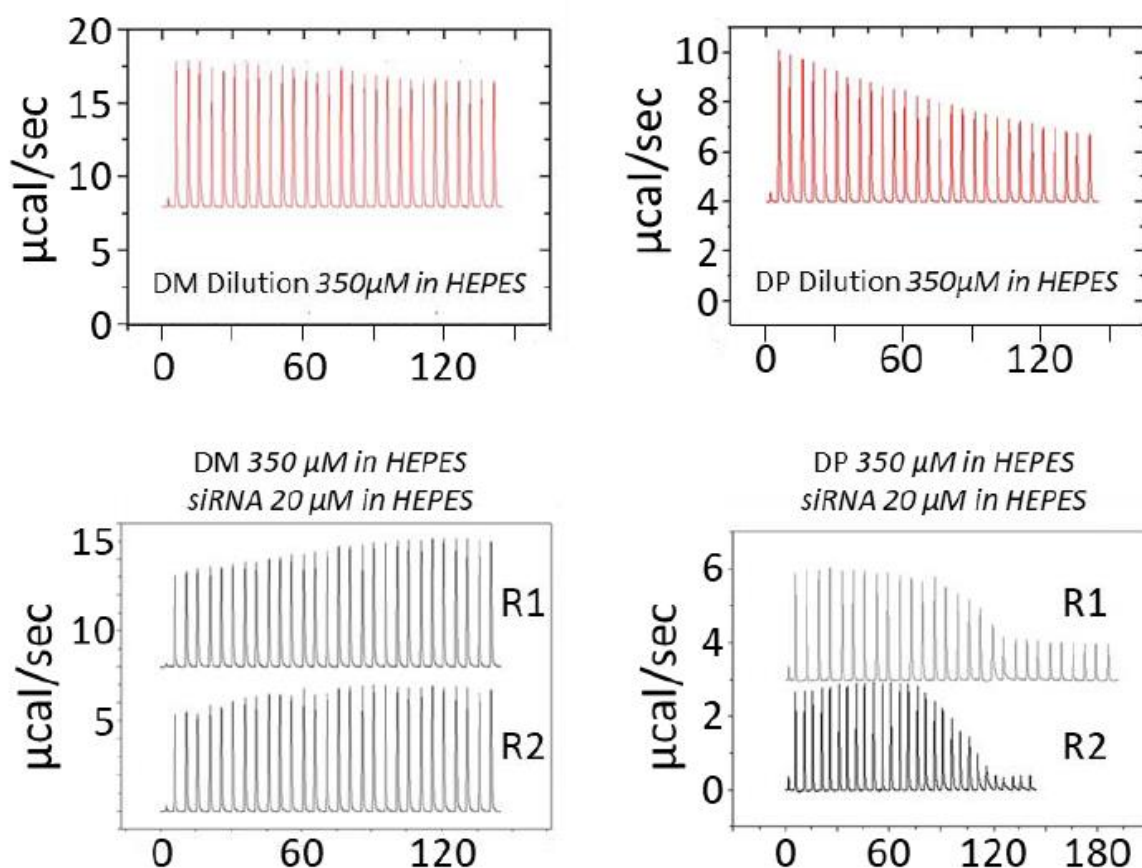


Figure S 1: Figure extracted from Deriu et al. paper²⁷. ITC injection curves for DM (left pictures) and DP (right pictures) molecules. Injections of DM dendrimer solution are add up to the HEPES buffer (top panel, red curve) and siRNA solution in HEPES (bottom panel, black curves with 2 experimental repetitions R1 and R2) in the ITC machine. The area underlying each injection peak is equal to the total heat released for that attempt. When such total injection heat is plotted against the molar ratio of dendrimer solution added to siRNA for ITC

titration, we get a complete binding isotherm for each interaction. Dilution experiments (top panels, red curves) show different trend for DM and DP dendrimers. R1 and R2 are two repetitions of the binding experiment (bottom panels, black curves) where even in this case is appreciable different trends.

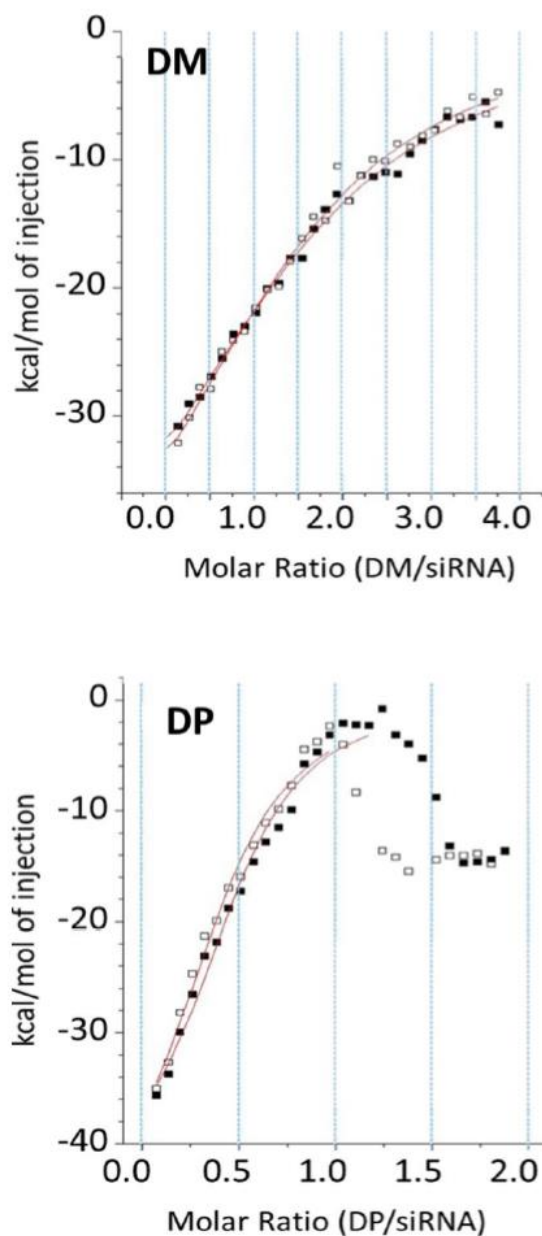


Figure S 2: Picture extracted from Deriu et al. paper²⁷. Two separate in vitro experiment repetitions (black and white squares) are reported for both DP-siRNA (bottom) and DM-siRNA (top) studied systems. The solid continuous red curves are calculated adopting the best-fit terms. The data was fitted employing one the site model. The figure is obtained by subtracting before fitting the dilution signal from ITC titration signals.